INFORMATION TO USERS

The most advanced technology has been used to photograph and reproduce this manuscript from the microfilm master. UMI films the text directly from the original or copy submitted. Thus, some thesis and dissertation copies are in typewriter face, while others may be from any type of computer printer.

The quality of this reproduction is dependent upon the quality of the copy submitted. Broken or indistinct print, colored or poor quality illustrations and photographs, print bleedthrough, substandard margins, and improper alignment can adversely affect reproduction.

In the unlikely event that the author did not send UMI a complete manuscript and there are missing pages, these will be noted. Also, if unauthorized copyright material had to be removed, a note will indicate the deletion.

Oversize materials (e.g., maps, drawings, charts) are reproduced by sectioning the original, beginning at the upper left-hand corner and continuing from left to right in equal sections with small overlaps. Each original is also photographed in one exposure and is included in reduced form at the back of the book.

Photographs included in the original manuscript have been reproduced xerographically in this copy. Higher quality 6" x 9" black and white photographic prints are available for any photographs or illustrations appearing in this copy for an additional charge. Contact UMI directly to order.

U·M·I

University Microfilms International
A Bell & Howell Information Company
300 North Zeeb Road, Ann Arbor, MI 48106-1346 USA
313 761 4700 800 521 0600

Order Number 9119644

Electron spin resonance spectroscopy of group IB metal clusters and groups IA–IIA mixed-metal clusters generated in inert gas matrices at 4.2 K

Kernizan, Carl Frederick, Ph.D.

City University of New York, 1991

U·M·I

300 N. Zeeb Rd.
Ann Arbor, MI 48106

ELECTRON SPIN RESONANCE SPECTROSCOPY OF GROUP IB METAL CLUSTERS AND GROUPS IA-IIA MIXED-METAL CLUSTERS GENERATED IN INERT GAS MATRICES AT 4.2 K.

by

CARL F. KERNIZAN

A dissertation submitted to the Graduate Faculty in Chemistry in partial fulfillment of the requirements for the degree of Doctor of Philosophy, The City University of New York.

1991

This manuscript has been read and accepted for the Graduate Faculty in Chemistry in satisfaction of the dissertation requirement for the degree of Doctor of Philosophy.

5/10/89
Date

Chair of Examining Committee

5/11/89
Date

Executive Officer

Supervisory Committee

The City University of New York

THIS ONE IS FOR THE ANCESTORS. THANK YOU.

TABLE OF CONTENTS

TABLE OF CONTENTS (continued)

TABLE OF CONTENTS (continued)

LIST OF TABLES

LIST OF TABLES (continued)

LIST OF FIGURES

LIST OF FIGURES (continued)

I. INTRODUCTION

The interest in the generation of small metal clusters has seen a tremendous growth in the past decade. With this increasing interest in the field, new generation techniques and various spectroscopic approaches have been used in an attempt to elucidate the sizes, shapes, and the chemistry of these species (1,10). Small metal clusters are broadly defined as aggregates of 3 to 20 atoms or the limiting number of atoms approaching the bulk phase of the peticular metal. The sizes of these clusters provide an approximate means for their classification. These clusters have been grown in noble gas, in zeolites and in organic support matrices at 4 to 77K, (11-15). The clusters that we will describe were all generated in nitrogen or inert matrices near 4K and in the absence of any ligands. They are electrically neutral and believed to be in their ground states.

This work can be described as " the fourth generation " cluster production from our laboratory. Successful work performed on the ESR of the group IA metal clusters have already been published, (17), and have added to the growing literature of small metal clusters. Interestingly enough the work done on the alkali metals proved to be in very good agreement with a series of theoretical publications such as photoionization measurements, (18), and dissociation energies, (19). Also, a series of sophisticated computational papers which were published around that time, (20-23), did predict reasonable potential surfaces for these alkali clusters. Since then, the field has grown dramatically and explicit compilations or reviews articles have appeared in the journals, (24-27), describing selective clustering techniques and various spectroscopic approaches that are currently being used to study these metal clusters. The interest in the

economic importance of these species has also grown as evidence by a series of articles in C & E News, (28-32), and Nature magazine, (33). Recently the diversity of the field is becoming apparent with the technique now being applied for the generation of heteronuclear clusters, (34,37). These mixed-metal species if generated successfully can offer great insight in the basic molecular bonding scheme of different sized atoms. From a more practical stand point, these mixed-metal species can be conceived as alloys and of course are of great interest to industry.

In this work UV-Visible Optical Absorption spectroscopy was used along with ESR in the study of the clusters generated. The OA technique was specially useful for confirming the presence of species such as, dimers and tetramers, not detectable by ESR (1,38-43).

The greatest advantage of low temperature ESR is that the spectrum is assumed to be generated from species in their ground state and unlike the molecular beam technique, no metastable or vibrationally excited states are expected in the spectrum. One of the many problems still present in cluster generation are the so called "matrix effects ", which can be very decisive in the generation or non generation of these metal clusters. In practice, several support matrices are chosen and if any clusters are generated the invariance in their molecular parameters are taken as an indication of real physical properties rather than matrix effects.

The ESR of the group IB metals generated in a series of support matrices will be presented in this dissertation. Whenever possible the observed parameters will be compared with theoretical calculations, (44-46). UV-visible OA spectroscopy was also performed as a secondary probing technique and proved valuable in the assignment of species generated in

different matrices. The ESR of mixed-metal clusters of the groups IA-IIA will also be presented, although many questions regarding the size of these size clusters remained unanswered.

II. EXPERIMENTAL

II.1 Introduction

The matrices were prepared by codepositing hot metal vapor generated by a resistively heated source along with a large excess of nonreactive gas on a target mounted within the ESR cavity, (47-52). Both target and matrix were maintained near 4K by the liquid helium cryostat. On the surface of the target, the metal vapors were rapidly frozen and any species, single atom or clusters, formed were trapped in the matrix.The group IB metal clusters were grown using Nitrogen as the matrix gas. Although Argon, Xenon, and Krypton matrix gases were also used, only previously observed spectra, (48), or broad featureless unresolved spectra were generated. The group IA-IIA mixed-metal clusters were also grown in Argon, Nitrogen and Krypton matrices, but only when grown in an Argon matrix could spectra observed be assigned to the mixed-metal species. The matrices were annealed stepwise to a few degrees below the melting point of the matrix gas. In some cases the rise in temperature warmed up the matrix cage enough to allow diffusion or the generation of new species which were overlapped by stronger better resolved species present at 4K. But in most instances there was little diffusion through the matrix and annealing only narrowed broaden 4K transitions thus giving much better signal resolution.

A Xe-Hg high pressure lamp (CANRAD HANOVIA, # 901B-1) was used for both photolysis and optical absorption work. Photolysing the matrix also resulted in better signal resolution. However prolonged photolysis bleached rather than enhanced the signals. The samples formed were then

studied using a commercial spectrometer. A block diagram of the apparatus used in these experiments is shown in fig. (2.1).

II.2 Spectrometer and Magnet

In September 1983 the new spectrometer, (IBM BRUKER ER 200 ESR) ("Bruker"), arrived in the laboratory. It was interfaced with an existing electromagnet and power supply (JEOLCO JAPANESE OPTICS LABORATORY ME-3) by IBM' s staff. Since extensive documentation was provided by both manufacturers, only a brief discussion will be presented here, (49,50). The spectrometer was extremely reliable, had good sensitivity and was quite easy to tune. All these factors helped increase tremendeously the experimental efficiency.

The spectrometer employed a standard X-band microwave bridge, a klystron locked to the sample cavity, a solid state microwave detector and a reference arm arranged for homodyne detection, (49,52). The AFC klystron generated monochromatic microwave detection at a frequency of 9.2 Ghz and a maximum output power of ~ 200 mwatt. Typically 1.0 mw of power was incident on the cavity. The microwaves were attenuated and guided through a mica window and into a custom built TE_{102} microwave cavity. The wave guide and cavity were both enclosed in the liquid helium cryostat.

The quality factor, or Q, of the cavity determines the response to absorptions. The larger the Q, the more sensitive the cavity is to small changes in the energy absorbed. In these experiments the Q value was between 3500 and 4500, (47). Before deposition the reference arm of the spectrometer was tuned at 4.2K. After deposition, since Q has changed, the spectrometer was again tuned to the new frequency. Detection of resonance

was achieved by balancing the microwaves reflected from the cavity by those from the reference arm. This deviation at resonance and the change in Q was detected with a semiconducting diode.

Proper tuning was essential for obtaining maximum signal to noise ratio, S/N, and resolution. The attenuation level of the reference arm thus determined the biasing and the response of the diode. Both overbiasing and underbiassing the diode would result in deviations from linearality in the response regions. Finally, the phase of the reference arm was used to select only the absorption mode of the resonance for transmission to the detector.

To detect very small changes in the Q of the cavity the magnet was modulated at 100 Khz with a pair of custom made low impedance coils mounted directly on the cavity and maintained at cryogenic temperatures, (47). This field had a peak-to-peak amplitude range of 0.25-5.0 Gauss. The output of the microwave detecting diode was amplified with a 100 Khz band pass filter and sent trough a lock-in amplifier, (phase sensitive detector). Since only a small fraction of random noise was expected to have this frequency the S/N ratio increased and weaker intensity transitions could be well resolved. This phase sensitive detection and modulation is a standard technique used to recover weak signal from noise. The final signal was either filtered by an active low pass filter and plotted on an x-y recorder or digitally stored on a signal averager (TRACOR NORTHERN #1710-AIC) . The sensitivity of the spectrometer was of the order of $5x10^{10}$ spin/Gauss, (49) . The recorder and the signal averager were both interfaced to an IBM-9000 minicomputer (IBM INSTRUMENT,INC) so that spectra stored could be further analyzed.

The electromagnet and power supply used were both from JEOLCO. The electromagnet had custom made flat poles caps 300 mm in diameter, a 90 mm air gap and low impedence water cooled coils which drew 0 to 80 amps to induce fields in the range of 0 to 10 KG. The homogeneity of the field determined the ultimate resolution. It was relatively stable and linear in the range of 3.5 KG ± 1KG used in these experiments although jitters and field drifts did occur. The field strength and recorded spectra were also calibrated with a proton magnetometer (MICROW-NOW, MODEL 515). In addition, the resonance frequency of the cavity was monitored using a microwave frequency counter (Hewlett-Packard, model 5245L plus HP 5255A plug-in). Relative and absolute field positions are judged accurate to within ± 0.2 % and ± 0.5 G respectively, (47).

II.3 The Dewar

Detailed descriptions of the engineering and construction of the liquid helium cryostat have been given elsewhere and only a brief description be given here, (47,52). A schematic of the dewar is shown in fig. (2.2). The dewar consisted of and upper and lower section. The upper section had an outer vacuum jacket followed by a liquid nitrogen reservoir a second vacuum jacket and a liquid helium reservoir of $2^1/2$ liter capacity. The lower section or the "tail of the dewar" had a helium reservoir of 1/2 liter capacity connected to the top reservoir by a variable position valve. The valve allowed helium to flow down from the top reservoir when working near 4K, and evacuation of the tail when conducting temperature dependent work. Finally, there was a length of evacuated waveguide which ran down

along the center of the apparatus and to which was attached the resonance cavity.

Variable temperature work was monitored using a Gallium Arsenide diode in conjunction with a microprocessor based temperature indicator/controller (SERIES 5500, SCIENTIFIC INSTRUMENT, INC). The indicated manufacturer' s precision was ±0.2K, (47). The controller was specially convenient to use and after minor adjustments of the helium gas flow from the upper and lower reservoir fixed temperatures could be attained and maintained for extended periods of time.

All temperature transducers were mounted on a heat exchanger connected to the cavity. Therefore temperatures recorded on the controller were "nominal temperatures" but were not expected to differ by more than ±2K between the two points. Additional sources of heat were from the modulation coils around the cavity, the klystron microwave power dissipated in the cavity walls and conduction through the incoming matrix gases.

II. 4a Resonance Cavity and Target

A microwave resonant cavity is a box fabricated from high-conductivity metals that can sustain oscillations in an number of standing wave configurations called modes. The energy from the klystron is carried down the waveguide in a series of discrete modes for the electric field transverse to the direction of propagation. These modes, are designated TE_{mn}, where TE, stands for transverse electric mode and m and n refer to the number of half wavelength of the electric field parallel to the wide, (a), and narrow, (b), dimentions of the rectangular guide. The mode of longest

wavelength is labelled TE_{10}, and TE_{20} the next highest and so forth. The cavity may also oscillate in a number of modes designated TE_{mnp}, where the p, refers to the number of half cycles of standing waves in the long direction (d).

In any resonant cavity the magnetic and electric waves are 90^0 out of time phase with each other. Thus, when the electric fields are at a maximun, the magnetic fields are zero, and vice versa, (52). For a standing X-band wave guide a = 2.286 cm and b = 1.016 cm. For our experiments a TE_{102} cavity was used, where p = 2. The cavity resonant frequency is then given by eq. (2.1),

$$\frac{2}{\upsilon_0^{res}} = \sqrt{\frac{m^2}{a^2} + \frac{n^2}{b^2} + \frac{p^2}{d^2}} \qquad (2.1)$$

where for our cavity case d = 4.547 cm and $\lambda_o{}^{res}$ = 3.224 cm or υ_o = 9.299 Ghz, (52). Fig. (2.3) shows the diagram of a cavity in the TE_{102} mode, the electric , magnetic field distributions and wall currents. The broad face of the cavity shows, the beginning and ending positions of the electric and a dispalcement current flowing through the center of the loops on the magnetic field. The two fields, and the charges will reverse polarity every cycle. Thus the sample undergoing magnetic dipole transitions is placed in a way such that, (i) it lies in a node of the microwave electric field and, (ii) in the position of maximum magnetic field, (52).

Three different targets were also used and were mounted within the resonance cavity between the modulation coils. The more commonly used target was made of copper 0.010" thick with a hole counterbored in its center to accommodate a 0.094" diameter Quartz window. The first advantage offered by this target was that it showed only one background signal near g =

2 arising from a small amount of organic glue used to hold the Quartz window in place. This background spectrum is shown in fig. (2.4). The second advantage was that the target also allowed UV-Visible optical absorption experiments to be performed on the matrices. The observed free electron value , H_e, was at a field value of 3321.1 ±0.5 Gauss. The two other targets made of sapphire and uniform copper, were less often used, although all clusters presented in this thesis could be made using any of these targets. Background spectra of the sapphire target is shown in fig. (2.5)

II.4b Optical Absorption Detection System

In 1985 a 5' long optical fiber cable (GENERAL FIBER OPTICS,INC,#SS-200) replaced a series of lenses previously used for the optical absorption work. The optical fiber was coupled to the arc lamp using a fiber optics positioner (NRC, MODEL FP-1). Inside the dewar the fiber was held in place by a 1/4" thick Teflon retainer and extended into the resonance cavity just below the target fitted with the quartz window.

The absorption signal was collected through a window fitted atop the wave guide and was then focussed onto the slit of a monochromator (GCA/McPHERSON INSTRUMENT,MODEL EU 700) to which was attached a photo multiplier tube, PMT, (HAMAMATSU CO., MODEL R943-02). The PMT was connected to a two mode single photon amplifier discriminator, (UNI-PHOTON SYSTEM,INC). The analog mode was used for signal optimization while the photon collecting mode for data collection. The monochromator's scanning motor was then interfaced with both the signal averager and the IBM 9000 minicomputer. A block diagram is shown in fig. (2.6).

II. 5a. The Effusion Source

The metals were evaporated from a double chambered Knudsen effusion source. This source was designed for simultaneous evaporation of low and high melting point metals. The two chambers were separated by a water cooled 8 3/32" X 2 1/4" rectangular brass radiation shield. The low temperature chamber, (fig. 2.7), consisted of an oven block made of stainless steel with a tubular hole in which the metals were placed. A 150 watt resistor (HOTTWATT INC.,) fitted in a stainless steel, SS, tube, open at one end and vacuum tight at the other, was used to heat the oven block. A stainless steel slit block that fitted atop the oven block was used to collimate the metal vapors into a beam. A second SS tube with similar configurations was also fitted with a 150 watt resistor was used to heat the slit thus preventing clogging during vaporization. The matrix gas was introduced in the deposition chamber by a 5/4" SS tube fitted with a slit at its end and oriented such that the matrix gas would intersect the metal beams at the surface of the target in the resonance cavity. The high temperature chamber fig. (2.8) consisted of two 7/16" o.d. "OFHC" copper water cooled electrodes. The ends directly in the chamber were fitted with two 3/4" diameter mounts to retain the crucible or "boat" in place. The other ends were connected to high voltage current cables leading to a power supply, (47). A Tantalum (ME-10, R.D. MATHIS INC.,) type boat was used for all experiment, (47).

II. 5b. Radiation Shields

The source was expected to radiate 5000 watts into space and vaporize metals, (i.e. group IB), in the temperature range of 1900^0c. Therefore heat

transfer from the source to the liquid helium cryostat had to be minimized to prevent rapid helium loss during deposition.

The heat input from the low temperature chamber was reduced by a 1/16" thick rectangular 5" X 2 1/4" "OFHC" copper radiation skirt, and 1/8" thick "OFHC" top slit block with a 3/8" X 5/32" aperture directly above the oven block. Also,the heat input from the high temperature chamber was reduced by a curve "OFHC" copper shield and an 1/8" "OFHC" top radiation flange with an aperture 1/4" X 5/32" opening directly above the crucible. A diagram is shown in fig. (2.9). The shields from both chambers were then bolted to the water cooled flat brass shield

Finally, considerable amount of heat generation was expected to in the electrodes. At temperatures above the melting point of copper it is necessary to conduct heat away from the dewar and prevent "melt down". The electrodes were fitted with a 1/4" diameter water inlet and outlet holes. The water cooling reduce this heat input by more than 90 %. Stephan's law, eq. (2.2) can be used to estimate the total heat input from the effusion source,

$$Q_{rad} = \varepsilon \cdot \sigma \cdot SA \, (T^4_{source} - T^4_{sink}) \qquad (2.2)$$

where the emittance, ε, can vary between 0 and 1, σ, Stephan's constant 5.6 $X10^{-12}$ watt cm^{-1} K^{-1}, can be used to estimate the radiative heat input from the source into the liquid helium dewar. The heat transfer to the liquid helium dewar was limited by an 1/8" diameter metal vapor input hole in the liquid nitrogen cooled radiation baffle 2" above the metal vapor source. This shield would absorb about 20% of the 5000 watts or 1000 watts, and limit helium loss of less than 0.2 liter/hr, (52). Since the source was a combination of two previous working sources all other heat transfer considerations are

similar to those described in references, (47,52), except were minor engineering adjustments were made because of space restrictions.

II.6a. Monitoring metal fluxes

Three fluxes were involved in these experiments : The high and low metal fluxes, and the matrix gas flux. Reference, (47), gives a detailed explanation of the gas line input and supporting apparatus. Both metal fluxes were monitored using a commercial quartz deposition monitor (MODEL QM-300, VEECO INSTRUMENTS., INC), with custom built temperature heads, (47,52). The sensor heads were similar to the VEECO VTT 300 except for modification in their cooling system. They were reliable and responded well for all temperatures encountered.

The microbalance reading, are related to metal fluxes incident on the target by appropriate geometric parameters inherent in the nitrogen radiation shield. These geometric factors can be described by eq. (2.3),

$$\text{Flux (cavity)} = 1/3 \text{ Flux (microbalance)} \qquad (2.3)$$

in units of Angstrom per second (Å/s). The weight on the crystal or the number of atoms incident of the microbalance is expressed by eq. (2.4a),

$$N \text{ (atoms/s)} = 6.02 \times 10^{15} A_m (\rho/M) R \qquad (2.4a)$$

where M, is the metal's molecular weight, ρ, it's density, R, the number of atoms on the crystal, and A_m, the exposed area of the crystal measured as, 0.79 cm^2. For the double chambered source eq. (2.4a), is then expressed by eq. (2.4b), after substituting the value of A_m,

$$N = 4.76 \times 10^{15} (\rho/M) R \qquad (2.4b)$$

The number of molecules incident on the target is obtained by multiplying the value obtained from eq. (2.4b) by one third,

$$Z = 1.59 \times 10^{15} \ (\rho/M)\, R \qquad (2.5)$$

Table II.1 gives a list of the metals used in these experiments and their calculated fluxes.

The low temperature metal fluxes were estimated from Nesmeyanov's Tables, (53), that plot vapor pressure vs temperature. More accurate measurements were obtained with the VEECO microbalance retractably mounted on the source flange and parallel to a pinhole in the slit situated between the oven block and the slit spacer. Two thermocouples (OMEGA ENG.,INC) connected in series to multivoltmeters were used to read slit and oven temperatures. These values were then compared with the reference values, (53), and also used to maintain a constant temperature gradient between the slit and oven block to prevent underheating which could cause clogging of the slit passage. The high temperature metal fluxes were monitored by a second VEECO microbalance introduced from the back of the dewar and perpendicular to the direction of the metal beam. The output of both microbalances were connected to a panel fitted with two switches and connected in series with the deposition monitor. The microbalance panel allowed greater convenience in registering the metal fluxes. A block diagram of the apparatus is shown in fig (2.10).

II.6b. "Doing a Run"

The double chambered source was fairly easy to operate and proved to be both reliable and durable. The experiments follow closely the procedures described in references, (47) and (52). The metal fluxes were first monitored at room temperatures and compared with references values. The dewar was always leak checked with a mass spectrometer helium leak detector (VEECO

INSTRUMENTS,INC. MODEL MS-9), without and with the source in place. It was then pre-cooled with liquid nitrogen for approximately 4-5 hours. The helium reservoir was evacuated and pump on until no significant temperature changes due to incomplete nitrogen removal was observed. The next day, the various components were started and liquid helium was then transferred. Within an hour metal fluxes could be generated and set to the required deposition conditions. After various background spectra were taken deposition was initiated. Spectra was taken after each hourly deposition and would continue until no significant increase in signal intensity was observed. Fig. (2.11) and table (2.2), provide a summary of the experiments done, the metals used, the duration of each deposition, the ratio of metal-matrix gas concentration and the deposition temperatures.

Fig. II.1 Block Diagram of the Experimental Apparatus

Outline of the experimental system used for the electron spin resonance spectroscopy of matrix isolated metal clusters. A commercial spectrometer is used to detect the spectra of metal clusters isolated in a nonreactive matrix maintained at low temperatures by the liquid helium cryostat. Additional components included for specific experiments will be presented separately in the following chapter. This diagram was adapted from ref. (52).

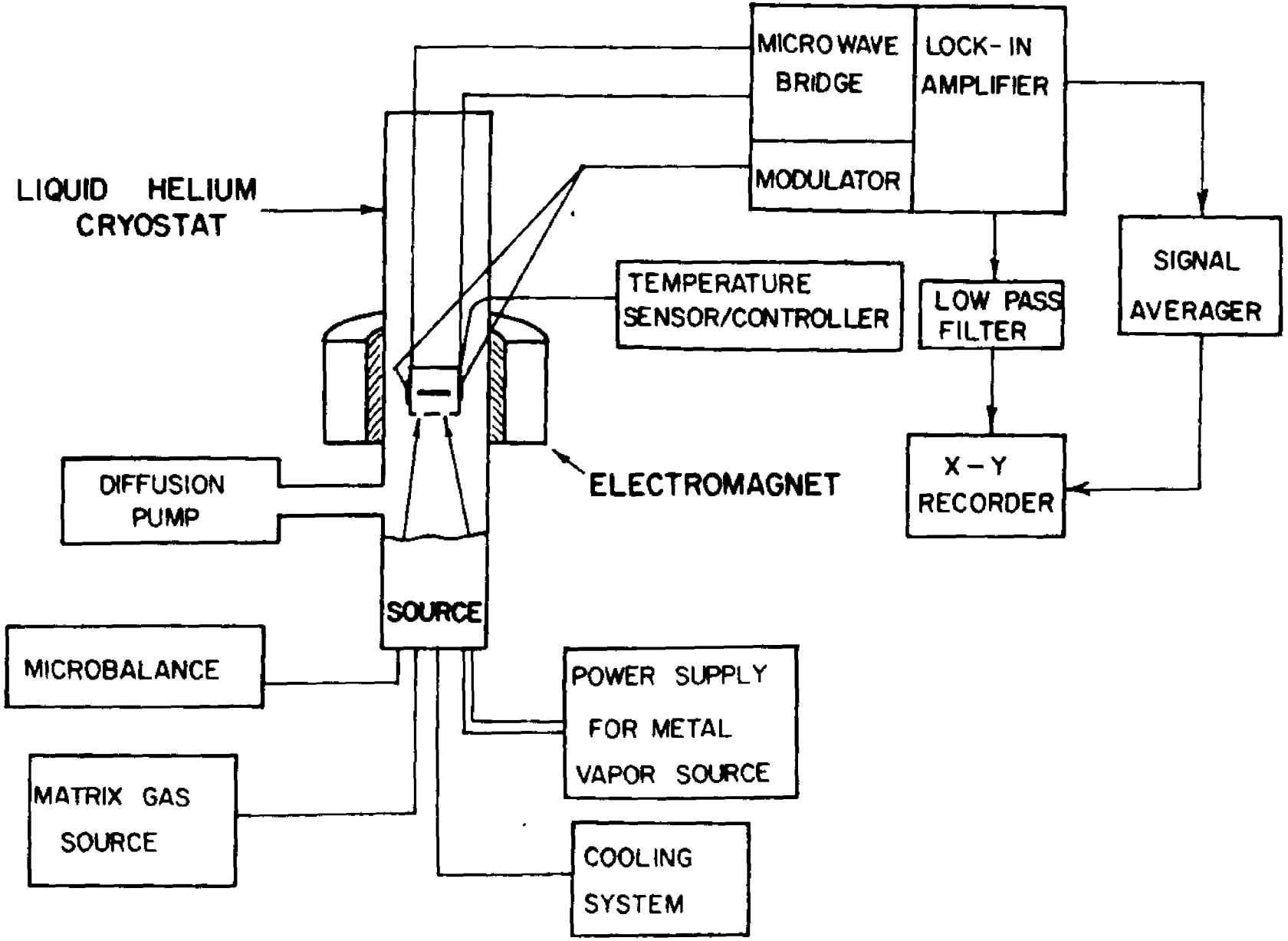
MICRO WAVE BRIDGE
LOCK-IN AMPLIFIER
MODULATOR
LIQUID HELIUM CRYOSTAT
TEMPERATURE SENSOR/CONTROLLER
LOW PASS FILTER
SIGNAL AVERAGER
DIFFUSION PUMP
ELECTROMAGNET
X-Y RECORDER
SOURCE
MICROBALANCE
POWER SUPPLY FOR METAL VAPOR SOURCE
MATRIX GAS SOURCE
COOLING SYSTEM

Fig. II.2. The Liquid Helium Dewar

Lateral cross sectional view of the liquid helium dewar used for these experiments. This diagram was adapted from ref. (52).

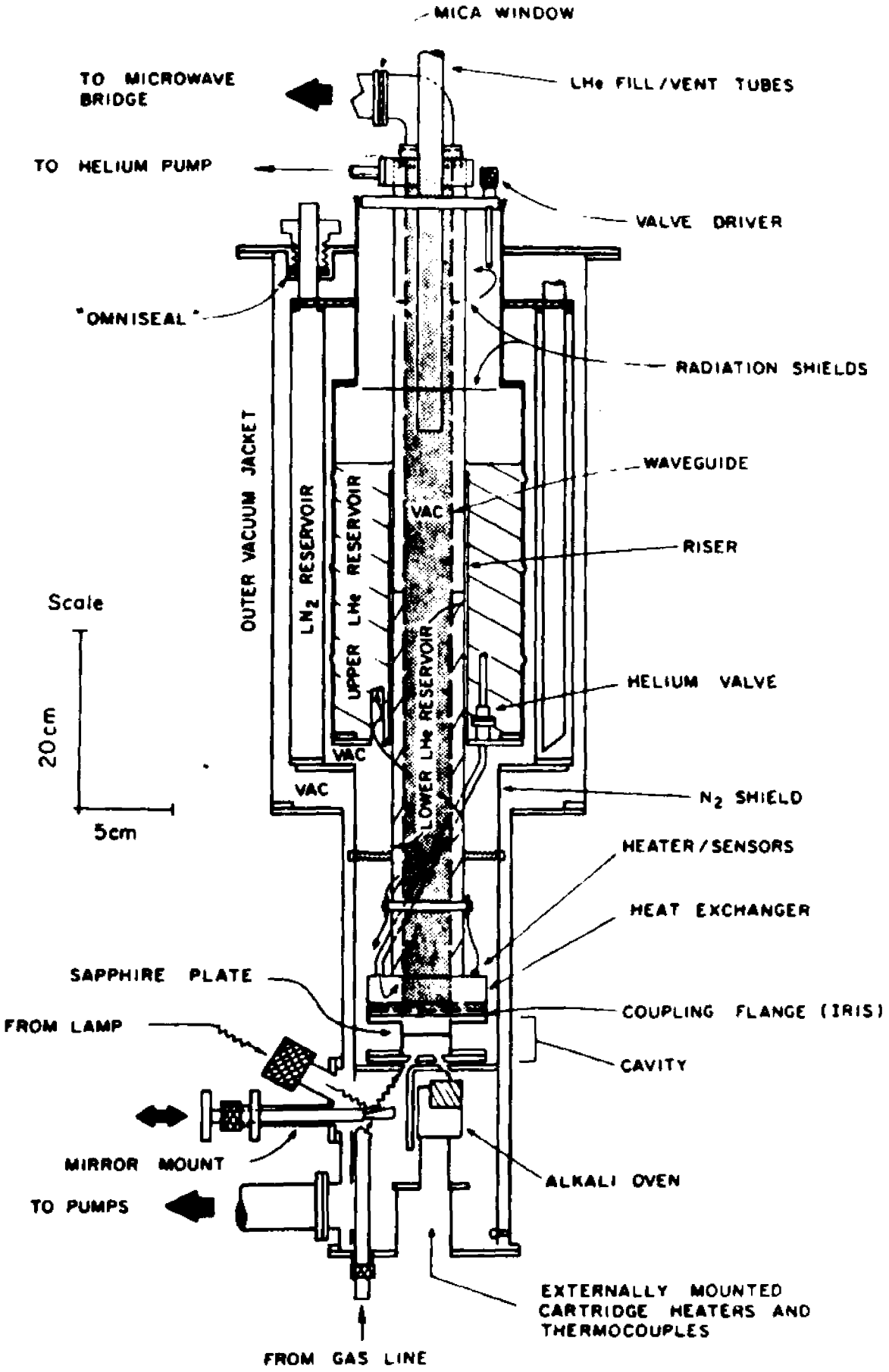
MICA WINDOW
TO MICROWAVE BRIDGE
LHe FILL/VENT TUBES
TO HELIUM PUMP
VALVE DRIVER
"OMNISEAL"
RADIATION SHIELDS
OUTER VACUUM JACKET
LN2 RESERVOIR
UPPER LHe RESERVOIR
LOWER LHe RESERVOIR
VAC
WAVEGUIDE
RISER
Scale
20cm
5cm
HELIUM VALVE
N2 SHIELD
HEATER/SENSORS
HEAT EXCHANGER
SAPPHIRE PLATE
FROM LAMP
COUPLING FLANGE (IRIS)
CAVITY
MIRROR MOUNT
ALKALI OVEN
TO PUMPS
EXTERNALLY MOUNTED CARTRIDGE HEATERS AND THERMOCOUPLES
FROM GAS LINE

Fig. II.3 Rectangular Cavity in TE_{102} Mode

Adapted from reference (52).

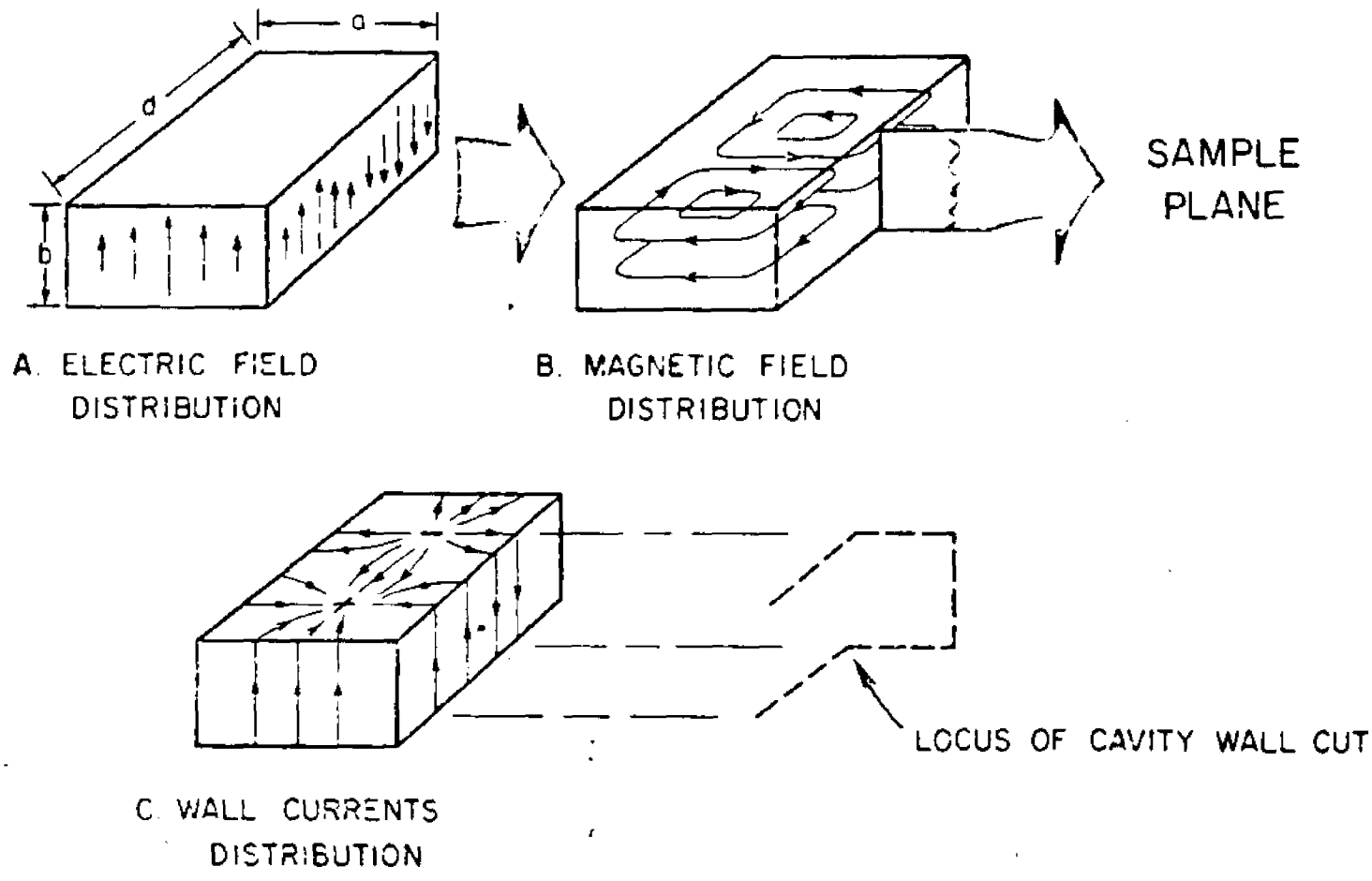

Fig. II.4 Background Spectrum of the copper Target

ESR spectrum of the copper plate used as the deposition target for most of these experiments presented in this dissertation. The signal about g = 2, probably arises from the organic glue used to retain the optical window in place. This spectrum is 700 Gauss wide and centered about g = 2.

Fig. II.5 Background Spectrum of the Sapphire Target

ESR spectrum of impurities in a sapphire plate used as a deposition target in these experiments. This target was mostly used for the mixed-metal cluster experiments. The spectrum is 500 Gauss wide and centered about g = 2.

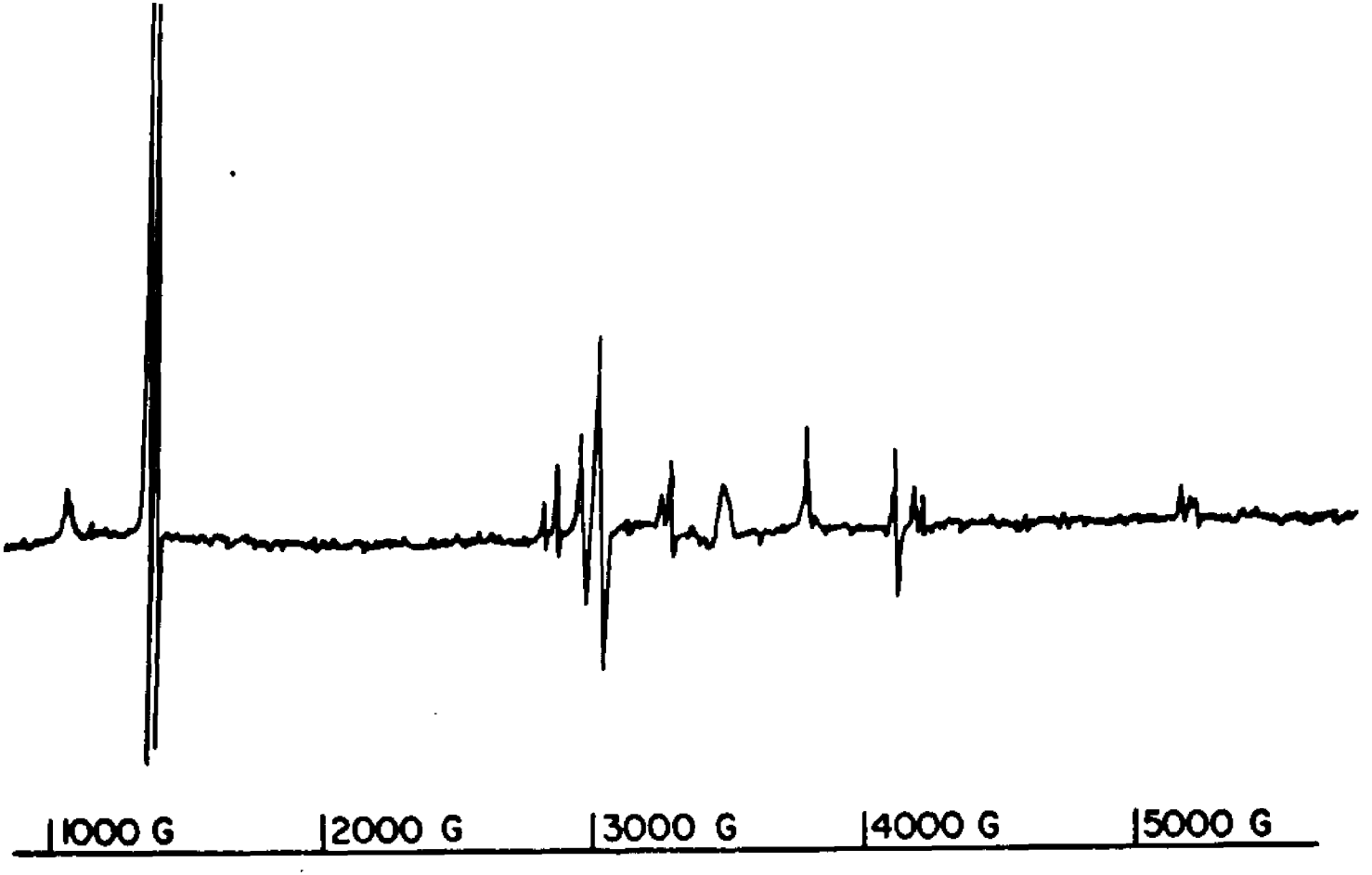

Fig. II.6 Block Diagram of the Optical Absorption System

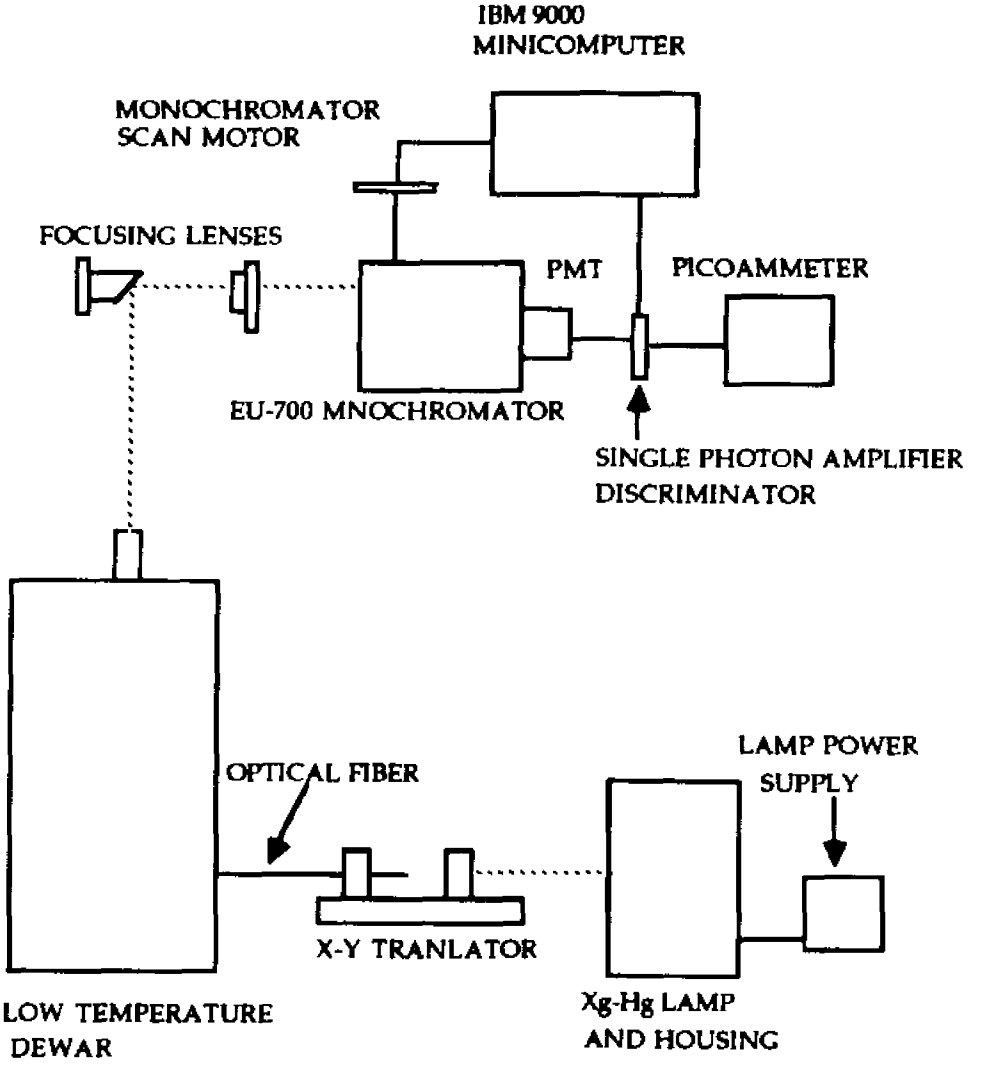

Fig. II.7 Low Temperature Chamber of The Effusion Source

Front and side view of the low temperature chamber used to generate alkali metal fluxes.

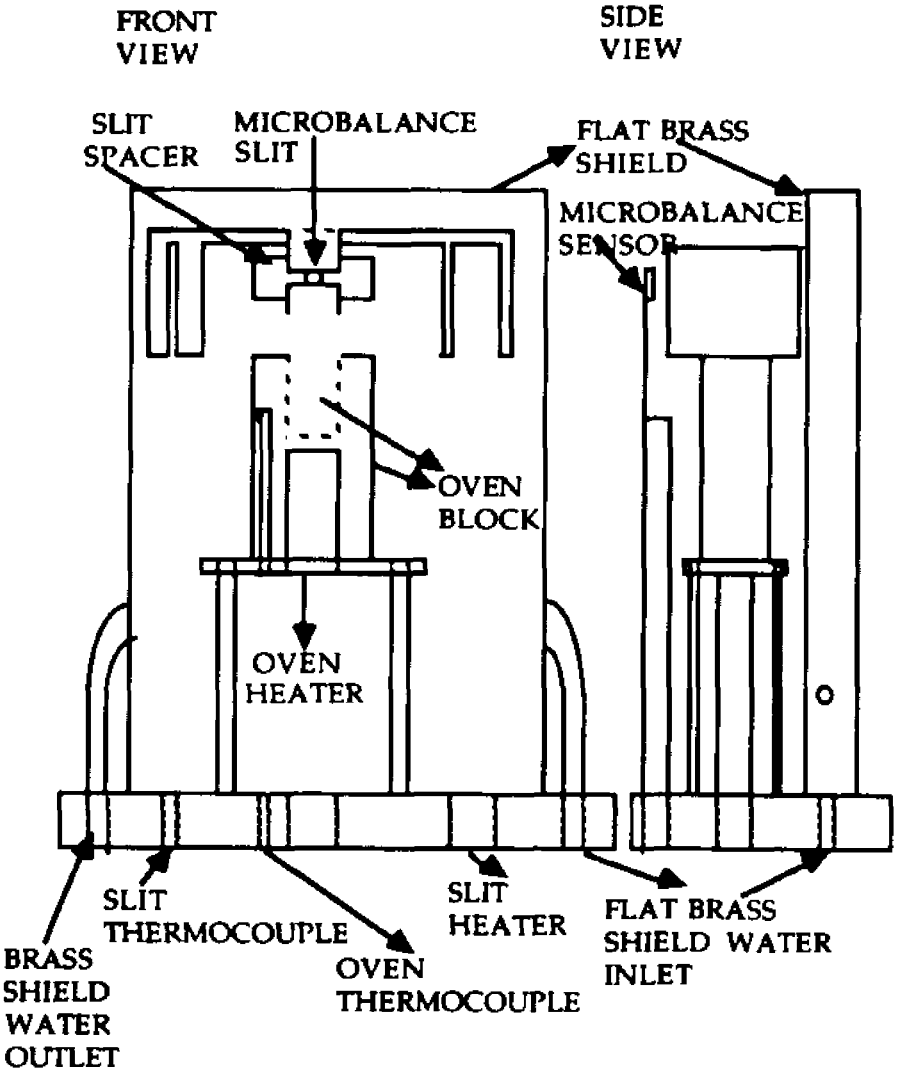

Fig. II.8 High Temperature Chamber of The Effusion Source

Front and side view of the high temperature chamber used to generate the Group IB and Group IIA metal fluxes.

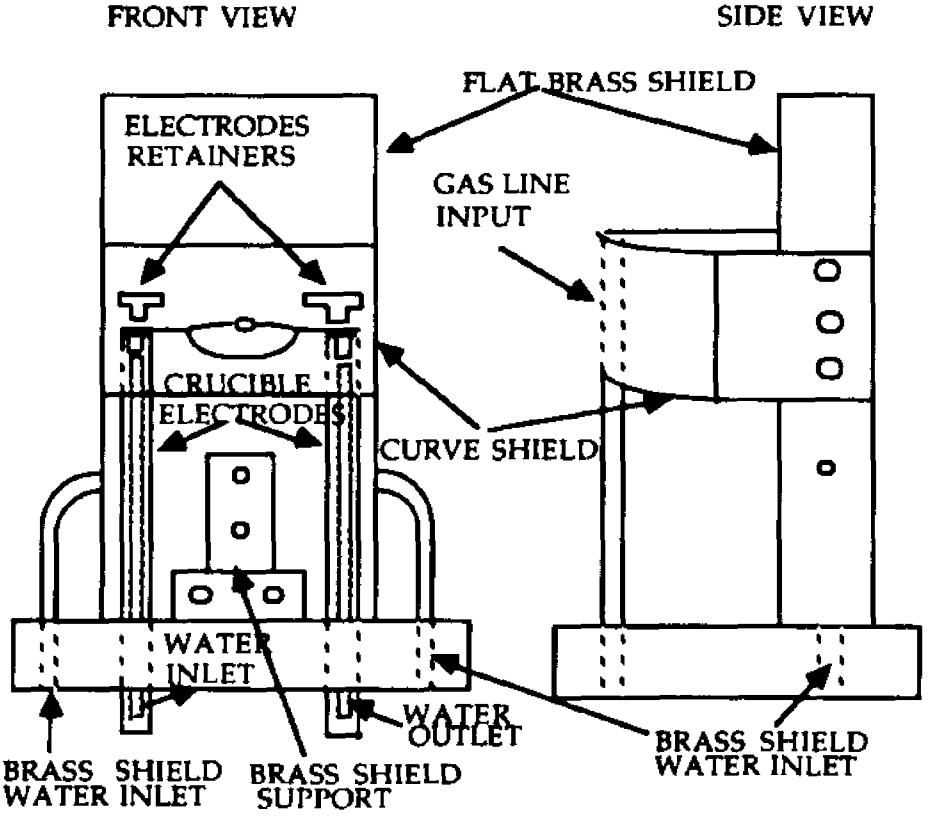

Fig. II.9 Radiation Shields

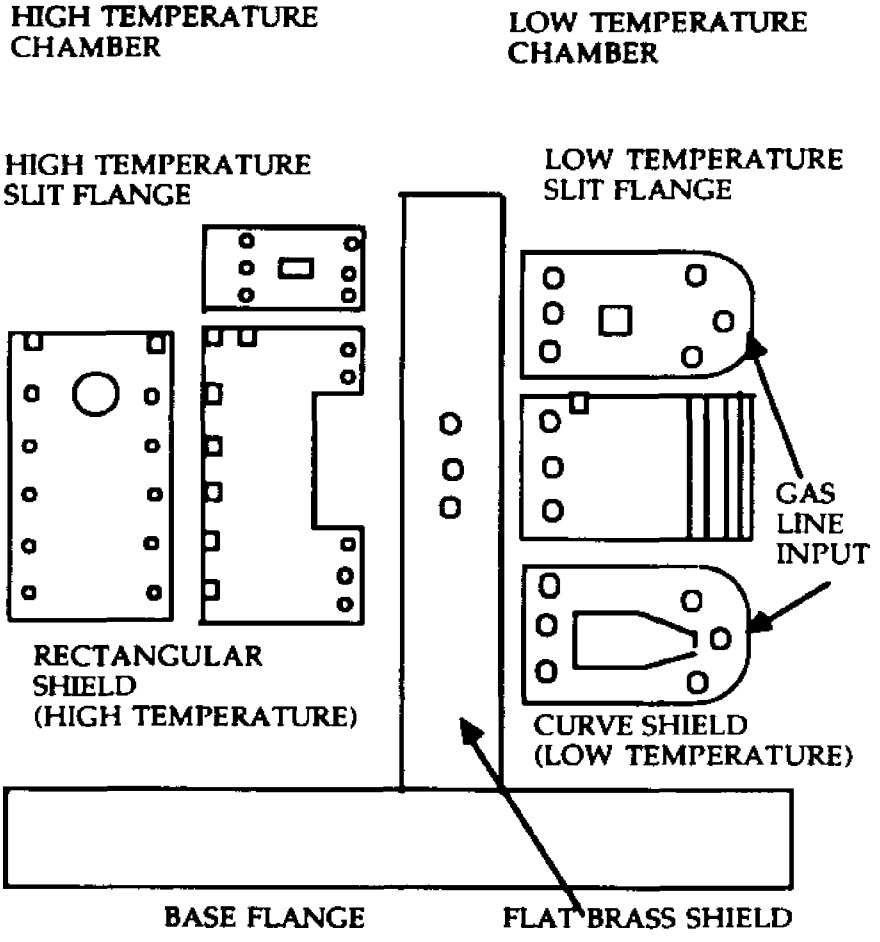

Fig. II.10. Flux Monitor Assembly.

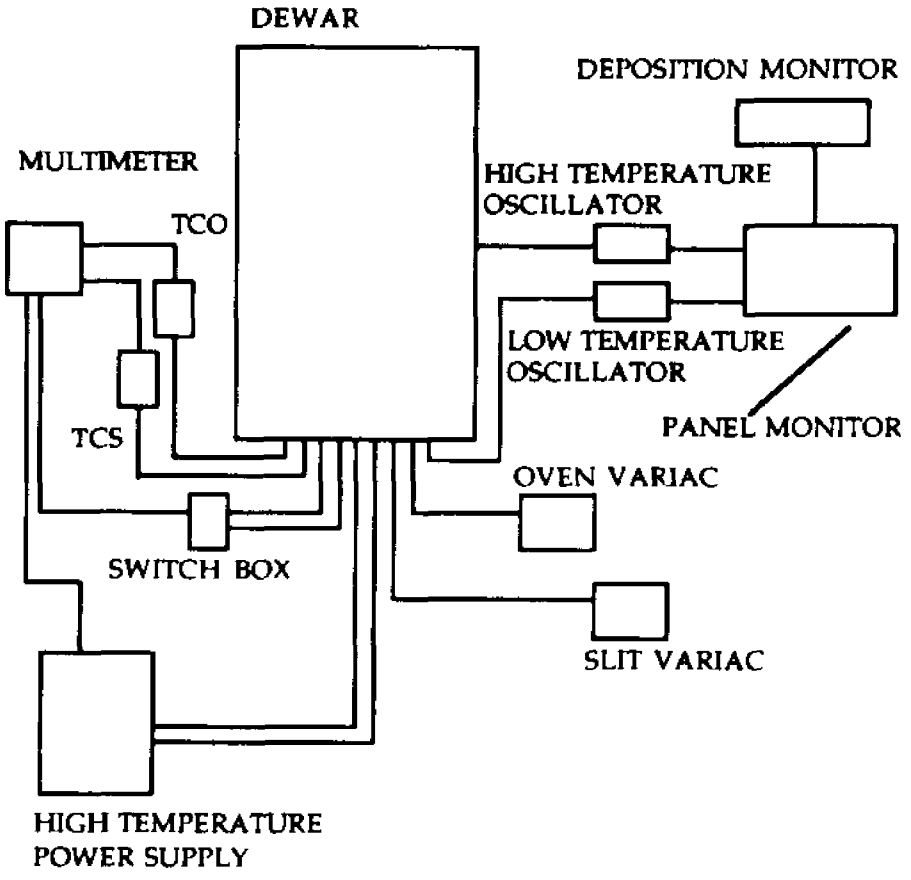

Fig.II.11. Sample of Matrix Growth vs. Time Taken From The Mixed-metal Cluster Experiments.

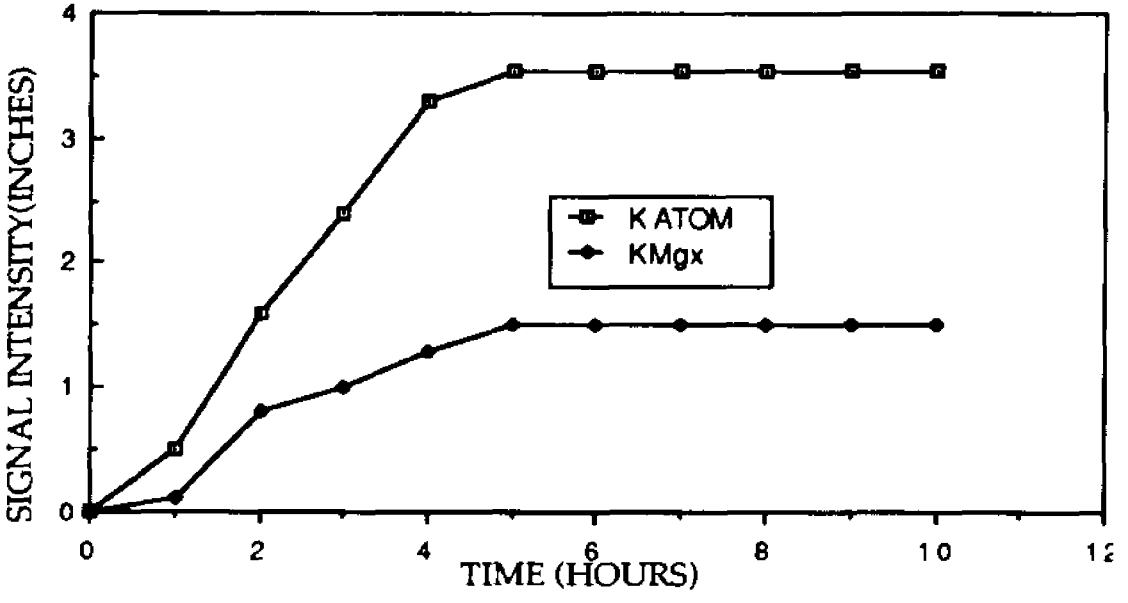

TABLE.II.1. Calculated metal fluxes for the double chambered source, with the entire surface of the microbalance exposed to the metal vapor fluxes.

Metals	ρ^a	M^b	N/R^c	Z/R^d
Ag	10.5	107.80	4.63(14)	1.54(14)
Au	18.9	197.00	4.56(14)	1.53(14
Na	0.971	22.99	2.02(14)	6.72(13)
K	0.870	39.10	1.05(14)	3.54(13)
Mg	1.74	24.31	3.40(14)	1.14(14)
Ca	1.55	40.08	1.84(14)	6.13(13)
Sr	2.54	87.62	1.37(14)	4.61(13)
Ba	3.50	137.33	1.21(14)	4.04(13)

a. Smithsonian Tables. Units of g cm^{-3} (54).

b. Units of g mol^{-1}.

c. Atoms per sec for a reading of R = 1 Å sec^{-1}.

d. Flux incident on the microbalance surface, taken as 1/3 (N/R).

TABLE II.2. Summary of Experiments and Depositions Conditions.

#	EXP	METAL[a]	MATRIX[a] GAS	METAL/GAS[b] RATIO	DEP.[c] TIME	DEP.[d] TEMP.
1	ESR	Ag	N_2	5:800	4	4
2	ESR	Ag	Ar	5:800	3	4
3	ESR	Ag	Xe	6:800	3	5.8
4	ESR	Ag	Kr	5:800	2	5.4
5	ESR	^{107}Ag	N_2	5:800	3	5.3
6	ESR	^{107}Ag	Ar	5:750	2	5.4
7	ESR	Au	N_2	5:840	3	5.5
8	OA	Au	N_2	5:800	2	5.5
9	OA	Au	N_2	5:800	3	5.5
10	ESR-0A	^{107}Ag	Kr	5:800	3	5.5
11	ESR-0A	^{107}Ag	N_2	5:800	3	5.5
12	ESR-0A	^{107}Ag	N_2	5:800	3	5.5
13	ESR-0A	^{107}Ag	Ar	5:800	3	5.5
14	ESR-0A	^{107}Ag	Ar	5:800	3	5.5
15	ESR	Cu	Ar	5:900	3	5.0
16	ESR-0A	Na-Ag	Ar	1:5:900	3	5.0
17	ESR-0A	Na-Ag	Ar	1:5:800	3	5.0
18	ESR-0A	Na-Ag	Ar	1:5:800	3	5.0
19	ESR-0A	Na-Ag	Ar	1:5:800	3	5.0
20	ESR-0A	Na-Ag	Ar	1:5:800	3	5.2
21	ESR	K-Mg	Ar	1:5:600	3	6.2

TABLE II.2. (continued)

#	EXP	METAL[a]	MATRIX[a] GAS	METAL/GAS[b] RATIO	DEP.[c] TIME	DEP.[d] TEMP.
22	ESR	K-Ba	Ar	1:5:600	3	6.2
23	ESR	Na-Mg	Ar	1:5:600	3	6.2
24	ESR	Na-Mg	Ar			
25	ESR	Na-Mg	Ar	1:5:600	3	6.4
26	ESR	Na-Mg	Ar	1:5:600	3	6.4
27	ESR	Na-Mg	Ar	1:5:600	4	6.4
28	ESR	Na-Mg	Ar	1:5:600	3	6.4
29	ESR	Na-Mg	Ar	1:5:600	3	6.0
30	ESR	Na-Mg	Ar	1:5:600	3	5.0
				1:8:600	2	6.2
				1:5:600	4	6.2
				1:5:600	6	6.2
				1:10:600	2	6.2
30	ESR	Na-Mg	Ar	1:3:600	6	6.2
31	ESR	Na-Mg	Ar	1:5:600	3	6.2
32	ESR	K-Mg	Ar	1:5:600	3	6.2
33	ESR	K	N_2	1:800	3	6.2
34	ESR	K-Mg	N_2			
35	ESR	K-Mg	N_2	1:5:800	3	6.2
36	ESR	K-Mg	Ar	1:5:600	3	6.2
37	ESR	Na-Mg	Ar	1:5:600	3	6.2

TABLE II.2. (continued)

#	EXP	METAL[a]	MATRIX[a] GAS	METAL/GAS[b] RATIO	DEP TIME	[c]DEP.[d] TEMP.
38	ESR	Na-Mg	Ar	1:5:600	3	6.2
39	ESR	Na-Mg	Ar	1:5:600	3	6.2
40	ESR	K-Mg	Ar	1:5:600	3	6.2
41	ESR	K-Mg	Ar	1:5:600	3	6.2
42	ESR	K-Mg	Ar	1:5:600	3	6.2
43	ESR	K-Ba	Ar	1:5:600	3	6.2
44	ESR[e]	Ag	N2	5:800	3	6.2
45	ESR[e]	Ag	N_2	5:800	3	6.2
46	ESR	K-Ca	Ar	1:5:600	3	6.2
47	ESR	Na-Sr	Ar	1:5:600	3	6.2
48	ESR	K-Sr	Ar	1:5:600	3	6.2
49	ESR	K-Sr	Ar	1:5:600	3	6.2
50	ESR	Na-Sr	Ar	1:5:600	3	6.2
51	ESR	Na-Ba	Ar	1:5:600	3	6.2
52	ESR	Au	N_2	5:800	3	5.5
53	ESR	Au	N_2	5:800	3	5.5
54	ESR	Na-Ba	Ar	1:5:600	3	6.2

TABLE II.2. (continued)

a. Material	Company	
K,Na	Gallery,	99.95%
Kr,Xe	Alpha,	99.995%
Ar	Airco,	99.9998%
Ag,Au,Cu	Alpha,	99.9999%
Ag(107)	USDOE, Oak Ridge National Laboratories.	99%
Mg,Ca	Æsar,	99.8%
Ba,Sr	Alpha	99%

b. Micron pressure units. $1\mu = 10^{-3}$ Torr for the matrix gas. $Åsec^{-1}$ units for the metals where $1\mu \sim 2\ Åsec^{-1}$.

c. Hour time units.

d. Kelvin temperature units.

e. A UV cut-off filter at 350 nm was used throughout the deposition.

III. THEORETICAL

III.1. Introduction

Electron Spin Resonance, ESR, spectroscopy is one of the methods used in the study of the interaction of paramagnetic species with an applied magnetic field. It monitors the absorption of radiation and the accompanying resonance conditions when these paramagnetic atoms or molecules interacting with the applied field change their energy states. The previous chapter covered the experimental factors involved in the generation of these species to be studied. This chapter will briefly review the theory useful for the analysis of an E.S.R. spectrum. Many texts and articles cover these theories with varying degrees of rigor and detail, (55-61).

III.2a. Resonance Condition

A simple description of a paramagnetic specie interacting with an applied magnetic field can be given by using a classical description of a bar magnet. A charge, spinning or rotating, behaves like a magnet with its poles along the axis of rotation. Therefore, electrons in atoms or molecules are expected to behave like magnetic dipoles and will align themselves in the direction of an applied external magnetic field so that their internal fields are either parallel or anti-parallel with respect to the external field. The energy difference, ΔE, between the two alignment is a function of the field strength. For an isolated electron the magnetic moment, μ_e, is given by eq. (3.1),

$$\mu_e = -g_e \beta_e \cdot S \qquad (3.1)$$

where, S, is the spin angular momentum vector of the electron, g_e, a

dimensionless constant called the electron free g-factor, (2.00232), and, β_e is the electronic Bohr magneton, (9.27410×10^{-21} erg-G^{-1}). The interaction of the electronic moment and an applied field, **H**, is given by the electronic Hamiltonian in eq.(3.2),

$$H_e = -\mu_e \cdot H \tag{3.2}$$

If the applied field is the z direction, H_Z, then eq.(3.2) becomes,

$$H_e = g_e \beta_e H_z M_S \tag{3.3}$$

where Ms is the quantized spin momentum, **S**, into its two allowed states, $M_S = (\pm 1/2)$.

The energy difference, ΔE, is given by eqs. (3.4) and (3.5),

$$E_{+1/2} = +1/2\, g_e \beta_e H_z, \qquad E_{-1/2} = -1/2\, g_e \beta_e H_z \tag{3.4}$$

$$\Delta E = g_e \beta_e H_z \tag{3.5}$$

Transitions between the two levels can be induced when the resonance condition is met and the difference between the 2 energy levels coincide with an electromagnetic radiation field of frequency, υ.This condition is described by eq. (3.6),

$$\Delta E = h\upsilon = g_e \beta_e H_z \tag{3.6}$$

where h, is Planck's constant. For these experiments, υ, was in the X-band region of the spectrum ~9.2 Ghz and the field strength, H_z, was ~3300 G.

A similar but much smaller effect is observed for a nucleus with a spin angular momentum, **I**, interacting with an external magnetic field, **H**, and magnetic moment, μ_n. An equation analogous to (3.1) is obtained,

$$\mu_n = g_n \beta_n I \tag{3.7}$$

with the applied field again in the z direction, the nuclear Hamiltonian can be expressed by eq. (3.8),

$$H_n = g_n \beta_n H_z M_I \tag{3.8}$$

where g_n is the nuclear g factor, β_n is the nuclear Bohr magneton, (5.05095×10^{-24} erg-Gauss^{-1}), and M_I the allowed levels of the nuclear spin, I, in the applied magnetic field.

In atoms or molecules there is an additional interaction that occurs when the electronic and nuclear spins, S and I, couple to form what is called the hyperfine interaction, described by the hyperfine Hamiltonian in eq. (3.9a),

$$H_{hf} = \mathbf{S}\cdot\mathbf{A}\cdot\mathbf{I} \tag{3.9a}$$

The spin vectors are couple thru the symmetric tensor, **A**. Equation (3.9a) is then expanded,

$$H_{hf} = S_x A_{xx} I_x + S_y A_{yy} I_y + S_z A_{zz} I_z \tag{3.9b}$$

and the symmetry of the tensor corresponds to the symmetry of the local spin distribution about the nucleus, (63). Other well known interactions were omitted if they did not contribute to the spectral analysis of the work that will be presented in this dissertation These interactions are covered in most of the previously cited references of which, (57) was found to be the most explicit and easiest to comprehend.

III.2b. Spin Hamiltonian

The interactions described in the previous section are then combined into a single equation known as the Spin Hamiltonian,

$$H_s = \beta_e g_e H_z M_S + \beta_n g_n H_z M_I + \mathbf{S}\cdot\mathbf{A}\cdot\mathbf{I} \tag{3.10}$$

The first term is called the electronic zeeman interaction and describes the flip of the electron's spin and gives rise to a resonance near υ = 9.2 Ghz. It also defines the center of the spectrum and has the largest order of

magnitude, ~1cm^{-1}.The second term called the nuclear zeeman is three orders of magnitude smaller then the electronic zeemam, ~ 10^{-3} cm^{-1},is usually neglected. The last term called the hyperfine interaction with an order of magnitude ~ 10^{-1} - 10^{-3} cm^{-1}, splits the resonance into several components. Furthermore the tensor **A**, can be separated into two terms. The first called the isotropic of fermi contact term, A_{iso}, and the second called the anisotropic or dipolar term, A_{dip}. Rewriting the hyperfine Hamiltonian (3.9a), we have,

$$H_{hf} = [A_{iso} + A_{dip}]\, \mathbf{S}\cdot\mathbf{I} \tag{3.11}$$

The Fermi term arises from the interaction of the nuclear spin, **I**, with induced electric fields at the nucleus produced by the electric current of the spinning electron. The isotropic Hamiltonian is then expressed by eq.(3.12),

$$H_{iso} = a\, \mathbf{I}\cdot\mathbf{S} = a(I_xS_x+I_yS_y+I_zS_z) \tag{3.12}$$

where a, is the isotropic hyperfine constant and equals,

$$a = \frac{8}{3} g_e \beta_e g_n \beta_n |\Psi(0)|^2 \tag{3.13}$$

and is proportional to the squared amplitude of the wave function at the nucleus. Since the expression is integrated over the coordinate of the electron, contact interaction can only occur when the electron has a finite probability density at the nucleus, i.e. no nodes at the nucleus or an s-character.

The dipolar interaction arising from the coupling between the magnetic moments of the electron and the nucleus, μ_e and μ_n, is similar to the coupling of two bar magnets. The classical interaction energy, E, is given by eq. (3.14),

$$E = \frac{1}{r^3}(\mu_e \cdot \mu_n) - \frac{1}{r^5}(\mu_e \cdot r)(\mu_n \cdot r) \qquad (3.14)$$

where r, is the radius vector from the two magnetic moments, and r, is its magnitude. To obtain the quantum mechanical version of (3.14), eqs. (3.1) and (3.7) are substituted into eq. (3.14) such that the dipolar Hamiltonian is expressed by eq. (3.15),

$$H_{dip} = -g_e\beta_e g_n\beta_n\left(\frac{1}{r^3}(I \cdot S) - \frac{3}{r^5}(I \cdot r)(S \cdot r)\right) \qquad (3.15)$$

The anisotropy arises from the orientation dependence of the radius vector and eq. (3.15), can be rewritten in scalar form,

$$H_{dip} = -g_e\beta_e g_n\beta_n\left(\frac{1}{r^3}(1 - \cos^2 \varnothing) \cdot I \cdot S\right) \qquad (3.16)$$

and ø is the angle between the axis of the dipoles and the line joining them. Since the electron orbital motion is not static r and ø are constantly changing therefore integration is over a spatial average of the orientation dependent term over the whole electronic orbital, i.e. $<(1\text{-}3\cos^2\text{ø})/r^3>_{av}$, (58).

The anisotropic hyperfine constant a', is then expressed by eq. (3.17),

$$a' = g_e\beta_e g_n\beta_n < \left(\frac{1 - 3\cos^2\varnothing}{r^3}\right) >_{av} \qquad (3.17)$$

and the term $<(1\text{-}3\cos^2\text{ø})/r^3>_{av} = 0$ for spherically symmetric orbitals.

III.2c Transition Field Positions

A general solution of the Spin Hamiltonian, eq. (3.10), can be obtained by using the basis function $|S,M_S,I,M_I>$, (64), and perturbation theory, (57). For the hyperfine interaction equations (3.11) and (3.12), the I_zS_z terms will give the first order hyperfine energies by perturbing the zero order wave

functions and the remaining terms, I_xS_x and I_yS_y, will produce the second order hyperfine energies by mixing the remaining two wave functions. The Spin Hamiltonian can then be block diagonalyzed by properly ordering this basis function into a set of pure states represented by 1X1 matrices and a series of mixed states represented by 2X2 matrices. The diagonal elements are given by eqs. (3.18a) and (3.18b),

$$\begin{aligned}<S,+M_S,I,+M_I \mid \boldsymbol{H}_s \mid S,+M_S,I,+M_I> = \\ g_e\beta_eH_z+M_S + g_n\beta_nH_z+M_I + \\ (A_{iso}-2A_{dip})+M_S-M_I\end{aligned} \tag{3.18a}$$

and,

$$\begin{aligned}<S,-M_S,I,-M_I \mid \boldsymbol{H}_s \mid S,-M_S,I,-M_I> = \\ g_e\beta_eH_z-M_S + g_n\beta_nH_z-M_I + \\ (A_{iso}-2A_{dip})-M_S-M_I\end{aligned} \tag{3.18b}$$

The off-diagonal elements are given by eq. (3.19a) and (3.19b),

$$\begin{aligned}<S,M_S,I,M_I \mid \boldsymbol{H}_s \mid S,M_S-1,I,M_I+1> = \\ 1/2\{(S+M_S)(S-M_S+1)(I-M_I)(I+M_I+1)\}^{1/2}(A_{iso}+A_{dip})\end{aligned} \tag{3.19a}$$

and,

$$\begin{aligned}<S,M_S,I,M_I, \mid \boldsymbol{H}_s \mid S,M_S+1,I,M_I-1> = \\ 1/2\{(S-M_S)(S+M_S-1)(I+M_I)(I-M_I-1)\}^{1/2}(A_{iso} + A_{dip})\end{aligned} \tag{3.19b}$$

For the case of $M_S= \pm 1/2$, the energy levels are given by eq. (3.20),

$$\begin{aligned}E(\pm 1/2,I,M_I) = -1/2\,(2\Delta_nM_I + 1/2\,a \pm \Delta_n) \\ \pm 1/2\{(\Delta_e+\Delta_n)^2 + 2a\,(\Delta_e+\Delta_n)(M_I\pm 1/2) \\ + a^2\,(I+1/2)^2\}^{1/2}\end{aligned} \tag{3.20}$$

where $\Delta_e= g_e\beta_eH_Z$ and $\Delta_n= g_n\beta_nH_z$ and a, the hyperfine constant.

Resonances are observed when the sweeping static field, **H**, lifts the

degeneracy of the magnetic states when,

$$h\upsilon = E(+1/2,I,M_I) - E(-1/2,I,M_I) \qquad (3.21)$$

Transitions between these levels is then accomplished by a second time dependent oscillating field, $H_{osc} = 2(\Delta_e S_j - \Delta_n I_j)\cos\omega t$, produced in the cavity by the klystron and oriented perpendicular, i.e. j = x direction, to the static field. The transition probability can be expressed by eq. (3.22),

$$P = |g_e\beta_e\langle M_S,M_I | I\cdot H_{osc} | M_S,M_I\rangle|^2 \qquad (3.22)$$

If S_x, is expressed by the ladder operators, $S_x = 1/2(S^+ + S^-)$, then $S_x | M_S\rangle = 1/2$ $\{(M_S - 1) + (M_S + 1)\}$ and all other matrix elements will vanish. A similar treatment can be done with I_x, resulting with the allowed selection rules of $\Delta M_S = \pm 1$ and $\Delta M_I = 0$.

Equation 3.21 can then be expressed is terms of the sweeping field H(m), by substitution of eq. (3.20), changing units and rearranging, we have,

$$H(M_I) = - M_I\, a/ (1-a^2/4)$$
$$\pm\{M_I^2a^2/(1-a^2/4) + 1-a^2(I+1/2)^2/(1-a^2/4)\}^{1/2} \qquad (3.23)$$

where $H(M_I)$ is the observed field position between 2 states with equal M_I, in units of $(\Delta_e\Delta_n/h\upsilon)$, and, a the hyperfine splitting in units of $a/h\upsilon$. A plot of $H(M_I)$ vs is shown is fig. (3.1) for I = 3/2. At all points on this curve the resonance conditions are met and the three labeled regions are functions of the field strength. These regions are,

(i) Weak Field : the dominant term is the isotropic hyperfine interaction,i.e $a\,\mathbf{I}\cdot\mathbf{S} > g_e\beta_e\,\mathbf{H}\cdot\mathbf{S}$, which couple the spin vectors S and I into a resultant angular momentum, F = (I+S), with its (2F+1) projections given by M_F= F,F-1,.....,-F.

(ii) Strong Field : the dominant term is the electronic zeeman, i.e, $g_e\beta_e$

$\mathbf{H \cdot S} > \mathbf{a\, I \cdot S}$, and decouples **I** and **S** making them good quantum numbers with their projections M_I and M_S split into (2I+1)(2S+1) levels. In this case eq. (3.23) cannot be approximated and an exact solution known as the Breit-Rabi equation, (62), is required.

(iii) Medium Field : the zeeman and hyperfine terms are of the same order and rather than using an exact solution a binomial series expansion of the square root terms in eq. (3.23) is done resulting in a power series expansion given by eq. (3.24) in unit of Gauss with the nuclear moments neglected,

$$\begin{aligned} H(M_I) = (g_e/g_o)H_e + (g_e/g_o)aM_I \\ + (g_e/g_o)^2\, a^2[I(I+1 - M_I^2)]\ /2H(M_I) \\ +(g_e/g_o)^3\, a^3[M_I^2(M_I+1/2-I(I+1)]\ /2H(M_I) \end{aligned} \qquad (3.24)$$

H_e is the resonant value for the free electron, 3312.2 Gauss, g_e is the free electron g-value, g_o is the value for the electron in the atom, and, a, the hyperfine constant . A zeemam energy diagram for the case of I = 3/2 is shown in fig. (3.2).

III.3. Breit-Rabi Equation

For molecules with large hyperfine values, Au_3, (65), or with very large hyperfine values, Cu_3, (66), an exact solution of the Spin Hamiltonian is desired instead of further expansion of eq. (3.24). The Breit-Rabi equation, (62), is often used to analyze molecules that fall within these two cases. Applications of this equation has been used by many workers since the original work was presented, (60,63). The equation will be used in this thesis to analyze a system with a large hyperfine at one nuclei and little or no

hyperfine at the remaining nucleus. An equation similar to eq. (3.23) is obtained which gives the energy levels, $E(\pm M_S, M_I)$, over all field positions and using the strong field case where I and S are good quantum numbers, Paschen-Back effect, we have eq. (3.25),

$$\eta(M_I) = \frac{M_I a}{\left(1 - \frac{a^2}{4}\right)} \pm \left[\frac{M_I^2 a^2}{\left(1 - \frac{a^2}{4}\right)}\right] + 1 - a^2\left[\frac{\left(I + \frac{1}{2}\right)}{1 - \frac{a^2}{4}}\right] \tag{3.25}$$

where $\eta = g_e\beta_e H/h\upsilon$, and $a = A/h\upsilon$. For the case where $M_I = \pm I = \pm 3/2$, eq. (3.25) becomes,

$$\eta(\pm I) = \frac{(-2 \pm (2I + 1)a)}{(-2 \pm a)} \tag{3.26}$$

If $h(\pm I) = H_\pm/H_o$ and $a = (g_e/g_o)A/H_o = a/H_o$, where $H_o = h\upsilon/g_o\beta_e$ and $H_\pm$ are the low and high field transitions respectively, eq. (3.26) has now been converted from ergs to units of Gauss. The hyperfine, a, and the center field position H_o, can be obtained by substituting these terms in eq. (3.26) and we now have,

$$\left(\frac{H_\pm}{H_0}\right) = \left[\frac{-2 \pm (2I + 1)a}{H_0}\right] + \left(\frac{-2 \pm a}{H_0}\right) \tag{3.27}$$

which in terms of the low and high field transitions gives,

$$H_\pm = \frac{2H_0(-H_0 \pm 2a)}{(-2H_0 \pm a)} \tag{3.28}$$

and this equation gives a quadratic in terms of H_o or a. When solved in therms of H_o we have,

$$H_0 = h_+ \sqrt{h_+^2 + 3ah_-} \tag{3.29}$$

where $a = 3H_0h_+/4H_0\text{-}h_+$, and $h_+ = 1/2\,(H_+ + H_-)$ and $h_- = 1/3\,(H_- - H_+)$. Substitution of the hyperfine term into eq. (3.30) then gives the Breit-Rabi equation in this simple working form,

$$H_0 = \frac{5}{8}h_+ \pm \frac{3}{8}\sqrt{\left(h_+^2 + 4h_-^2\right)} \tag{3.30}$$

For the work presented in this dissertation equation (3.24) was used to analyze the silver, and the mixed-metal spectra. Also, expansion to the a^3 was sufficient to determine the line positions for both previously mentioned species. The Breit-Rabi equation, (3.31) was used to analyze the gold spectra and to double check the silver work.

Fig. III.1. Transition Field Diagram

Transition fields, hf vs. H, for ^2S atom with I = 3/2 are plotted. The bold lines indicate combinations of the hyperfine value and external magnetic field strength which fulfill the resonance condition. Adapted from ref. (47).

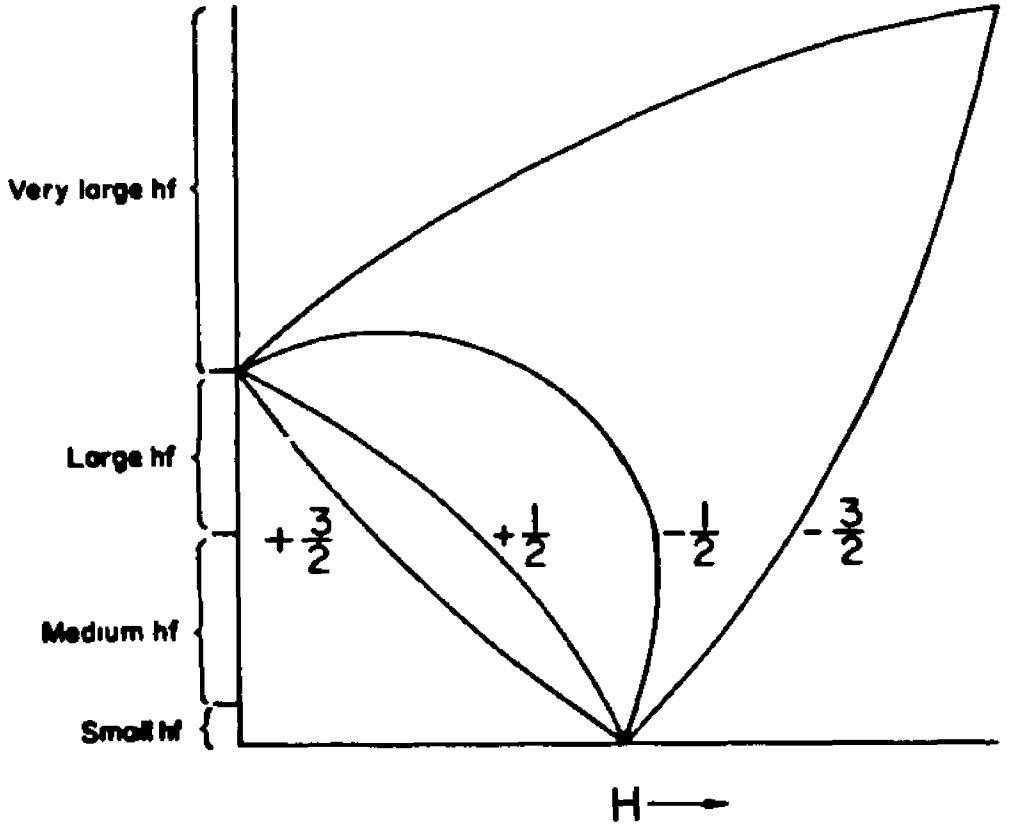

Fig. III.2 Zeeman Energy Level Diagram

Zeeman energy level diagram for a ^2S atom with I = 3/2. The states are labeled in both the uncoupled basis, $|S,M_S,I,M_I\rangle$, and the coupled basis, $|F,M_F\rangle$. Adapted from ref. (47).

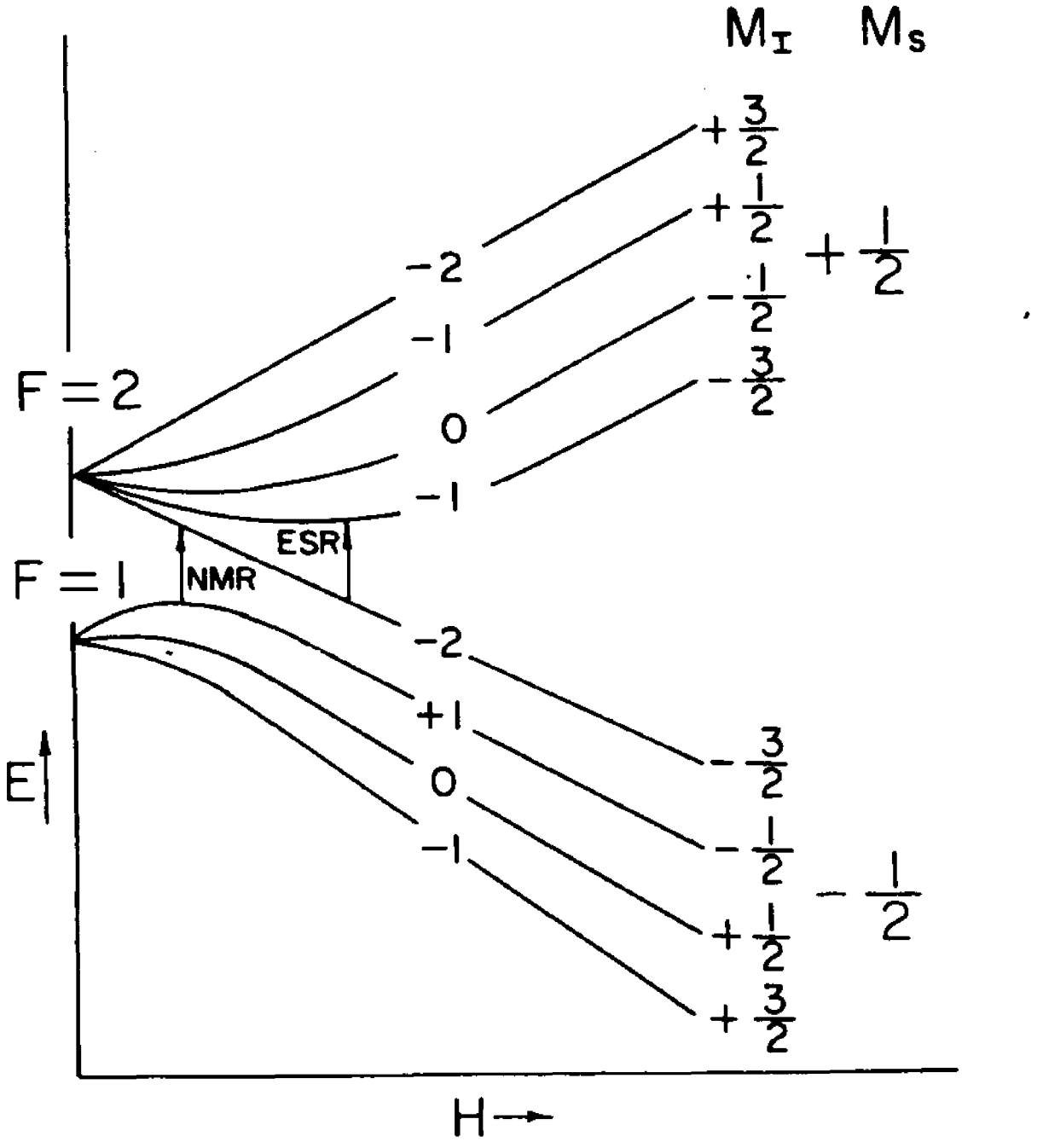

IV. SPECTRA AND ANALYSIS

IV.1. Introduction

Various uncontrollable factors already in existence in the laboratory will always influence or in some instances dictate the selection of experiments that one attempts to perform during one's graduate studies. In our case two factors could be isolated and credited for our experimental selections. The first was that at the time on going work with the group IB metals, i.e. Cu, and the individual that was performing these experiments was practically graduating. Thus the second factor, a new source successfully operating and most important, at my complete disposal. Still, the choice of metals were limited by the heat transfer considerations and vaporization limits of that source.

The work done on the group IB metals mostly focussed on the generation of homogeneous small metal clusters. This phase of the work was successful in some instances but we quickly found that these clusters could be generated, (or at least observed), in only one support matrix, nitrogen. To supplement the ESR experiments a UV-visible Optical Absorption apparatus, also in existence in the laboratory, was incorporated in the experimental detection scheme. This technique was mostly used for the silver work and in some instances corroborated previously published work, (67,70). From the results obtained, we further attempted to selectively generate metal clusters by optically exciting certain bands form the UV-visible spectra using a cutoff filter transparent only to the atom line positions, (67). Following this increasing interest in the group IB metal an attempt was made to generate heterogeneous or mixed-metal clusters of

groups IB-IA, (35,37), again taking advantage of the double chambered effusion source.

From the mixed-metal cluster generation experience, a series of experiments involving the groups IA-IIA metals followed. In all seven metal combinations were successfully generated in an argon matrix. Unfortunately, the OA method was not used in any of these experiments.

IV.2 Group IB Metal Clusters

The group IB metal clusters, Ag and Au, were generated in a nitrogen matrix at 4K. In all other support matrices, Ar, Kr and Xe, that were tried, only atom lines could be generated. These experiments only corroborated previously published observations, (16).

IV.2a. Silver Atoms

Spectra showing silver atoms in Ar, Kr, and Xe are shown in figs. (4.1-4.3) respectively. Two clearly resolved lines for each silver isotope with I = 1/2 are seen at low and high field for ^{109}Ag and ^{107}Ag respectively. Additional lines seen in the Ar, Kr, and Xe spectra were attributed to matrix side effects, and to the deposition substrate at g =2.

IV.2b. The Silver Trimer

Co-deposition of silver vapor with excess nitrogen gas resulted in the generation of spectra featuring a series of weak transitions at temperatures

close to 4.2K. Deposition time was approximately 3 to 4 hours with an N_2:Ag ratio of ~ 85:1. Upon annealing to ~25K, well resolved spectra, fig. (4.4), attributed to an axially symmetric trimer emerged. The spectrum showed two transitions at low and high fields respectively due to a single spin 1/2 nucleus with most of the unpaired spin. And, the remaining two equivalent nuclei with little or no spin, further split these two transitions into six parallel and six perpendicular components respectively. The axial symmetry of the spectrum implies that the trimer is rotating about one of it's principal axis. Unlike the group IA trimers, (17), there was no evidence of a pseudorotating specie.

Since the original work was performed with naturally abundant silver, ^{107}Ag and ^{109}Ag, 51.8% and 48.2%, respectively and a nuclear spin of I = 1/2 for both isomers, a series of isomers, i.e. $^{107}Ag_3$, $^{109}Ag_3$, $^{107}Ag_2{}^{109}Ag$, etc, were also observed. In all six isomers were assigned giving rise to 48 parallel and 48 perpendicular transitions at low and high field respectively, fig. (4.4). Except when overlapped by atomic transitions, the perpendicular transitions were well resolved.

To confirm the assignments and enhance the resolution of the weak parallel transitions, the experiment was conducted with isotopically enriched silver, ^{107}Ag, 99.9% pure. Fig. (4.5a) shows the axially symmetric $^{107}Ag_3$ in an N_2 matrix at 25K. The broad background about g = 2 is from the organic glue used to retain the optical window, (Chap. 3). Also observed, are transitions from a methyl radical, (71). Fig. (4.5b) shows the simulated spectrum of the trimer using the best fit magnetic parameters obtained and a simulation program labelled "1", (11). At 5.2K, the M= 0 perpendicular components are split by 1.5 and 3.0 G for m = ±1/2 respectively. This might

imply as in the case of Li_7 in Ar, (17), that the trimer is trapped in several matrix sites whose magnetic parameters show a small temperature dependence.

Well resolved spectra were obtained and facilitated the assignment of the trimer to a $^2A_1$ ground state in contrast to the $^2B_2$ ground state geometry assignment when generated in deuterobenzene, (73). The field positions are defined by eqs. (4.1), which are modifications of eq. (3.23) discussed in the previous chapter,

$$H_\perp = \left(\frac{g_e}{g_\perp}\right)[H_e - A_\perp M]\left(\frac{g_e}{g_\perp}\right)^2\left[\frac{A_\perp^2 + A_{//}^2}{4H_\perp}\right]\left[j(j+1) - M^2\right]$$
$$H_{//} = \left(\frac{g_e}{g_{//}}\right)[H_e - A_{//} M] - \left(\frac{g_e}{g_\perp}\right)^2\left[\frac{A_{//}^2}{2H_{//}}\right]\left[j(j+1) - M^2\right] \qquad (4.1)$$

The observed line positions of the isotopically enriched trimer in an N_2 matrix are listed in table (4.1), and are then compared with those calculated from a second order perturbation expansion program labelled "ESR 1" derived from eq. (4.1). The measured parallel and perpendicular g-values and hyperfine constants,[1] were the same for both the isotopically enriched and the naturally abundant silver trimer, and are listed in table (4.2). Finally, the assignment was confirmed by the ratio of the observed hf constants, $^{109}Ag/^{107}Ag$ = 1.154, (73), which was in good agreement with the

[1]From reference, (52), the sign of $A_{//}$ and $A_\perp$ cannot be identified by the use of eq. (4.1) alone. But, here we may assume that $A_{//}, A_\perp > 0$, in agreement with "the environment change rule of Schoemaker", (52). Indeed, in our case for the $^{107}Ag_3$ both $A_{//}$ and $A_\perp$ were positive.

predicted ratio of the nuclear moments, μ_{109}/μ_{107} = 1.1544, (74).

IV.2c. Heteronuclear Clusters: Ag and Na in an Ar Matrix

Our first attempt at generating mixed-metal clusters were unsuccessful. Fig, (4.6), shows the spectrum of Na-Ag in an Ar matrix. The spectrum shows only the atom lines of ^{107}Ag and Na. The less intense transitions were from Na_3. The line positions from both sets of atoms lines were the same as reported in previously cited references, (16,17).

IV.2d. Optical Absorption Spectra of Silver Clusters

UV-visible absorption spectroscopy has been used extensively in the past few years as one of the techniques for size determination of small metal clusters. Matrix isolated small metal clusters typically exhibit very intense UV-visible bands, and when coupled with ESR, can be an even more powerful detection and confirmation technique for elucidating cluster sizes. Silver matrices grown in Ar and N_2 support matrices were annealed to ~25K and irradiated with a high pressure Xe-Hg lamp for 5-10 minutes. Optical scans in the range of 200-600 nm were collected and are shown in figs. (4.7-4.8). A series of bands were observed and were assigned to Ag and $Ag_{n'}$ were $n \geq 2$. These bands were assigned as :

(i) Ag atom : three strong features around 298-314 nm and 309-327 nm in Ar and N2 respectively are observed and correspond to the Ag atom line $^2P_{3/2,1/2} \leftarrow ^2S_{1/2}$ transitions. The bands to the red have been assigned to the $^2P_{1/2} \leftarrow ^2S_{1/2}$ transition, and the doublets to the $^2P_{3/2} \leftarrow ^2P_{1/2}$ transition for

Ar and N_2 respectively.

(ii) Ag_2 : two bands were assigned to Ag_2 in Ar, the strong A-X transition around 440 nm, and at 260 nm a band corresponding to the B-X transition. Other weak bands were also observed but were not easily assigned to the Ag_2 system.

In an N_2 matrix a series of weak bands were observed towards the red but no assignments could be made.

(iii) Ag_3: only one band in N_2 matrix was assigned to the trimer at 402 nm. There is an additional weak band around 570 nm that was not assigned but might be due to the Ag_n, n>3, specie cited by Ozin et. al., (67). In Ar matrix, Ozin, (67), stated that the band at 440 nm assigned to the A-X transition of the dimer might also be part of the Ag_2/Ag_3 band, while Bechtold et al., (98), assigned a band at 443 nm to the dimer. Although Bechtold also assigned a system between 425 nm and 442 nm to the trimer in Xe support matrix, he could not unambiguously assign the trimer in Ar support matrix due to strong Ag_2/Ag_3 overlap. Thus due to inconclusive OA assignments and the absence of ESR spectra in argon support matrix , we concluded that this band most likely belongs to the silver dimer. Table (4.3) lists the band positions for all silver clusters observed in Ar and N_2 matrices along with positions cited by refs. (67, 83-84).

Selective cluster generation was attempted by using a cut-off filter transparent only to the silver atom transition at 315 nm during deposition. The ESR spectrum obtained showed the same trimer pattern only with lowered intensities and the OA spectrum showed the same number of bands with no significant band shifts or growth.

IV.3 Gold Atoms and Gold Clusters Isolated in an N_2 Matrix

Fig. (4.9) shows the spectrum of Au metal clusters generated in an N_2 matrix. The very intense four line transitions are those expected from a ^2S gold atom with I = 3/2. The spectrum also shows a series of transitions at low and high fields and was tentatively assigned to the gold trimer. The transition pattern suggest that a single atom, with I = 3/2, is carrying most of the spin, and is split into four components, m = ±3/2, ±1/2. Each transition should in tern split into seven lines due the interaction of the first atom with two additional atoms carrying little or no spin. This analysis is analogous to the one offered for Ag_3, (72), and Cu_3, (66), in an N_2 matrix. Due to anomalies and transitions overlap in this spectrum, definite assignment of the line positions could not confirmed. However, better agreement might be obtained between calculated and observed line positions if equation (3.23) is modified by adding a quadrupole term. The data and analysis of this system will be presented in a separate publication.

IV.4 Discussion

IV.4.1 Introduction

The axial spectrum of $^{107}Ag_3$ was previously shown in section IV.2b. Either the third order spin Hamiltonian or the Breit-Rabi equation could be used to calculate the hyperfine constants and the g-values. Then using a simple molecular orbital approach and the Jahn-Teller effect in conjunction with these spectral parameters, we were able to assign the ground state of the silver trimer. Furthermore, this assignment was compared with some sophisticated theoretical calculations, (34,77), and a recently published paper on the trimer isolated in deuterobenzene, (73).

The important physical properties of the trimer were all derived from the hyperfine constants and the g-values. The hyperfine constants provided the relative spin distributions or populations of the unpaired electron over each atom of the molecule. These spin populations are obtained by taking the ratio of the observed h.f. constants to the gas phase atomic value. Although this practice does introduce certain errors in the calculation, (e.g., factors such as orbital contractions, electron correlations and matrix effects, etc..), the use of the gas phase data does provide a consistent method for comparison of cluster properties. The g-values and the sign of the calculated g-shifts, indicated the hybridization scheme of the trimer. From this analysis, the molecular orbital diagram was constructed. The **g** and **A** tensor analysis leads to a better understanding of the rotational motion in the matrix and the probable rotational axis. This last fact shed more light on the puzzling observed axial symmetry of the spectrum.

Also, the observed OA spectra in Ar and N_2 support matrices, proved

to be an important addition to the assignment of these silver clusters. The spectral assignments and analysis follow closely previously cited references, (67-70).

This section will discuss, in the first part, the ESR of Ag_3 in a nitrogen support matrix, and the second part, the OA spectra of silver clusters, Ag_n, in Ar and N_2 support matrices.

IV.4.2 ESR of Ag_3

The Jahn-Teller effect has been used extensively to explain the different interactions of a triatomic molecule, such as Na_3, Li_3, (17), and Ag_3, composed of s orbitals. Fig. (4.11) shows the orbital correlation for such a molecule. The left side of the diagram shows the molecular orbitals for a linear or large angled geometry molecule. The energy of the states, $1a_1$ and $1b_2$, will converge and the orbitals will become degenerate as the angle is opened or closed to form the equilateral triangle or Jahn-Teller forbidden case. Further distortion of the angle will cause the high symmetry D_{3h} equilateral triangle to distort to the lower C_{2v} symmetry and form an acute or an obtuse angled isomer with $^2A_1$ and $^2B_2$ ground states respectively. More important experimental observations have shown that rapid interconversion between the equivalent geometries , ("pseudorotation"), is energetically feasible, (17). Intermediate between the three previous cases is the possibility of pseudorotation at a time scale comparable to the experiment time scale, giving rise to an alternating line width effect. These different molecular orbitals will show different ESR spectra thus providing information on the geometry of the trimer. The pseudorotating and

alternating line width effect were not observed in the case of the silver trimer, but have been reported by Lindsay et al., for the alkali metal trimers, (17). We can then illustrate the remaining two cases where :

i) case 1 : the acute angled isomer will have 2/3 of the spin density at it's apical atom and 1/6 on the two equivalent basal atoms. The expected spectrum should therefore show a pattern of 2 lines from the major interaction of the apical atom with the unpaired electron. These two lines will be further split into triplets by the remaining 2 basal atoms. This is exactly the spectral pattern shown in figs. (4.4-4.5). Therefore, this observation leads to the conclusion that we are indeed looking at the acute angle silver trimer with a $^2A_1$ ground state in nitrogen support matrix.

ii) case 2 : the obtuse angled isomer will have most of it's spin density at the two equivalent basal atoms and zero spin density at the remaining atom. The nodal apical atom, while having zero spin density at the simple Huckel level approximation, is expected to have a small spin density due to polarization effects. The predicted ground state of this isomer is $^2B_2$. The spectral pattern has not been seen in nitrogen support matrix, instead it has been observed for Ag_3 in deuterobenzene at 77K by Howard et al., (73). This ground state geometry has also been observed for the group IA trimers, (17).

This divergence in experimental behavior is not surprising since the predicted difference between the two geometries is only of the order of a few hundred wave numbers. Divergences in the ground state symmetries of certain molecules isolated in different matrices is not a new phenomenon as is the case of Ni in the gas phase and in Ar, Kr, and Xe matrices, (75,76). Thus, we can assume that the two support matrices N_2 and C_6D_6, can stabilize one isomer in preference to the other. This divergence in the

ground state assignment is also predicted by molecular structure calculations. Richtsmeier et al., (34), using a diatomics-in-molecule approach, predicted the acute angle isomer with $^2A_1$ ground state to be more stable, while Flad et al., (77), using the pseudopotential + density function, suggested that the $^2B_2$ ground state geometry should be more stable for the silver trimer.

If we assumed that the trimer is rotating about one of it's principal axis then the rotationally averaged **g** and **A** tensors will have axial symmetry. From the g-tensor analysis the symmetry of the trimer can be determined by rotating the **g** and **A** tensors about the trimer's molecular framework and then averaging each tensor element over all orientations. Fig. (4.10), illustrates the hybridization scheme for the partially occupied $2a_1$ orbital and the expected 5s and 5p character of the trimer. Here, (1), refers to the apical atom, and (2), (3), to the two basal atoms. This analysis also gives us the total anisotropy at the two basal atoms and an indication of the "hybridization" of the angle α on the two basal atoms, see fig. (4.10). These tensors can be expressed by eq. (4.2), using the sum of the Fermi contact and dipole-dipole terms, (60), $\mathbf{A(2)} = a(2)1 + T(2)$, where T(2) is given by,

$$T(2) = \beta(2)\begin{pmatrix} -1 & 0 & 0 \\ 0 & 3\cos 2\alpha - 1 & 3\sin\alpha\cos\alpha \\ 0 & 3\sin\alpha\cos\alpha & 3\sin 2\alpha - 1 \end{pmatrix} \qquad (4.2)$$

where $a(2)\,1 = \rho_{5p}(2)$ and $\beta(2) = \rho_{5p}(2) \times \beta_{5p}$ and α is the angle between the p orbitals of the two basal atoms and the molecular C_2 axis. A similar expression can be obtained for the third atom where Tyz = Tzy = -3 sin α cos α in equation (4.2).

The anisotropy on the apical atom can also be obtained with a similar equation where in this case , A(1) = a(1)1 + T(1). The anisotropy of the trimer is discussed in greater detail by Lindsay and Kasai, (81).

The terms in eq. (4.2) can then be expressed by the parallel and perpendicular hyperfine constants fo the $^{107}Ag_3$ as shown in table (4.4). In this case the angle $\alpha = 0^o$ for the apical atom. From column 4 in table (4.4), we see that the anisotropic parameters $A_{//} - A_{\perp}$, can be either positive or negative. But as shown in column 5, of table (4.4), the observed value was positive, $A_{//}(2) - A_{\perp}(2) = 3.4G$. This would imply that for the calculated value from the anisotropic spin population, $\beta 5p \sim 1.4G$, to satisfy the observed value of $A_{//}(2) - A_{\perp}(2) = 3.4G$, that the angle α, is close to either 0^o or 90^o. This indicates that the trimer is rotating about the molecular C_2 axis, which is the z axis in our framework. This phenomenon is also seen in the case of NO_2, (60,82), where it is easy to identify the axis of rotation. For the $^{107}Ag_3$ the axis of rotation is not easily identifiable because the three principal moments of inertia are almost equivalent, (60)[2] .

Using the hyperfine constants, $A_{//}$ and $A_{\perp}$, the isotropic hyperfine constant or Fermi contact term, a can be derived using eq. (4.3),

$$a = \frac{1}{3}(A_{//} + 2A_{\perp}) \qquad (4.3)$$

and is independent of any rotational axis. When the value of the Fermi contact term, a, is divided by the corresponding gas phase parameter, $^{107}a_{5s}$

[2] For $^{107}Ag_3$, the rotational constants are A= 0.050 cm^{-1}, B = 0.033 cm^{-1} and C = 0.020 cm^{-1} where A, B, and C correspond in fig. (4.7) to the x, y, z axes respectively, (60). For NO_2, A = 8.0 cm^{-1}, B = 0.43 cm^{-1}, and C = 0.41 cm^{-1}, table D-4, (60). Thus, for NO_2, A would most likely be the rotational axis.

= 611.1G, (77,78), the isotropic spin population $\rho_{5s}(1)$ on the apical atom and $\rho_{5s}(2)$ on the two basal atoms are then obtained. Table (4.5) lists the isotropic spin population for $^{107}Ag_3$ in an N_2 matrix along with values from two *ab initio* methods, (79,80). These values are in excellent agreement with one another and the ratio of $\rho_{5s}(1)/\rho_{5s}(2)$ is very close to the 4:1 ratio predicted by the simple Huckel model.

The anisotropic spin population is then obtained by using the formalism of eq (4.4),

$$\rho_{total} = \rho_{iso} + \rho_{aniso} = 1 \qquad (4.4)$$

Since the observed isotropic spin population, listed in table (4.5), was ρ_{5s} = 75%, the calculated anisotropic spin population using eq. (4.4), was ρ_{5p} = 12.5% on each of the two basal atoms. When multiplied by the anisotropic parameter for a $^{107}Ag_{5p}$ orbital, β_{5p} = 9.0G, (78), we get the anisotropic hyperfine value of a' ~ 1,4G, for each basal atom.

Using standard methods, (60,83), and g-values listed in table (4.2), the g-shifts, $\Delta g_{ii} = g_e - g_{ii}$, can be obtained. For the trimer both $\Delta g_{//}$ = - 0.0090 and $\Delta g_{\perp}$ = - 0.0465 were negative. We can assume from these large negative g-shifts that the anisotropy of the partially occupied $2a_1$ orbital of the trimer arises from spin-orbit coupling of the higher energy empty p-orbital with the s-orbitals rather than the lower energy filled d-manifold.

Even though the ESR results do not explain entirely the observed axial symmetry and the anisotropy of the silver trimer, it can be inferred that the wave function for the unpaired electron is mostly 5s at the apical atom and an equal admixture of 5s-5p at the two basal atoms. And, from the Jahn-Teller effect it is evident that the observed spectrum of Ag_3 shows the acute angled isomer with $^2A_1$ ground state in nitrogen support matrix.

IV.4.3 Optical Absorption Spectra

Two sets of bands assigned to the Ag atom were observed in both nitrogen and argon matrices. This is interpreted as a removal of the degeneracy by a crystal field causing the $^2P_{3/2}$ level to split into two sublevels, $^2P_{3/2\pm1/2}$ and $^2P_{1/2\pm3/2}$, where the second subscript correspond to the z component of the total angular momentum. This is the so called Kramer's degeneracy, which allows only doubly degenerate levels in system with one unpaired electron, (7). It is interesting to observe a red shift from N_2 to Ar matrix similar to earlier observations in Kr and Xe matrices, (67).

In the case of the dimer in Ar support matrix, the band assignments were in very good agreement with previous assignments, (67). The strong A-X transition towards the red and the weaker B-X transition towards the blue were clearly identified. The C-X transition although assigned by Ozin, (67), in the same region was not observed. Other features at 343 nm and 361 nm could not be conclusively assigned although Shin-Piaw et al., (95), reported observing a system between 315 and 363 nm in the emission band of Ag_2.

Two bands at 440 nm and 360 nm were assigned to the trimer in Ar support matrix. These assignments are in agreement with Ozin et al., (68), and Cheng et al., (99), who reported observing two systems between 360-380 nm, and 420-490 nm for trisilver clusters generated in a supersonic beam. Using photoexcitation in Kr and Xe support matrices, Ozin et al., (68), have reported observing a new band at 445 nm which they assigned to the Ag_3 system. They concluded that a photoisomerization process was responsible for this band growth. This feature could then be removed by annealing the matrix to 25K, where sufficient thermal energy could allow the matrix cage

to soften and cause back formation of the most stable silver trimer. Also, they reported not observing this band growth in Ar matrix in agreement with our observations. However these OA assignments in Ar support matrix are still questionable since we did not obtain any ESR spectra.

In a N_2 support matrix, a strong band at 402 nm was assigned to the trimer. Without other matrix deposition references or gas phase values, we used the trimer's detection by ESR as our strongest evidence of it's presence in this support matrix. Photoexcitation of the Ag atom line at 315 nm did not cause any changes in either the OA or the ESR spectra.

IV.5 Mixed-Metal Clusters of Groups IA-IIA Generated in Ar Support Matrix.

IV.5.1 Introduction

The generation of the mixed-metal clusters of groups IA-IIA was facilitated by the double chambered effusion source, (Chap. 2). The group IIA metals were chosen because their vaporization in the high temperature side of the source was quite stable and deposition rates could be satisfactorily controlled. Also, the low temperature side of the source, due to previously mentioned heat transfer considerations, limited our choices to only the alkali metals. This last choice was completely satisfactory since most of the ESR papers on alkali metal clusters were published by our laboratory, (17).

We knew that the analysis of the ESR spectra of these mixed-metal clusters would be severely limited since the group IIA metals are not paramagnetic. They all have an ns^2 or closed shell type electronic configurations. And, in terms of ESR theory, they would show no hyperfine values which would prevent cluster size assignments.

Besides work published by Kasai et. al., (35), on silver co-deposited with the IIA metals in argon support matrices, and work on the IIA metal hydrides and fluorides, (34,36-37), few references could be found dealing with the ESR of these heterogeneous species. From these references and our spectral observations we were able to explain our mixed-metal clusters using molecular orbital theory and by correlating observed magnetic parameters with other spectroscopic constants obtained form ref. (35). The line positions were calculated using eq. (3.24)

In this section, we will present the ESR spectra of the sodium, and the potassium atom along with spectra assigned to the mixed-metal clusters generated when these alkali metals where codeposited with the group IIA metals, i.e., Mg, Ca, Sr, and Ba, in argon support matrices. These mixed-metal species were labelled Na-IIA_n and K-IIA_n. Also, in every spectrum there were additional lines which were due to either the alkali metal trimer or septemer and methyl radical impurities. The assignments for these species were in close agreement with previously cited references, (17).

IV.5.2 Na-IIA_n in Ar Support Matrix.

i) $NaMg_n/Ar$

The spectrum of $NaMg_n$ in argon is shown in fig. (4.11). The intense four line pattern is due to a single Na atom with I = 3/2. The line assignments were in close agreement with the work published by Lindsay et. al, (17). The spectrum also shows a series of less intense quartets which were assigned to the mixed-metal species. As can be seen in fig. (4.11), these quartets are labelled I, II, and III. We believe that they arise from clusters of the form NaMg to $NaMg_n$, where $n \geq 1$. These spectra show an isotropic hyperfine character and have multiple matrix sites. Tables (4.6-4.7), list the line positions and the magnetic parameters of the Na atom and the mixed-metal clusters.

ii) $NaCa_n/Ar$

This spectrum is shown in fig. (4.12), again with the quartet Na atom transition. The other sets of transitions are believed to be the mixed-metal dimer NaCa. This spectrum shows an orthorombic hyperfine character and no multiple matrix sites. This observation was also reported by Kasai et. al., for AgCa in Ar, (35). All field positions and magnetic parameters are listed in tables (4.8-4.9).

iii) $NaSr_n/Ar$

The spectrum is shown is fig (4.13). Along with the Na atom lines, a single set of quartets is seen and was assigned to the mixed-metal specie labelled NaSr. This spectrum has an axial hyperfine character and no multiple matrix sites. The field positions and magnetic parameters are listed in tables (4.10-4.11).

iv) $NaBa_n/Ar$

Fig. (4.14) shows this spectrum with the intense Na atom line quartet. Two sets of quartets labelled I and II due to slightly different matrix sites were assigned to the mixed-metal specie NaBa. This spectrum shows an axial hyperfine character. Tables (4.12-4.13), list all line positions and magnetic parameters.

IV.5.3. K-IIA$_n$ in Ar Support Matrix.

i) KMg$_n$/Ar

Fig. (4.15) shows this spectrum with the intense quartet due to a single ^{39}K atom with I = 3/2. The less intense quartets were assigned to the mixed-metal species. These clusters are believed to range in size from KMg to KMg$_n$ with n ≥ 2. As previously observed with Na, co-deposition with Mg metal seems to generate more mixed-metal species than any other group IIA metal. This spectrum also has an isotropic hyperfine character. Tables (4.14-4.15) list all line positions and magnetic parameters.

ii) KCa$_n$/Ar

This mixed-metal co-deposition showed a couple of interesting features. Apart from the usual atom line quartet due to ^{39}K shown in fig. (4.16), another set of quartet, labelled II, was assigned to ^{41}K isomer also with I = 3/2, (17). The evidence offered for this assignment was that the observed relative line intensities of the two isotopes, ^{41}K/^{39}K = 0.7/9.9 = 0.071, were in good agreement with their natural abundances, 6.88%/93.10% = 0.073, (17, 60). The quartet labelled I was assigned to the mixed-metal cluster of ^{39}KMg. The last set labelled III, was due to a methyl radical impurity.

IV.6 Interpretation

The mixed-metal clusters presented in the previous section offer some interesting discussion. When sodium was co-deposited with the IIA metal, ESR spectra was observed for all of them, and multiple cluster formation observed only for NaMg codeposition. For potassium, the mixed-metal species could only be observed with Mg and Ca, again with multiple clusters formation with magnesium. To explain these observations, we propose that heterogeneous cluster formation and detection is dependent on both the size of the interacting atoms and the matrix support cage. Kasai, (35), reported that with the Ag-IIA mixed-metal clusters, unless UV-irradiation was conducted simultaneously with the metal co-deposition, the larger IIA mixed-metal clusters could not be observed. His explanation was that the heat produced by the irradiation eased cluster diffusion thru the matrix thus allowing their formation and detection. In our case, we annealed these matrices to ~25K but saw no spectral changes. We concluded that these mixed-metal clusters were formed on the surface layers of the support matrix, and once formed on the matrix could not be force to diffuse even by annealing. He also reported observing a gradual decrease in the mixed-metal silver hyperfine and a high field shift of the resonance positions with increasing IIA atomic size. We observed a similar trend with the IA-IIA mixed-metal clusters.

The group IIA metals all have an ns^2 electronic configuration and are therefore not paramagnetic. Fig. (4.17), shows the electronic energy diagram of both groups IA and IIA metals.

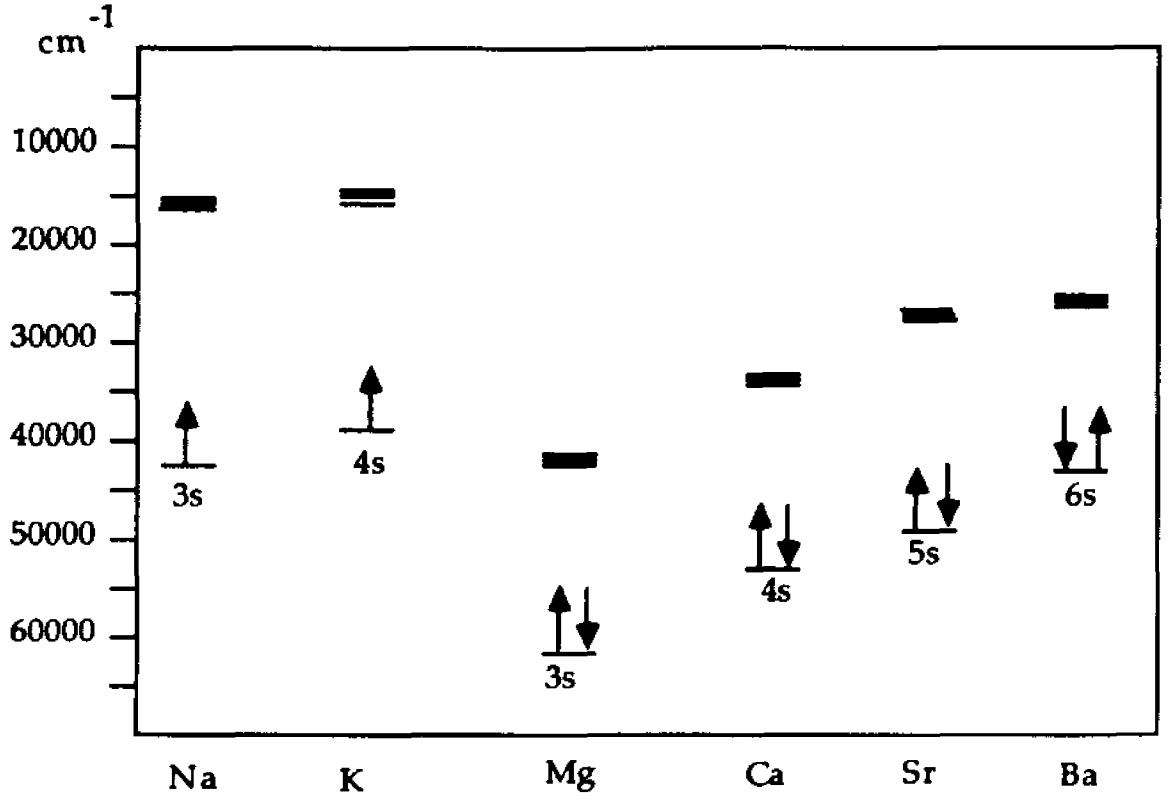

Fig.IV.17. Electronic orbital of the groups IA and IIA metals.

The smallest mixed-metal clusters formed will be dimers, and will share three electrons on two atoms. To illustrate this bonding scheme, we will take KMg as an example. From this simple scheme we concluded that the unpaired electron will reside in an antibonding σ^* orbital of the valence 4s orbital of the K and 3s orbital of Mg. This LCAO can be expressed by eq (4.5),

$$\Phi = a\phi_K\,(4s) - b\phi_{Mg}\,(3s) \qquad (4.5)$$

If we include the empty 3p orbitals of the magnesium atom, this hybridization scheme will further stabilize the dimer. A more accurate description of this interaction can be given by using a molecular orbital diagram, fig. (4.18),

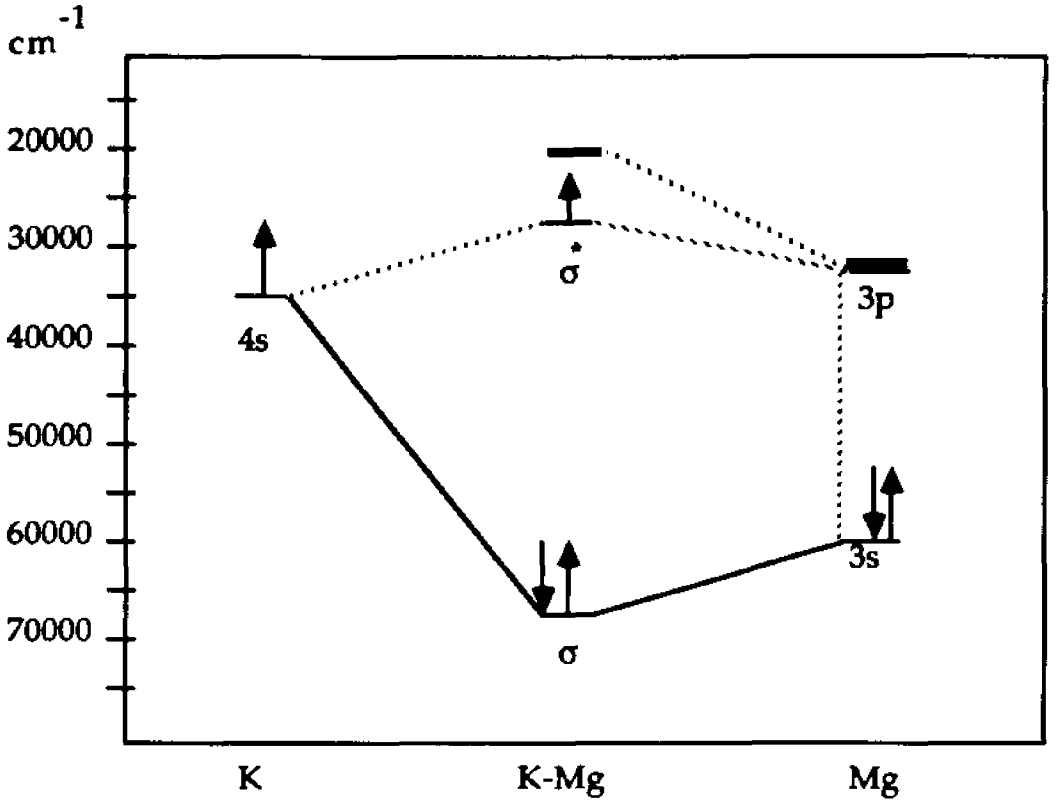

Fig. IV.18. Simple MO diagram of the KMg mixed-metal dimer.

Thus, we can now describe this interaction with a more accurate LCAO function,

$$\Phi = a\phi_K(4s) - b\phi_{Mg}(3s) - c\phi_{Mg}(3p) \qquad (4.6)$$

This would indicate the presence of anisotropy in the ESR spectra of these mixed-metal clusters. For KMg_n and $NaMg_n$ this was not observed. Even though we assigned their spectra as having mostly isotropic hyperfine characters, we cannot rule out the fact that the multiple matrix sites observed in the spectra may or may not be due to the presence of anisotropy. Kasai, (35), in his work with silver and the group IIA metals calculated the anisotropy contribution from both the **g** and **A** tensors of the silver. For the alkali metals the anisotropy contribution will be present only in the **g**

tensors. These observations will be presented in a subsequent paragraph. However, for the remaining group IA-IIA mixed-metal clusters, due to greater spin-orbit interaction, the anisotropy will be present in both **g** and **A** tensors. This can be seen in the axial or orthorombic hyperfine characters of their ESR spectra. To obtain the anisotropy contributions a complete analysis of both tensors would have to be undertaken. In this case eq. (4.1) instead of eq. (3.24) may be more suitable. These analyses and spectral line shapes will be presented in a separate publication.

Knight et. al., (34), reported the ESR of the IIA metal hydrides and concluded that significant s→p hybridization was involved on the alkaline earth atom during the formation of these dimers. A similar approach was taken by Chan et. al., (94), in their theoretical study of BeH and MgH. They concluded from their calculations that for MgH the 3s and 3p orbitals of Mg was of paramount importance to the formation of the dimer. The absorption of KMg, formed in the excited state, was also studied by Barat and Benard, (90-92), using chemiluminescence and laser fluorescence spectroscopy. Barat, concluded that in the excited state Mg would be in the (^{3}P) state, which would be identical to an alkali metal half filled s-shell. The molecular configuration of the dimer would then be, K (4s) and Mg (^{3}P) and this mixed dimer might have a chemical binding similar to an alkali dimer. Kappes et. al., (93), using supersonic molecular beam generation techniques and photoionization mass spectroscopy, reported that the dimer was observed with a relatively low abundance. But, in contrast to our observations, they reported that the Mg atom changes from a van der Waals interacting particle to a strongly bonding one between K_5Mg and K_6Mg.

This simple MO picture was also substantiated by the g-shifts analysis. Except for $NaBa_n$, all the g-shifts were negative or close to zero. We concluded that indeed the ns orbital of the alkali metals was mixing with the empty np orbitals on the group IIA metals. Since the g-shifts were positive for the NaBa mixed-metal clusters, we believe that the hybridization may involve the lower empty 5d orbitals instead of the 6p orbitals on Ba. For the remaining group IIA metals, the extent of that mixing can be seen as we move from $NaMg_n$ down the period to $NaSr_n$. Fig. (4.21) shows the correlation of Δg vs. the one electron spin-orbit coupling constant, λ, of the IIA atoms, (35).

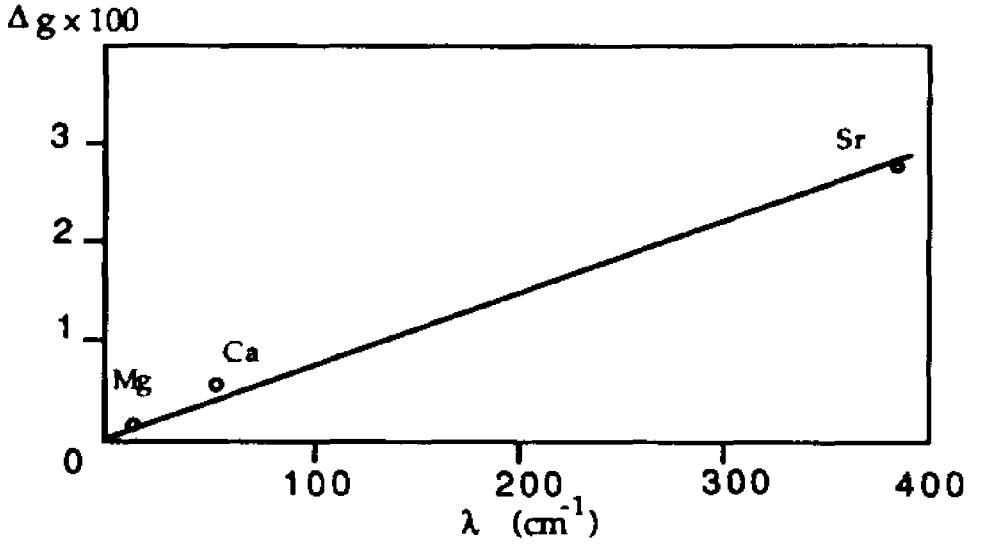

Fig. IV.19. The correlation between the observed Δg of Na-IIAn and the one-electron spin-orbit coupling constant of the group IIA atoms.

There is linear dependency between λ and the Δg values. As shown in fig. (4.19), the g-shifts are increasing with increasing spin-orbit coupling constant. This dependency, was also observed by Kasai, (35), and by Knight, (37), for the group IIA metals with Ag and hydrogen respectively.

This simple MO picture is greatly complicated as we move to larger sized clusters. But before we attempt to build MO diagrams for these clusters, we should elaborate on their aggregation mechanism. Again, this is a very complicated process and only a simplified version can be given. We assume that when the two metal beams collide with the matrix surface, the atoms may move and interact with each other before becoming completely embedded in the matrix. Then, the size of the individual atoms and the matrix cage determines the extend of cluster diffusion. To explain these interactions, we have proposed two reaction routes. We can picture the successive addition of the group IIA atoms to the alkali atom or an already formed mixed-metal cluster i.e., the dimer. This is shown in route i,

i) $K + Mg \rightarrow KMg$

$KMg + Mg \rightarrow KMg_2$

$Mg + KMg_2 \rightarrow KMg_3$

The second route is the addition of the group IA metal to the mixed-metal dimer,

ii) $K + Mg \rightarrow KMg$

$KMg + K \rightarrow K_2Mg$

$K_2Mg + K \rightarrow K_3Mg$

The first aggregation route seem to be one followed in our experiments as evidence by the ESR spectra, while the second route was the one observed by Kappes, (93). An explanation for the spectral evidence of proposed route i, cannot be given at this point. However, the fact that larger sized mixed-metal clusters were observed only with magnesium co-deposition, can be tentatively explained. Chiles and Bauschlicher, (96,97), using SCF and SCEP respectively calculated the bonding scheme for the alkaline earth metal

clusters. From their calculations, they concluded that Mg_2, Mg_4 and Ca_4, would be weakly bound as compared to Be_2 and Be_4. They attributed the difference in the bonding between Be, Mg and Ca to the extent of s→p hybridization. For Be, the 2s→2p hybridization was greater than the 3s→3p and 4s→4p on Mg and Ca respectively. And, they also reported that eventhough the Ca 4s→4p hybrid bond is more diffuse that the Mg 3s→3p hybrid bond, the promotion energy was 30% less for Ca. They concluded that for Ca, the two effects may have canceled each other out resulting in the similarity between the bonding of Mg and Ca. Thus, for our Mg mixed-metal clusters, we propose that the addition of the alkali atom may have lowered their energies enough to induce cluster stabilization. However, for Ca, along with Sr and Ba, although this addition may have caused a similar effect, we think that the interaction between metal size and deposition matrix cage may have prevented their formation.

The ESR analysis of the mixed-metal clusters of the groups IA-IIA metals presented in the previous sections were inconclusive for a number of reasons. Obviously, due to the electronic configuration of the IIA metals, were not able to obtain hyperfine values from the IIA metals. Because of this problem, we could not determine the sizes of these clusters. However, we were able to present a simple MO picture for the smallest mixed-metal cluster which would be a dimer. We explained the bonding scheme of this dimer using a couple of LCAO equations, and substantiated our conclusions with spectral observations. Finally, An explanation was also attained by the g-tensor analysis. A series of trends was established when the g-shifts were plotted against the spin-orbit coupling constants for the IIA metals. The most important information obtained from this plot was that the line went

through the origin, substantiating the fact that the anisotropy contribution was from the IIA metals, (35). Also, for Na-Ba the g-shifts were positive indicating a different hybridization scheme compared to the rest of the group IIA metals.

Multiple cluster formation was observed for only IA-Mg co-deposition, and for K-IIA co-deposition only Mg and Ca mixed-metal clusters were observed. Our proposed explanation was that, mixed-metal cluster formation is dependent of both the size of the interacting atoms and the support matrix cage. We also proposed an aggregation scheme that seems to agree well with the ESR spectra. However, the lack of experimental references and theoretical calculations prevented any decisive conclusions on the size distribution observed in their ESR spectra.

Fig. IV.1. ESR Spectrum of Silver Atoms in an Argon Matrix.

The ESR spectrum of ^{109}Ag and ^{107}Ag atoms isolated in an Ar matrix at 4K. The overall scan was 800 Gauss wide and centered about g = 2.

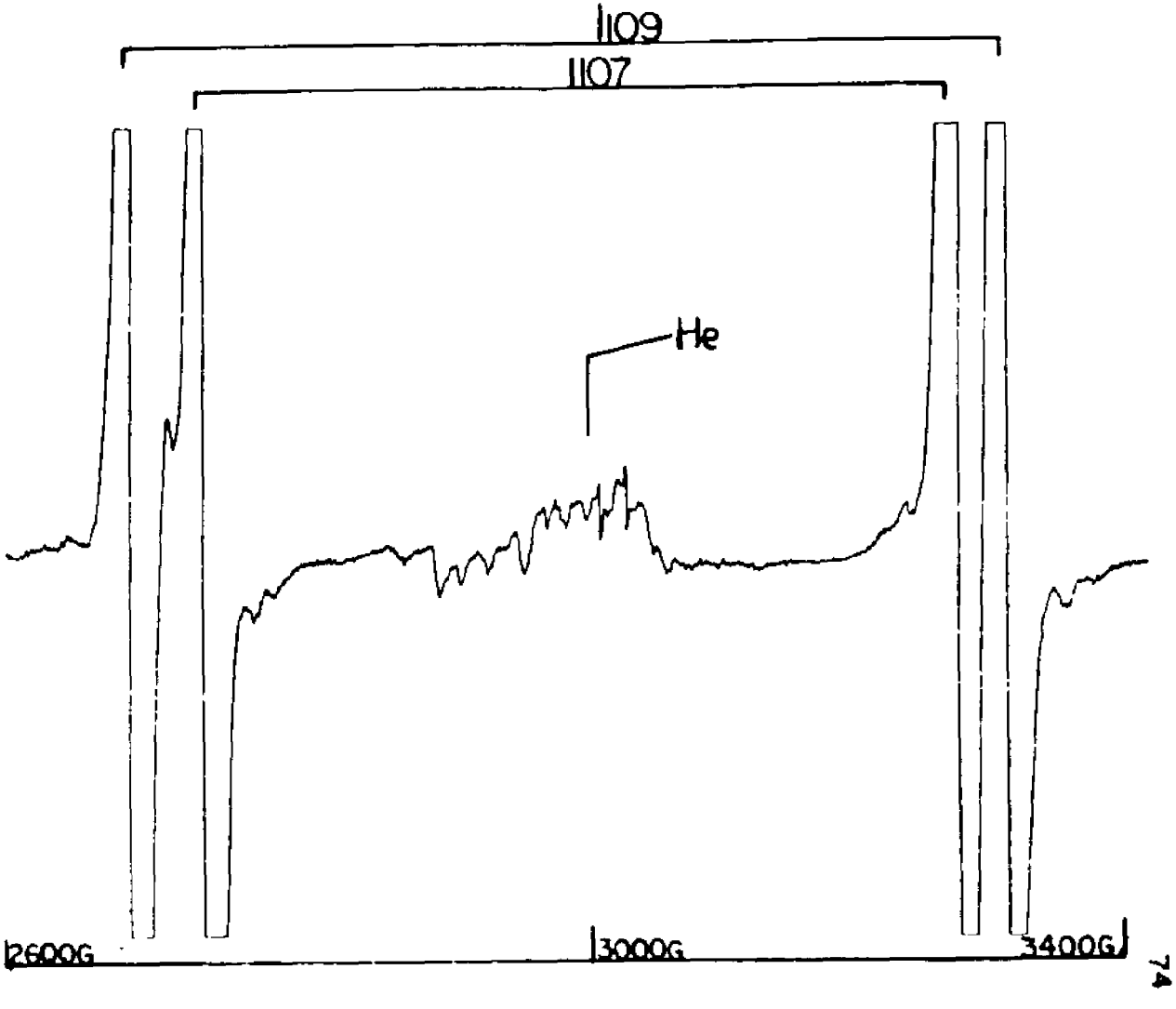
1109
1107
He
2600G
3000G
3400G

Fig. IV.2. ESR Spectrum of Silver Atoms in a Krypton Matrix.

The ESR spectrum of ^{109}Ag and ^{107}Ag atoms isolated in a Kr matrix at 4K. The overall scan was 800 Gauss wide and centered about g = 2.

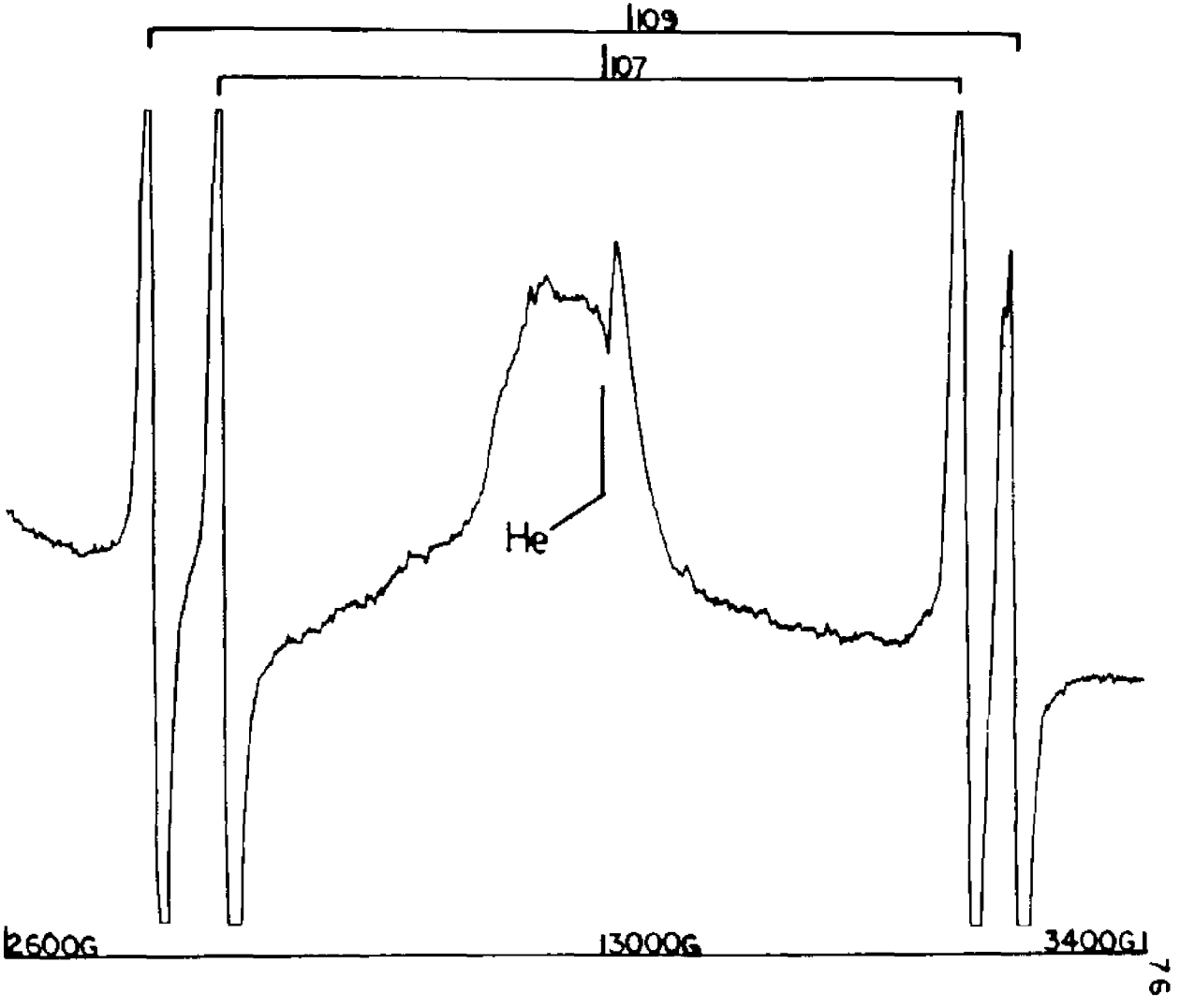
109
107
He
2600G
13000G
3400G
76

Fig. IV.3. ESR Spectrum of Silver Atoms in a Xenon Matrix.

The ESR spectrum of ^{109}Ag and ^{107}Ag atoms isolated in a Xe matrix at 4K. The overall scan was 1000 Gauss wide and centered about g = 2.

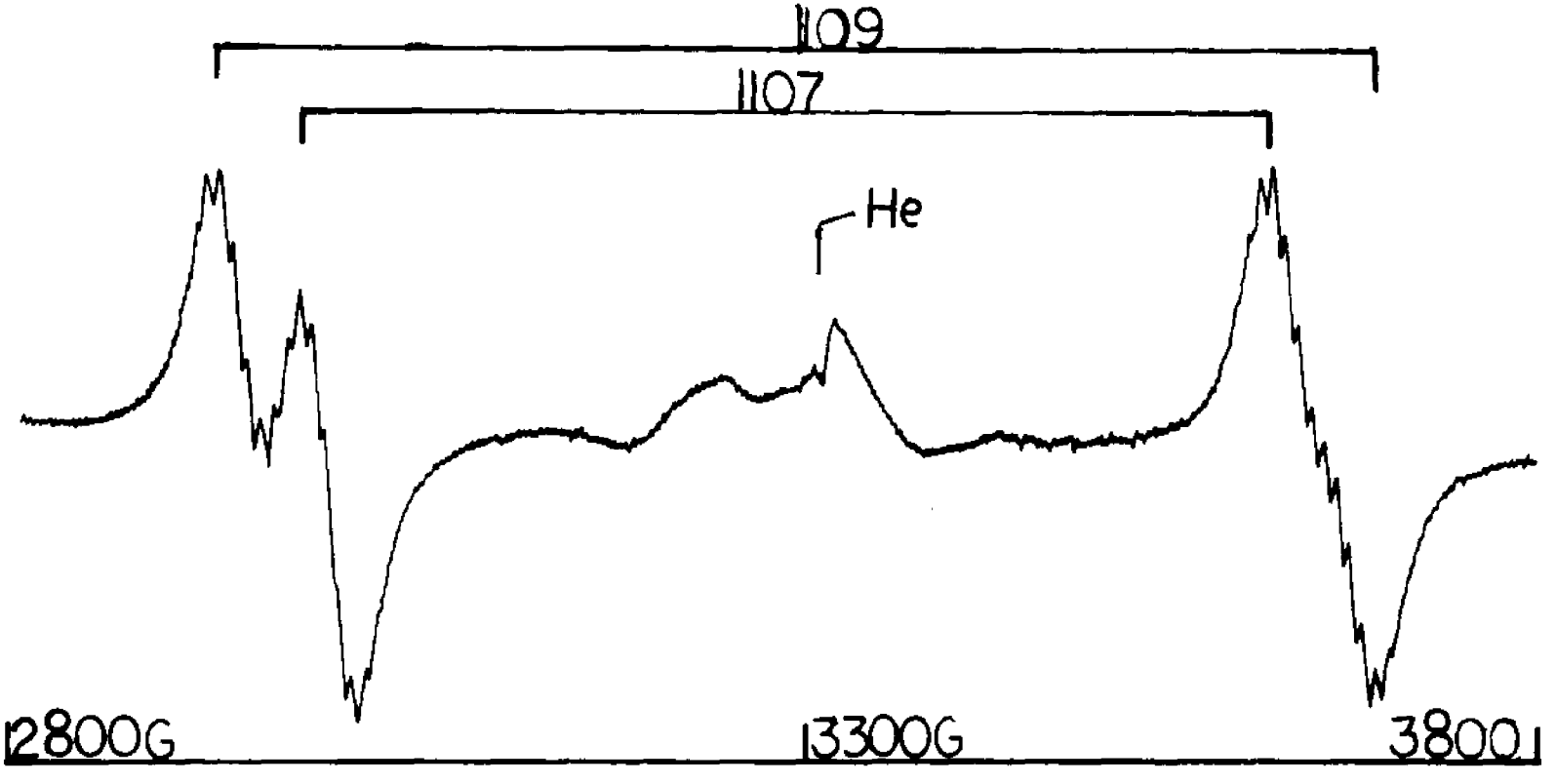
1109
1107
He
2800G
3300G
3800G

Fig. IV.4. ESR Spectrum of Naturally Abundant Ag_3 in a Nitrogen Matrix.

The ESR spectrum of naturally abundant Ag_3 in an N_2 matrix. Two sets of transitions corresponding to the silver atoms, ^{109}Ag and ^{107}Ag, are shown. Also, 48 parallel and 48 perpendicular transitions were assigned to the combinations of $^{109\text{-}107}Ag_3$. The overall scan was 700 Gauss wide and centered about g = 2.

ESR SPECTRA OF MIXED SILVER TRIMERS $^{107}Ag_n{}^{109}Ag_{3-n}$

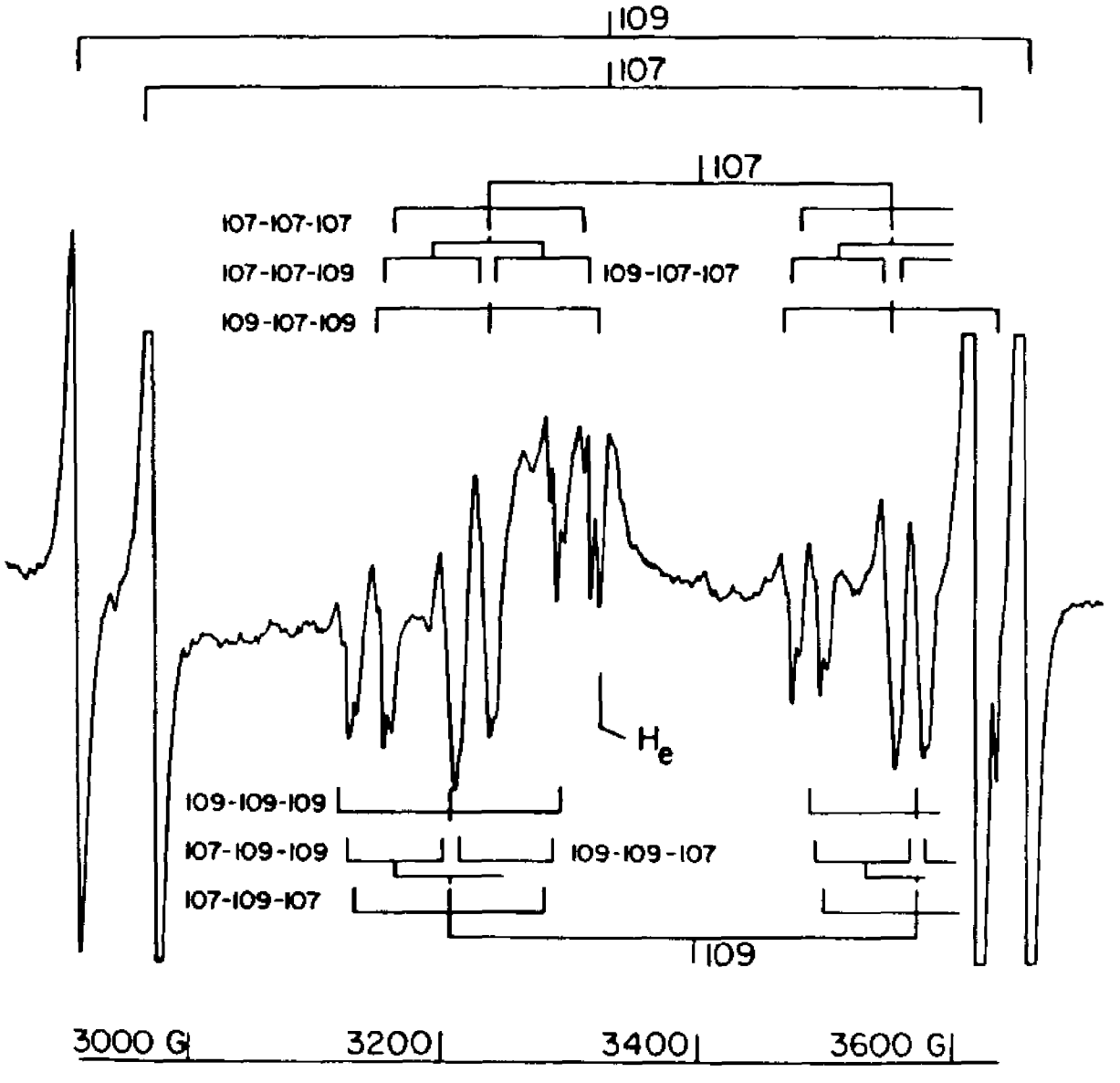

Fig. IV.5. ESR Spectrum of $^{107}Ag_3$ in a Nitrogen Matrix.

The ESR spectrum of isotopically pure $^{107}Ag_3$ in an N_2 matrix. Two sets of transitions corresponding to the silver atoms, ^{107}Ag, at low and high field respectively are shown. Also, a set of triplets were observed and were assigned to the $^{107}Ag_3$. Spectrum b, shows a simulation of the trimer using the best fit parameters. The overall scan was 700 Gauss wide and centered about g = 2.

ESR SPECTRUM OF $^{107}Ag_3$ IN AN N_2 MATRIX

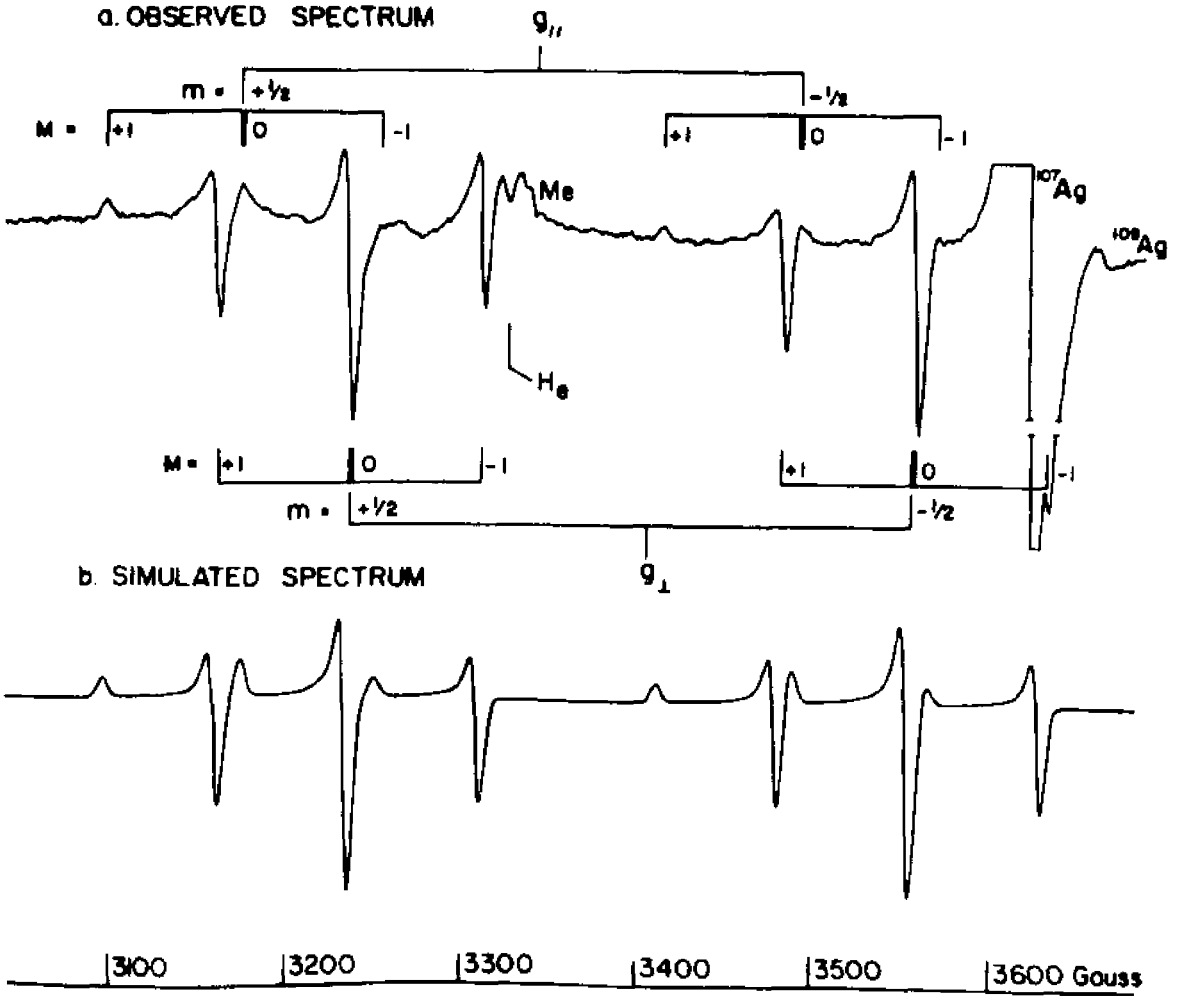

Fig. IV.6. ESR Spectrum of NaAg in an Argon Matrix.

The spectrum shows two ^{107}Ag atom line transitions and the four line pattern for an Na atom with I = 3/2, (17). In addition, there were transitions present that were assigned to the sodium trimer, (17). The overall scan was 1200 Gauss wide and centered about g = 2.

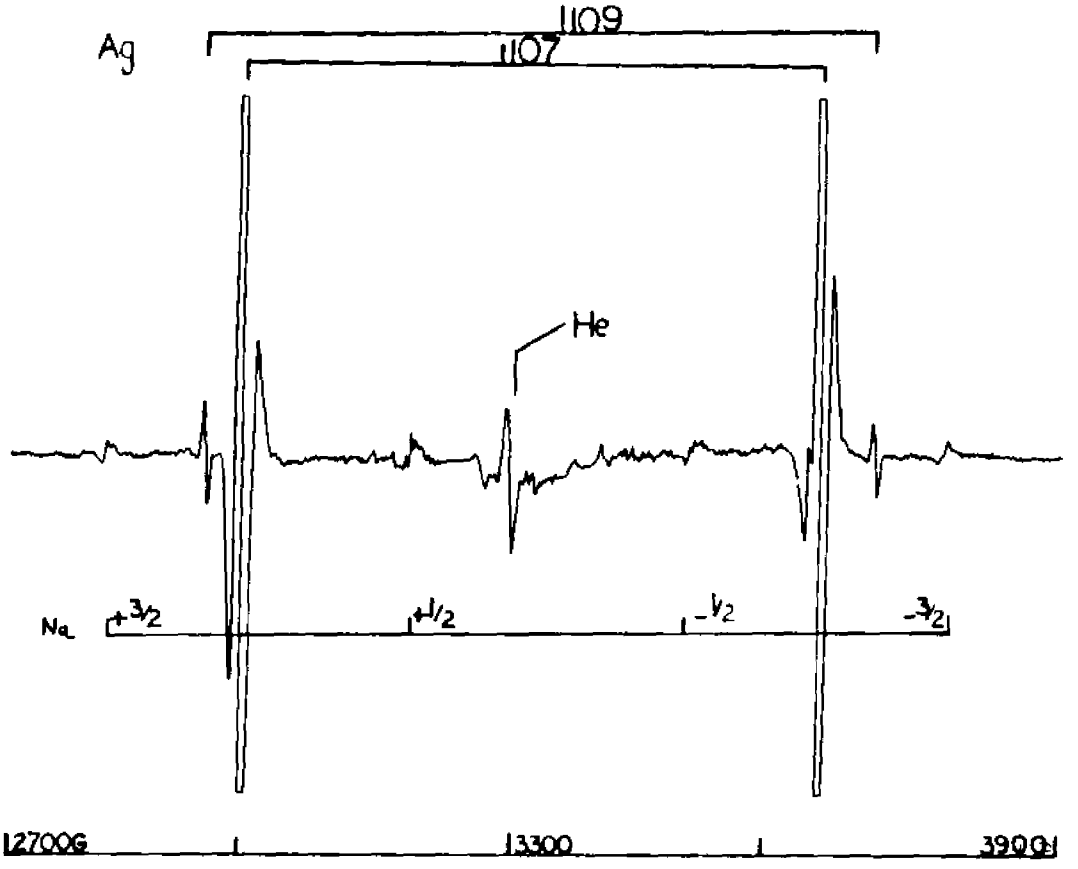
Ag
1109
1107
He
Na
+3/2
+1/2
-1/2
-3/2
12700G
13300
13900G

Fig.IV.7.Optical Absorption Spectrum of ^{107}Ag in an Argon Matrix.

OA spectrum of ^{107}Ag in an argon support matrix at 25 K. Several bands were assigned to the Ag atom, the dimer and the trimer. For the remaining bands, no conclusive assignements could be made. The overall scan was from 2000 to 6000 A^{o}.

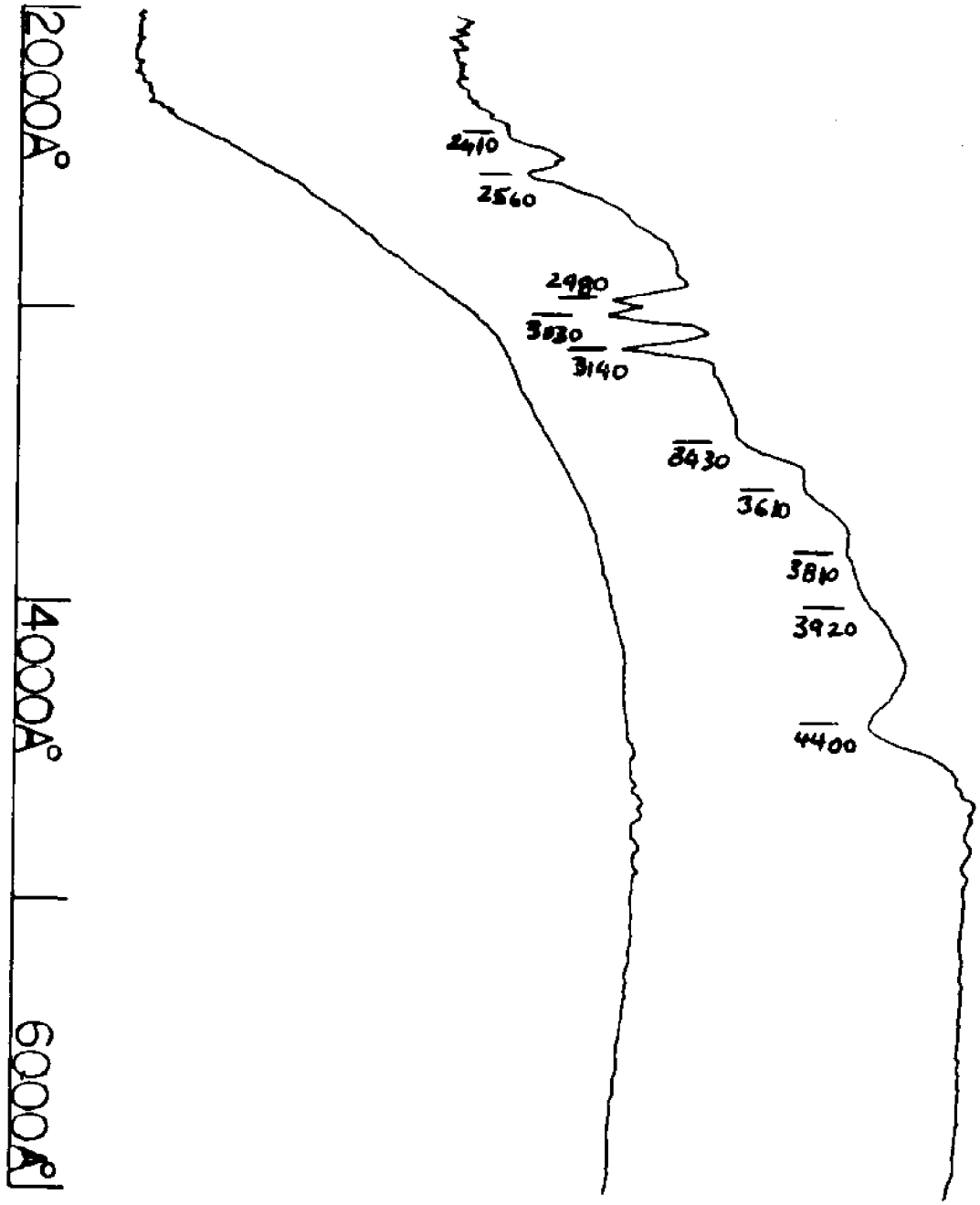
2000A°
4000A°
6000A°
2410
2560
2980
3030
3140
3430
3610
3810
3920
4400

Fig.IV.8.Optical Absorption Spectrum of ^{107}Ag in a Nitrogen Matrix.

OA spectrum of ^{107}Ag in an argon support matrix at 25 K. Three bands to the silver atom and the remaining bands to the trimer. The overall scan was from 2000 to 6000 A^{o}.

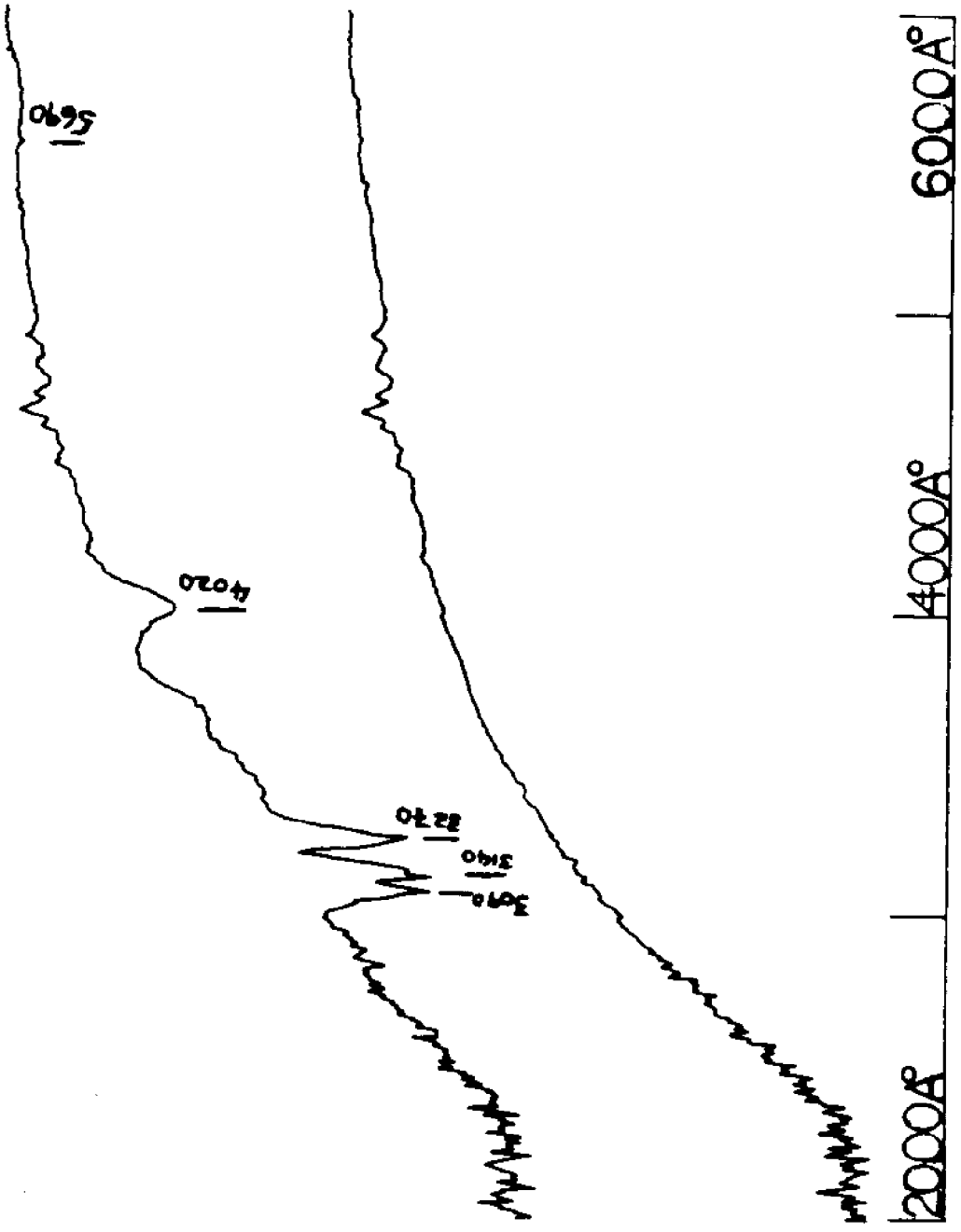
2000A°
4000A°
6000A°
5690
4020
3709
3440
3210

Fig. IV.9. ESR Spectrum of Gold Atoms in a Nitrogen Matrix.

The ESR spectrum of gold atoms isolated in an N_2 Matrix at 4.2 K. In this spectrum a series of transitions were also seen and were believed to originate from a specie labelled "Au_3". The overall scan was 4000 Gauss wide and centered about g = 2.

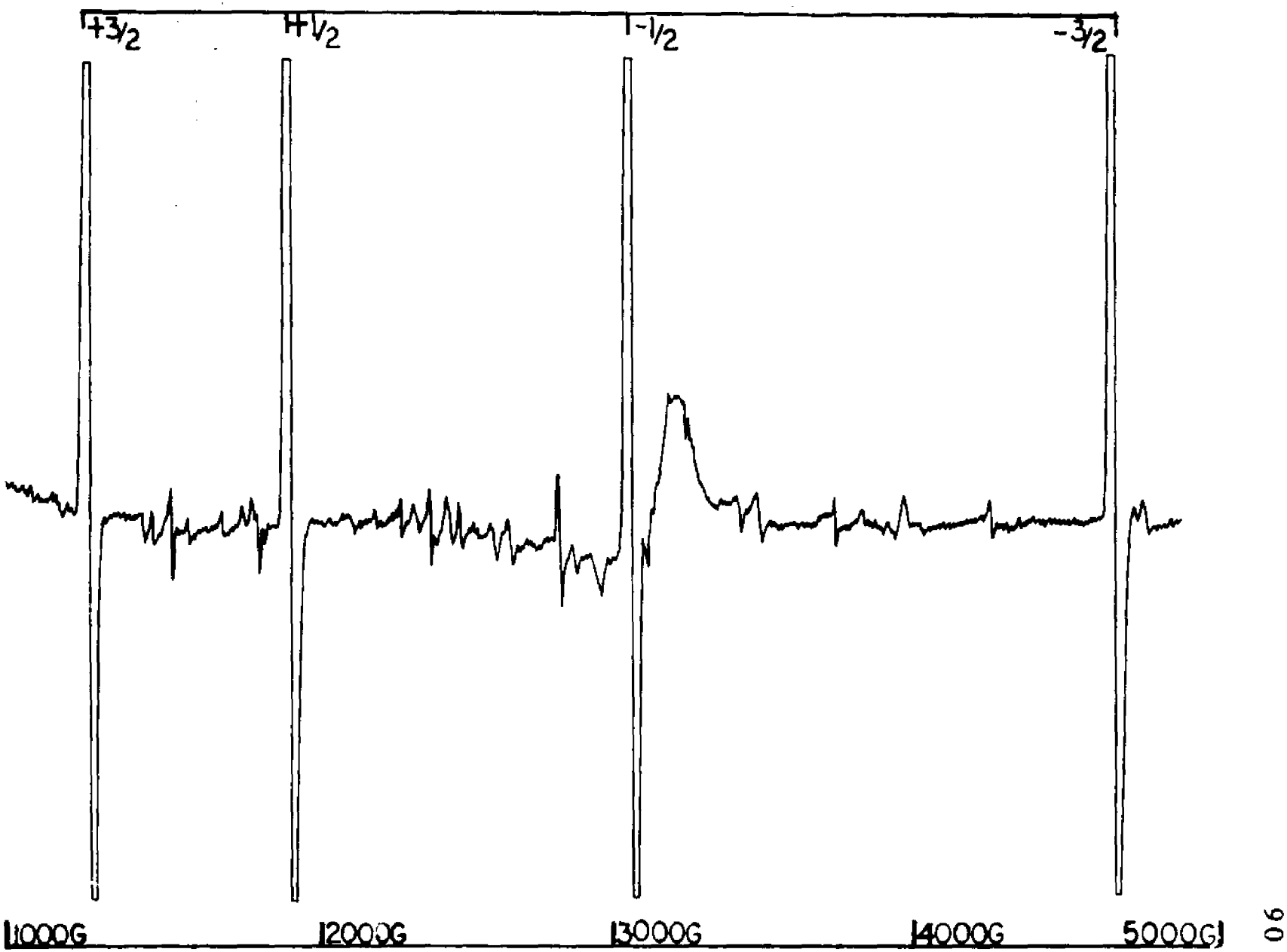
+3/2
+1/2
-1/2
-3/2
11000G
12000G
13000G
14000G
15000G

Fig. IV.10. Qualitative Molecular Orbital Scheme for the Partially Occupied $2a_1$ Orbital of Ag_3.

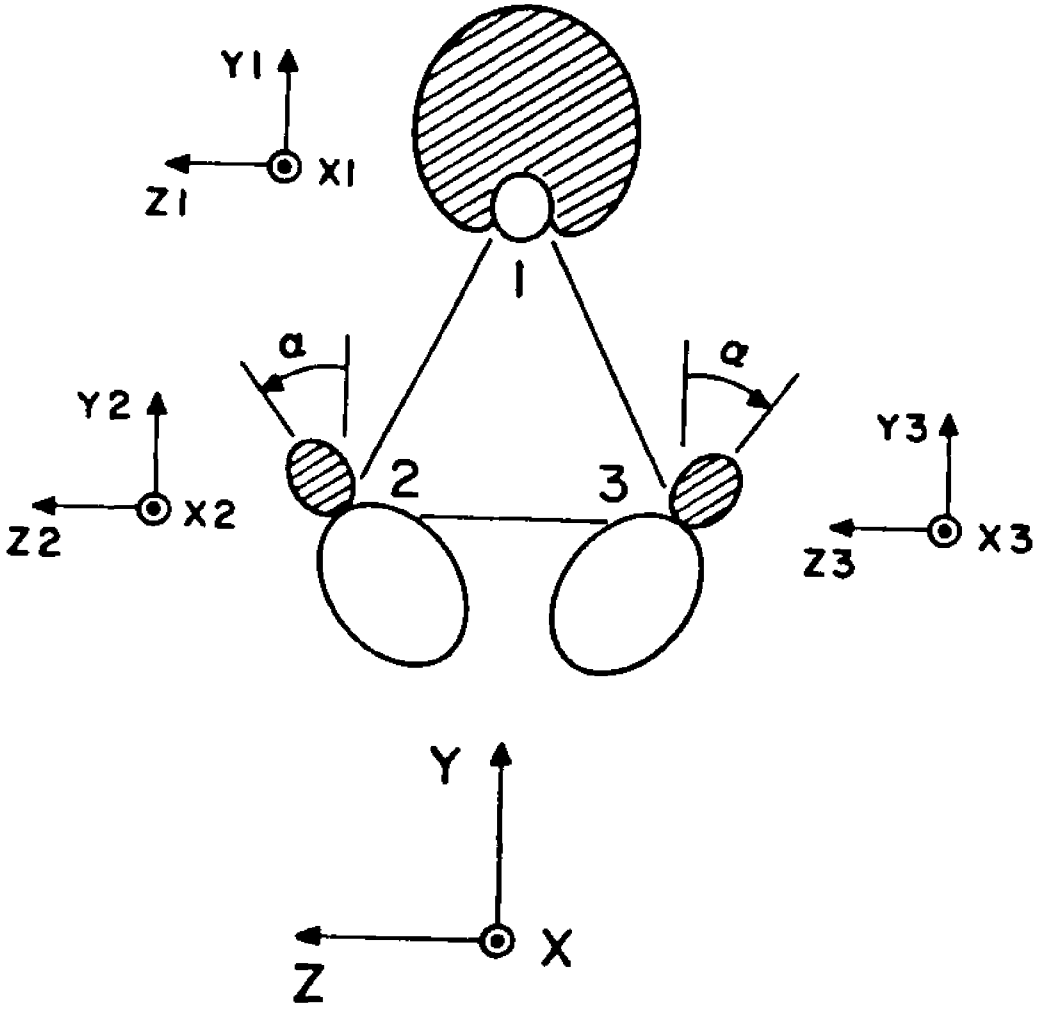

$$|2a_1\rangle = -a_{11}\,|P_{y1}\rangle - a_{12}\,\{\cos\alpha\,[|P_{y2}\rangle + |P_{y3}\rangle] + \sin\alpha\,[|P_{z2}\rangle - |P_{z3}\rangle]\}$$

Fig. IV.11. ESR Spectrum of NaMg in an Argon Matrix.

The ESR spectrum of the mixed-metal clusters of NaMg in an argon matrix at 4K. The transitions labelled A and A' were from the Na atom, and the series of unassigned transitions arise from Na_3, (17). The remaining transitions were assigned to the mixed clusters and are labelled I, I', II, and III. The overall scan was 1200 Gauss wide and centered about g = 2.

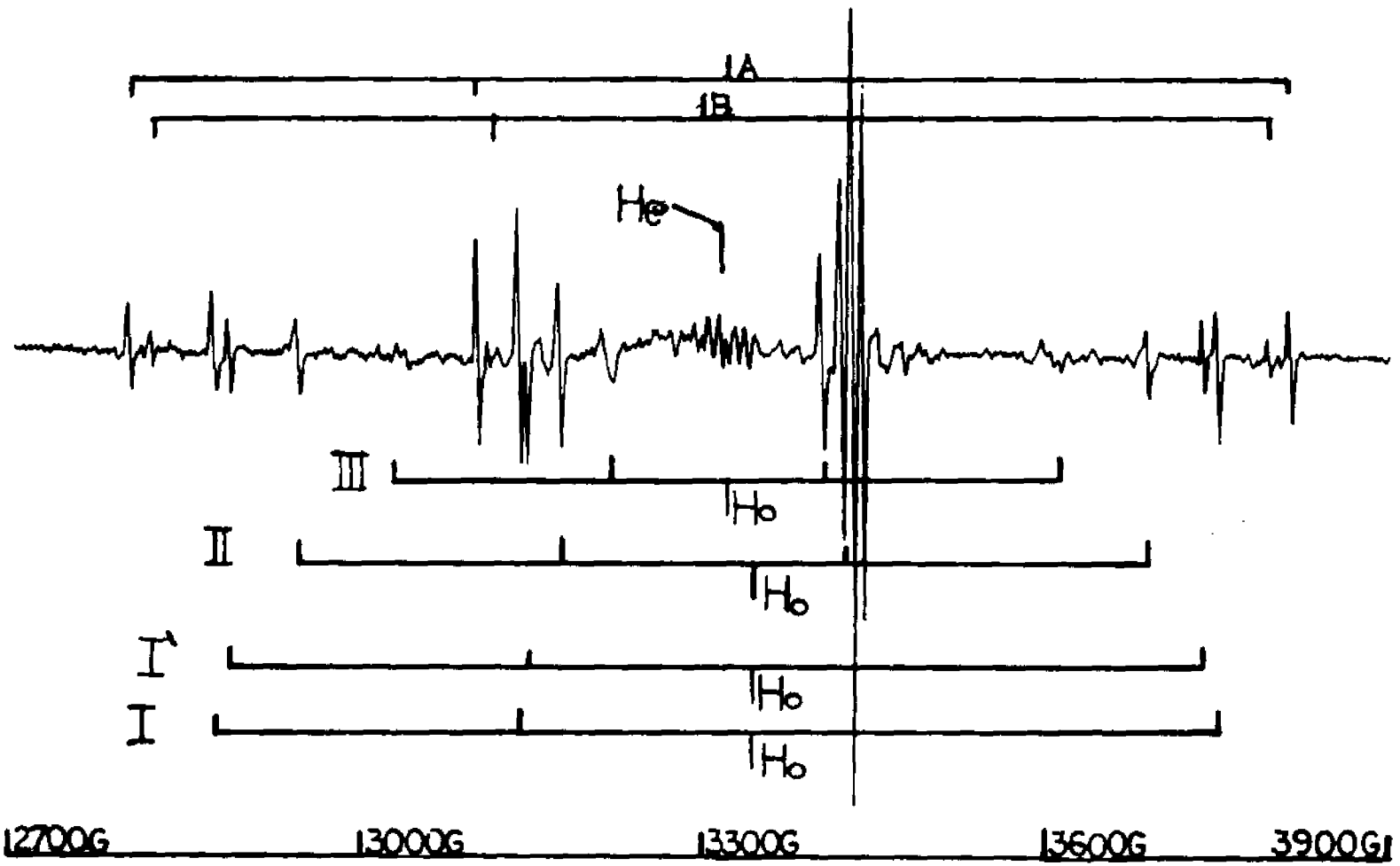
1A
1B
He
III
Ho
II
Ho
I'
Ho
I
Ho
12700G
13000G
13300G
13600G
13900G

Fig. IV.12. ESR Spectrum of NaCa in an Argon Matrix.

The ESR spectrum of the mixed-metal clusters of NaCa in an argon matrix at 4K. The transitions labelled A, A' and A" were from the Na atom transitions, (17). The transitions assigned to the mixed clusters and are labelled I. The remaining transitions present in the spectrum were from Na_3, (17). The overall scan was 1200 Gauss wide and centered about g = 2.

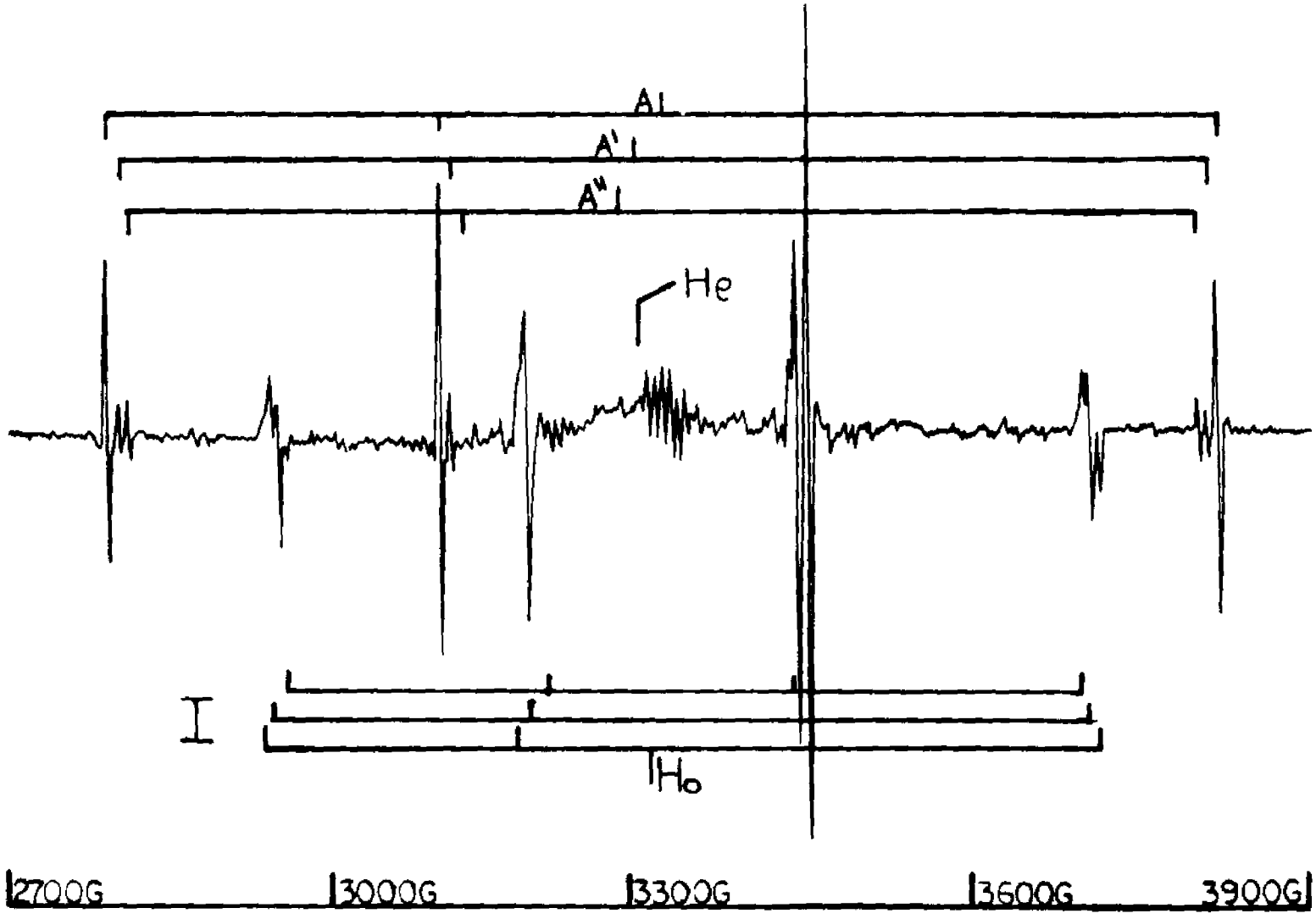
A
A'
A"
He
I
Ho
2700G
3000G
3300G
3600G
3900G

Fig. IV.13. ESR Spectrum of NaSr in an Argon Matrix.

The ESR spectrum of the mixed-metal clusters of NaSr in an argon matrix at 4K. The transitions labelled A, and A' were from the Na atom transitions, (17). Only one transition was assigned to the mixed clusters was labelled I. The remaining transitions present in the spectrum were from Na_3, (17). The overall scan was 1200 Gauss wide and centered about g = 2.

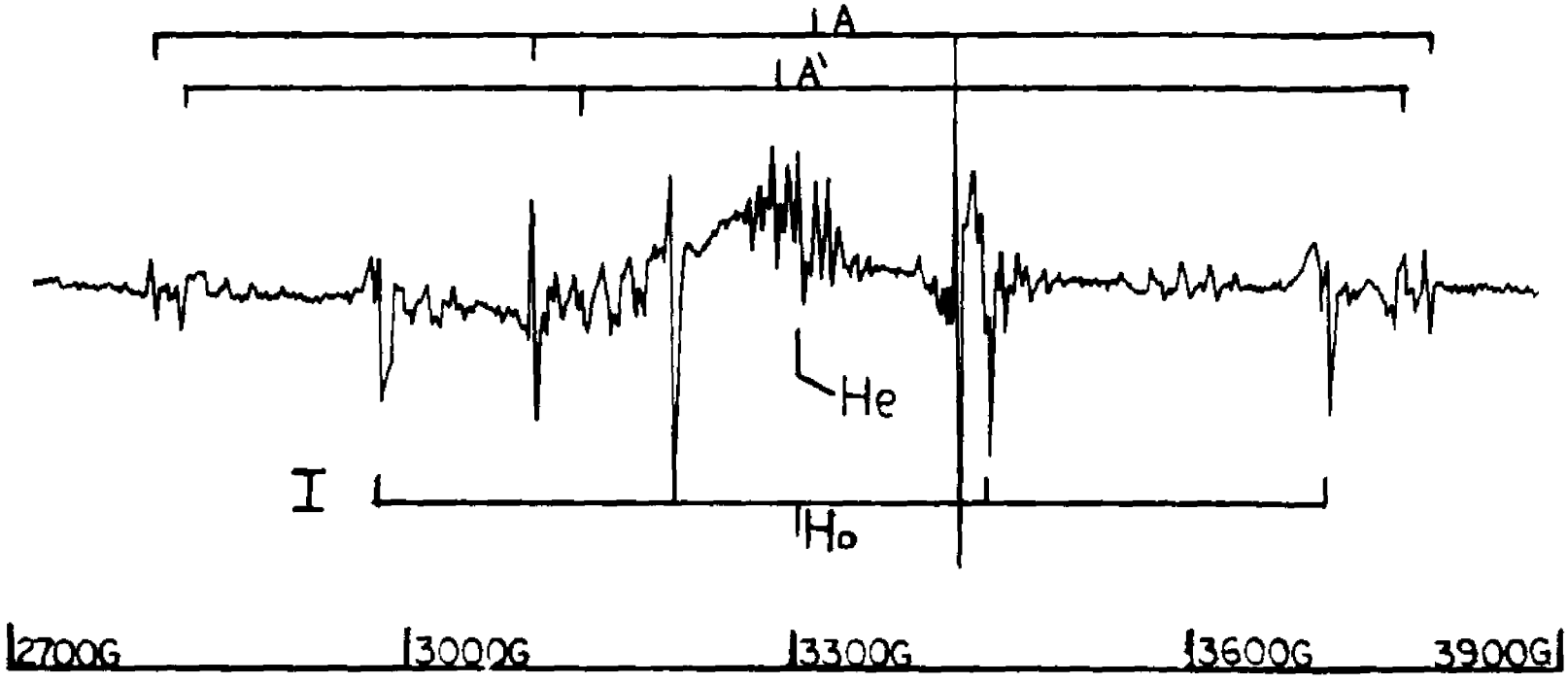
A
A'
He
I
Ho
2700G
3000G
3300G
3600G
3900G

Fig. IV.14. ESR Spectrum of NaBa in an Argon Matrix.

The ESR spectrum of the mixed-metal clusters of NaBa in an argon matrix at 4K. The transitions labelled A, and A' were from the Na atom transitions, (17), along with a series of transitions arising form Na_3, (17). The remaining transitions were assigned to the mixed clusters and were labelled I, II, and III. The overall scan was 1200 Gauss wide and centered about g = 2.

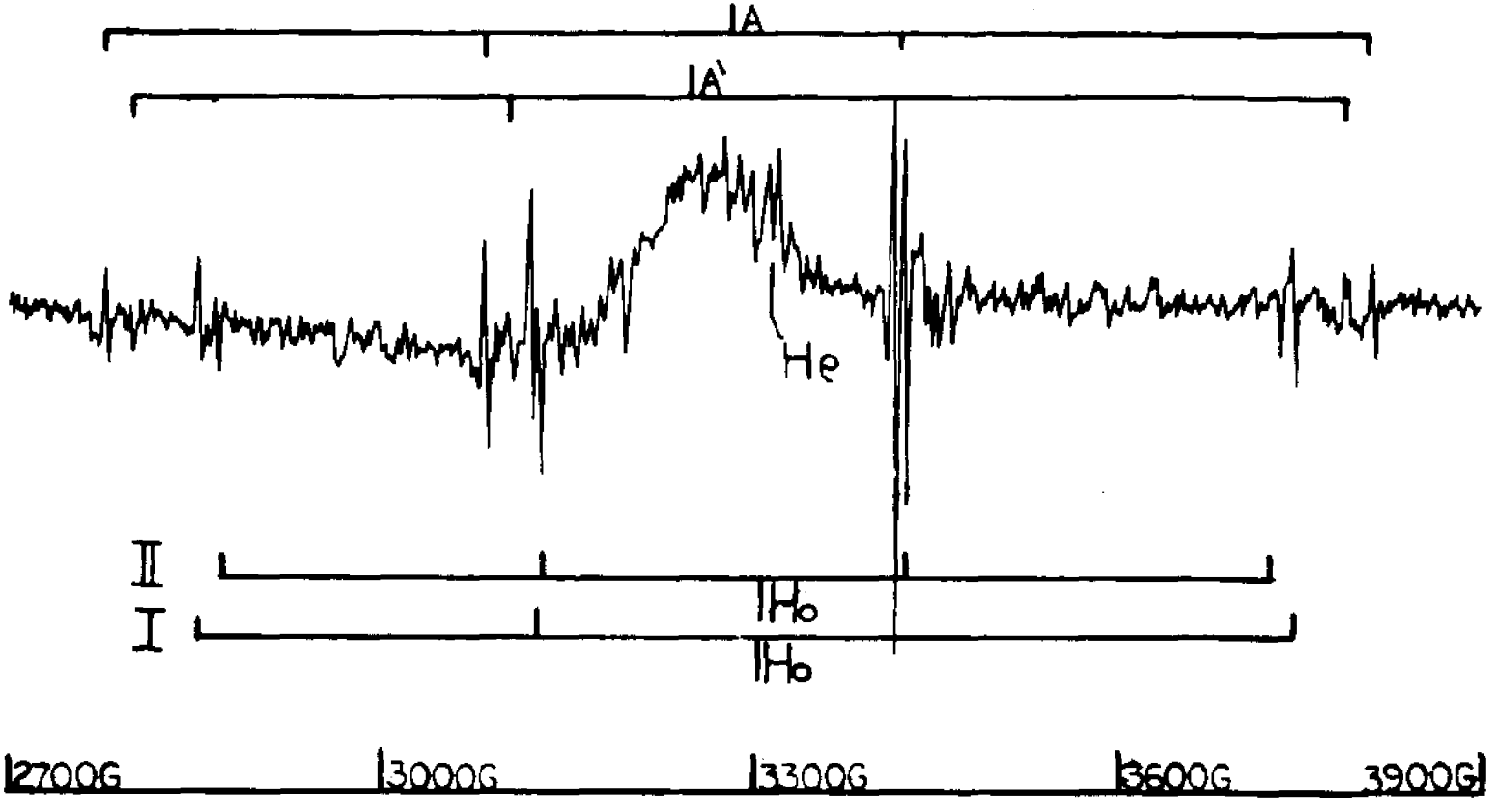
IA
IA'
He
II
I
Ho
Ho
2700G
3000G
3300G
3600G
3900G

Fig. IV.15. ESR Spectrum of KMg in an Argon Matrix.

The ESR spectrum of the mixed-metal clusters of KMg in an argon matrix at 4K. The transition labelled A was from the ^{39}K atom transition, along with a second set of quartets assigned to the ^{41}K isomer, (17). The remaining transitions were assigned to the mixed clusters and were labelled I, II, and III. The overall scan was 325 Gauss wide and centered about g = 2.

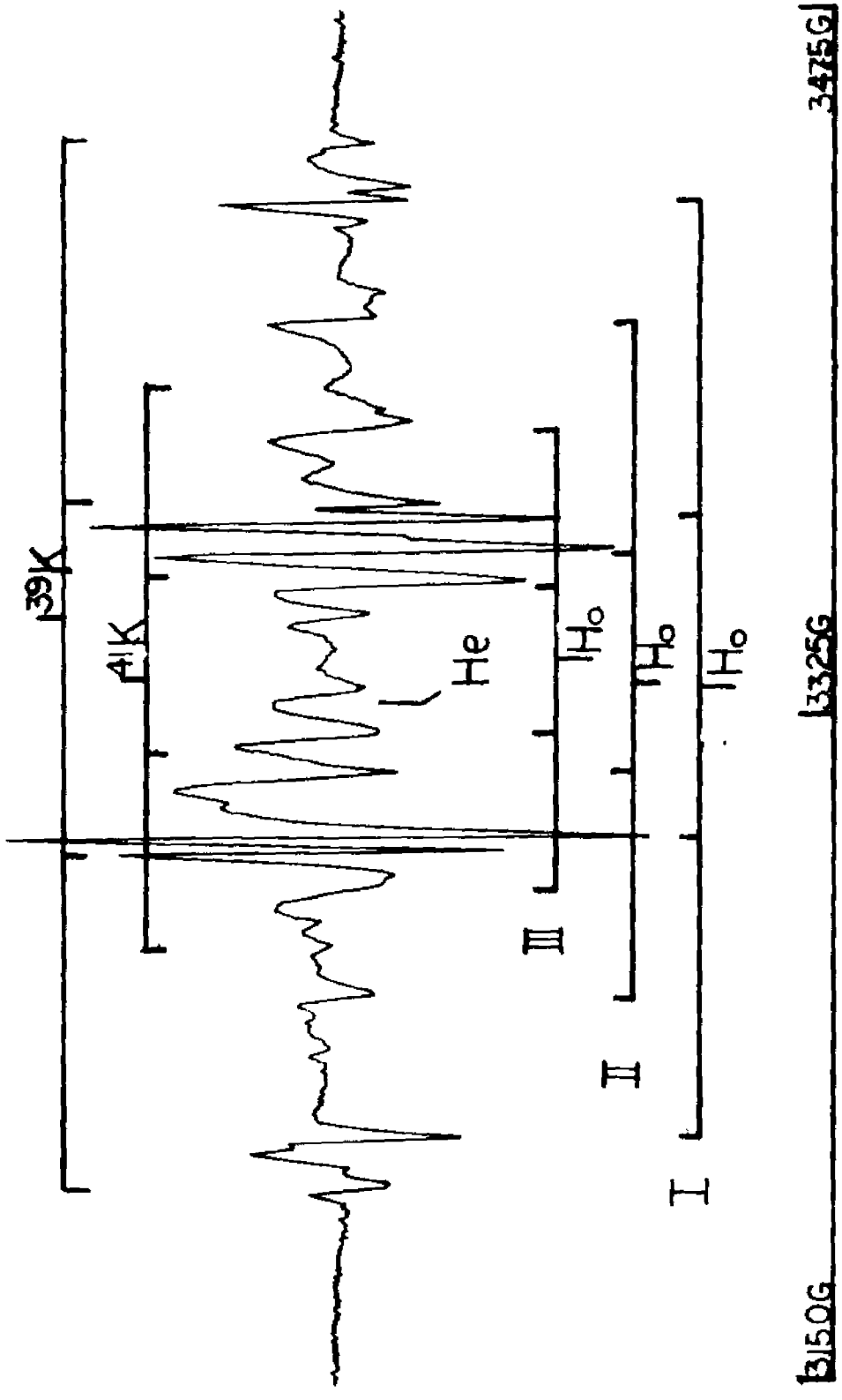
3150G
3325G
3475G
39K
41K
He
H₀
H₀
H₀
I
II
III

Fig. IV.16. ESR Spectrum of KCa in an Argon Matrix.

The ESR spectrum of the mixed-metal clusters of KCa in an argon matrix at 4K. The two quartet transitions labelled A and A' were from the ^{39}K atom transition, along with a second quartet labelled II that was assigned to the ^{41}K isomer, (17). The remaining transitions labelled I and III were assigned to the mixed clusters specie KCa and a methyl radical impurity. The overall scan was 325 Gauss wide and centered about g = 2.

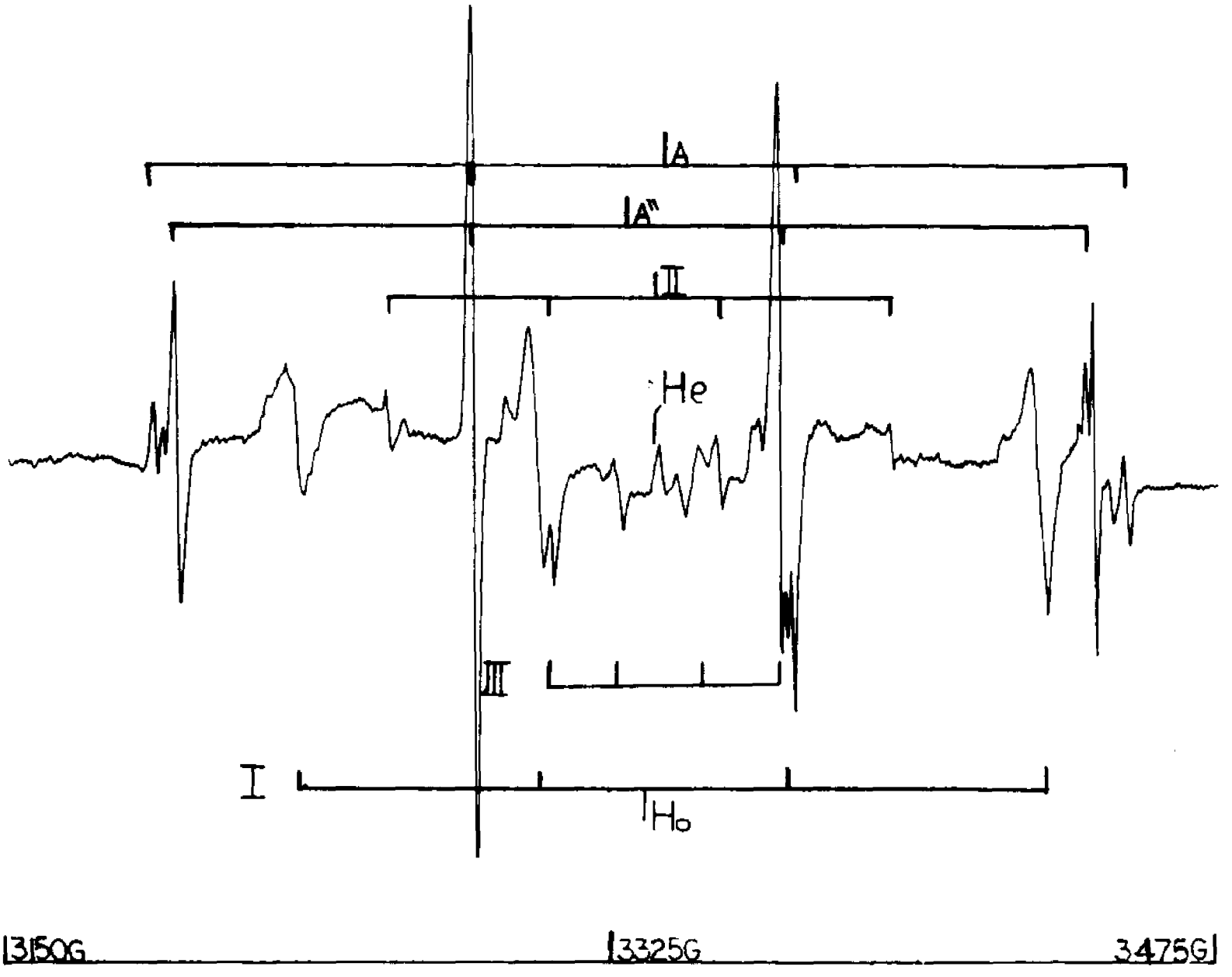
A
A''
II
He
III
I
Ho
3150G
3325G
3475G

TABLE IV.1. .Line Positions of $^{107}Ag_3$ in an N_2 Matrix.

Type	m	M	H(meas)[a]	H(cal)[b]	Diff.
//	+1/2	+1	3094.9	3094.4	+0.5
		0	3171.4	3171.2	+0.2
		-1	-------	3248.2	-----
⊥	+1/2	+1	3158.7	3159.5	- 0.8
		0	3234.3	3234.0	+0.3
		-1	3308.0	3308.9	- 0.9
//	-1/2	+1	3409.2	3409.2	0.0
		0	3486.8	3486.4	+0.4
		-1	3563.7	3563.4	+0.3
⊥	-1/2	+1	3478.7	3475.3	- 0.6
		0	3554.0	3554.0	0.0
		-1	3627.5	3628.3	-0.8

a. Field positions in units of Gauss.
b. Calculated using IBM program program labelled "'ESR 1", derived from eq. (4.1) and in the original paper, (72).

TABLE IV.2. Parallel and perpendicular parameters for $^{107}Ag_3$ in a nitrogen matrix and gas phase parameters for the ^{107}Ag atom. Units are in Gauss[a].

	Matrix	g	A (1)[c]	A(2)[c]
$^{107}Ag_3$ (//)	N_2	1.9933(3)	310.8(6)	76.0(2)
$^{107}Ag_3$ ($\perp$)	N_2	1.9558(3)	310.1(6)	72.2(2)
^{107}Ag atom	N_2	2.0010(3)	637.5(13)	
^{107}Ag atom[b]	GP	2.0023(10)	611.09(1)	

a. H.F. constants in Gauss are related to hf constants in ergs by $g_e\beta_e$ in ergs G^{-1}.
b. Gas phase constants from reference, (77).
c. Here (1),(2) refer to the apical and basal atoms respectively.

TABLE IV.3. Optical Assignment for Silver Clusters in Nitrogen and Argon Support Matrices. Bands are in nm Units.

Clusters	Matrices					
	Ar^a	$N_2{}^a$	Ar^b	Kr^b	Ne^c	GP^d
Ag	300-320	309-327	298-314	310-340	300-320	304-320
Ag_2	256		220	260-275		435
	381		254	390		279
						261-270
						266
						256
						249
Ag_3	440	402	225-240	220-250		
	360		280	280		
			360	350		
			440	410		
Ag_4				350		
$Ag_n{}^e$		570				

a. Bands assignments from our experimental results.
b. From Ozin et al., (67).
c. From Gruen et al., (84).
d. From Schultze et al., (85).
e. In this assignment n > 3.

TABLE IV.4. Rotationally Averaged Hypefine Constants $A_{//}$, $A_{\perp}$ (1 or 2) for the Apical (1) and Basal (2) Atoms for $^{107}Ag_3$. The Axes X, Y, Z are the same as in Fig. (4.10). For the Apical atom $\alpha = 0^{o}$.

Rotation axis and nuclei	$A_{//}$	$A_{\perp}$	$A_{//} \cdot A_{\perp}$[a]
X ($\perp$ Plane)	$a-\beta$	$a+1/2\beta$	$-3/2\beta$
Y (C_2 axis)	$a+\beta(3\cos^2\alpha-1)$	$a+1/2\beta(3\sin^2\alpha-2)$	$3/2\beta(3\cos^2\alpha-1)$
Z	$a+\beta(3\sin^2\alpha-1)$	$a+1/2\beta(3\cos^2\alpha-2)$	$3/2\beta(3\sin^2\alpha-1)$
Basal	76.02 (2)	72.60 (2)	3.4
Apical	310.80 (6)	310.1 (6)	0.7

a. Units are given in Gauss and are obtained by taking the difference of $A_{//}$ - $A_{\perp}$ (1 and 2) from table (4.1).

TABLE IV.5. Isotropic Hyperfine Constants and Spin Populations for $^{107}Ag_3$ and ^{107}Ag in a Nitrogen Support Matrix

Nucleus	a	$\rho_{5s}(1)^a$	$\rho_{5s}(1)^b$	$\rho_{5s}(1)^c$
Apical (1)	310.3 (6)	0.51	0.49	0.5
Basal (2)	73.7 (2)	0.12	0.13	0.12
Atom	637.5 (13)	1.04		

a. Isotropic spin populations $\rho_{5s}(1)$ and $\rho_{5s}(2)$ are ratios of corresponding h.f. values to the gas-phase constant ^{107}a = 611.1G, (78).
b. Calculated from *Ab-initio* methods, (80).
c. Calculated from LSD and SCF-Xα methods, (79).

TABLE IV.6 Line Positions of $NaMg_n$ in an Ar Matrix.

Sites[a]	H(meas)[b]	H(cal)[c]	Diff.
A	2841.5(1)	2831.4(4)	+ 0.1
	3162.4(2)	3162.2(1)	+ 0.2
	3492.7(1)	3493.1(1)	- 0.4
	3824.2(1)	3824.0(1)	+ 0.2
A'	2847.5(1)	2847.8(2)	- 0.3
	3167.2(1)	3166.8(1)	+ 0.4
	3486.0(1)	3485.8(2)	+ 0.2
	3804.5(2)	3804.8(1)	- 0.3
I	2896.7(1)	2896.2(3)	+ 0.5
	3182.4(1)	3182.5(4)	- 0.1
	3467.4(2)	3468.9(2)	- 1.5
	3756.2(3)	3755.2(1)	+ 1.0
I'	2908.3(2)	2908.5(3)	- 0.2
	3186.1(2)	3186.8(4)	- 0.7
	3467.2(1)	3465.1(6)	+ 2.1
	3742.3(2)	3743.4(3)	- 1.1

TABLE. IV.6. (Continued)

Sites[a]	H(meas)[b]	H(cal)[c]	Diff.
II	2962.0(1)	2961.5(8)	+ 0.5
	3203.9(2)	3204.2(5)	- 0.3
	3445.5(1)	3446.8(5)	- 0.9
	3689.5(1)	3689.5(8)	+ 0.7
III	3038.7(3)	3041.7(9)	- 3.0
	3232.7(2)	3228.8(5)	+ 3.9
	3416.9(3)	3415.9(6)	+ 1.0
	3601.0(3)	3603.0(9)	- 2.0

a. Sites labelled A, A' and sites Labelled I, II, and III are from the Na atom and and the mixed-metal clusters respectively.

b. Calculated using a least square fit.

c. Calculated using the spin Hamiltonian given by eq. (3.24). Units are given in Gauss

TABLE IV.7 Magnetic Parameters of $NaMg_n$ in an Ar Matrix.

Sites[a]	g-values	a_o(G)[b]	ρ[c]
A	1.9982(1)	330.2(1)	1.04(1)
A'	1.9990(2)	318.5(1)	1.01(1)
I	1.9994(6)	285.9(5)	0.905(5)
I'	1.9992(8)	277.9(7)	0.879(8)
II	1.9995(5)	242.3(4)	0.767(4)
III	2.0014(18)	187.0(16)	0.591(16)

a. Sites labelled A, A' and sites Labelled I, II, and III are from the Na atom and and the mixed-metal clusters respectively.

b. The Na atom atomic h.f. is a_{Na} = 316.1 Gauss, and $a_o = g_o$ He/ H_o.

c. $\rho_{Na} = a_o / a_{Na}$.

TABLE IV.8 Line Positions of $NaCa_n$ in an Ar Matrix.

Sites[a]	H(meas)[b]	H(cal)[c]	Diff.
A	2828.4(3)	2829.7(5)	- 1.3
	3161.2(3)	3162.6(2)	- 1.4
	3501.9(7)	3495.5(3)	+ 6.4
	3824.4(5)	3828,4(9)	- 3.9
I	2960.0(9)	2960.4(20)	- 0.4
	3203.8(6)	3204.7(13)	- 0.5
	3451.9(5)	3449.2(13)	+ 2.8
	3691.8(9)	3693.4(20)	- 1.6
I	2970.6(6)	2969.5(15)	+ 1.1
	3210.8(9)	3212.5(13)	- 1.7
	3455.6(9)	3455.5(13)	+ 0.1
	3699.0(10)	3698.4(15)	+ 0.6
I	2976.4(13)	2975.6(20)	+ 0.8
	3220.0(10)	3219.5(12)	+ 0.5
	3460.1(10)	3463.5(10)	- 3.4
	3709.5(13)	3707.4(20)	+ 2.1

a. Sites labelled A, and I, are from the Na atom and the mixed-metal clusters respectively.

b. Calculated using a least square fit.

c. Calculated using the spin Hamiltonian given by eq. (3.24). Units are given in Gauss

TABLE IV.9 Magnetic Parameters of $NaCa_n$ in an Ar Matrix.

Sites[a]	g-values	a_o(G)[b]	ρ[c]
A	2.0017(2)	332.8(3)	1.05(2)
I	2.0029(2)	244.3(3)	0.773(3)
I	1.9986(5)	242.5(4)	0.767(4)
I	1.9941(10)	242.9(10)	0.768(10)

a. Sites labelled A, and I, are from the Na atom and and the mixed-metal clusters respectively.

b. The Na atom atomic h.f. is a_{Na} = 316.1 Gauss, and $a_o = g_o$ He/ H_o.

c. $\rho_{Na} = a_o / a_{Na}$.

TABLE IV.10 Line Positions of $NaSr_n$ in an Ar Matrix.

Sites[a]	H(meas)[b]	H(cal)[c]	Diff.
A	2829.4(5)	2828.4(6)	+ 1.3
	3157.2(6)	3159.3(4)	- 2.1
	3490.4(3)	3490.1(5)	+ 0.3
	3821.5(5)	3821.0(6)	+ 0.5
I	2995.5(9)	2996.1(5)	- 0.6
	3243.3(6)	3242.0(4))	+ 1.3
	3487.3(5)	3487.8 (3)	- 0.5
	3733.6(9)	3733.6(6)	0.0

a. Sites labelled A, and I, are from the Na atom and the mixed-metal cluster respectively.

b. Calculated using a least square fit.

c. Calculated using the spin Hamiltonian given by eq. (3.24). Units are given in Gauss

TABLE IV.11 Magnetic Parameters of $NaSr_n$ in an Ar Matrix.

Sites[a]	g-values	a_o(G)[b]	ρ[c]
A	2.0001(7)	330.6(8)	1.04(7)
I	1.9762(6)	242.6(7)	0.767(6)

a. Sites labelled A, and I, are from the Na atom and and the mixed-metal clusters respectively.

b. The Na atom atomic h.f. is a_{Na} = 316.1 Gauss, and $a_o = g_o$ He/ H_o.

c. $\rho_{Na} = a_o / a_{Na}$.

TABLE IV.12 Line Positions of $NaBa_n$ in an Ar Matrix.

Sites[a]	H(meas)[b]	H(cal)[c]	Diff.
A	2828.8(14)	2825.7(12)	+ 3.4
	3146.7(12)	3150.2(10)	- 3.5
	3471.7(9)	3474.7(9)	- 2.0
	3801.6(14)	3799.1(12)	+ 2.5
A'	2837.3(15)	2846.4(13)	- 9.1
	3158.2(11)	3161.4(10)	- 3.2
	3461.9(10)	3476.3(8)	- 14.4
	3785.9(15)	3791.3(13)	- 5.4
I	2885.0(5)	2884.6(3)	+ 0.4
	3166.7(3)	3167.8(2)	- 1.1
	3452.0(2)	3451.0(3)	+ 1.0
	3734.0(5)	3734.2(3)	- 0.2
II	2896.1(5)	2895.8(3)	+ 0.3
	3171.0(2)	3171.9(4)	- 0.9
	3448.8(3)	3447.8(2)	+ 1.0
	3723.6(5)	3723.9(3)	- 0.3

a. Sites labelled A, and I, are from the Na atom and the mixed-metal clusters respectively.

b. Calculated using a least square fit.

c. Calculated using the spin Hamiltonian given by eq. (3.24). Units are given in Gauss.

TABLE IV.13 Magnetic Parameters of $NaBa_n$ in an Ar Matrix.

Sites[a]	g-values	a_o(G)[b]	ρ[c]
A	2.0074(1)	325.7(2)	1.02(2)
A'	2.0036(3)	315.2(2)	0.997(3)
I	2.0093(4)	284.2(3)	0.899(4)
II	2.0090(4)	276.9(3)	0.876(4)

a. Sites labelled A, A'and I, II, are from the Na atom and and the mixed-metal clusters respectively.

b. The Na atom atomic h.f. is a_{Na} = 316.1 Gauss, and $a_o = g_o$ He/ H_o.

c. $\rho_{Na} = a_o / a_{Na}$.

TABLE IV.14 Line Positions of KMg_n in an Ar Matrix.

Sites[a]	H(meas)[b]	H(cal)[c]	Diff.
A	3197.4(5)	3198.0(3)	- 0.6
	3290.2(3)	3289.3(2)	+ 0.9
	3380.5(4)	33380.5(1)	0.0
	3471.5(5)	3471.8(2)	- 0.3
I	3209.2(4)	3208.9(8)	+ 0.3
	3286.8(5)	3287.3(2)	+ 0.5
	3366.0(3)	3365.7(1)	+ 0.3
	3444.2(4)	3444.1(7)	+ 0.1
II	3243.6(6)	3243.3(3)	+ 0.3
	3299.7(4)	3300.1(2)	- 0.4
	3357.2(5)	3357.0(2)	+ 0.2
	3413.9(6)	3413.8(2)	+ 0.1
III	3270.1(5)	3269.7(2)	+ 0.4
	3308.3(2)	3308.4(4)	- 0.1
	3445.8(3)	3447.1(2)	- 1.3
	3386.6(5)	3385.8(2)	+ 0.8

a. Sites labelled A, and I, II, and III are from the ^{39}K atom and the mixed-metal clusters respectively.

b. Calculated using a least square fit.

c. Calculated using the spin Hamiltonian given by eq. (3.24). Units are given in Gauss.

TABLE IV.15 Magnetic Parameters of KMg_n in an Ar Matrix.

Sites[a]	g-values	a_o(G)[b]	ρ[c]
A	1.9900(3)	90.74(3)	1.11(3)
I	1.9950(2)	78.11(2)	0.958(2)
II	1.9937(1)	56.60(2)	0.695(2)
III	1.9943(6)	38.54(5)	0..472(5)

a. Sites labelled A, and I, II, and III are from the Na atom and and the mixed-metal clusters respectively.

b. The K atom atomic h.f. is a_K = 81.9 Gauss, and $a_o = g_o$ He/ H_o.

c. $\rho_K = a_o / a_K$.

TABLE IV.16 Line Positions of KCa_n in an Ar Matrix.

Sites[a]	H(meas)[b]	H(cal)[c]	Diff.
A	3193.5(3)	3193.9(6)	+ 0.4
	3286.1(3)	3285.0(2)	+ 1.1
	3375.0(2)	3376.0(2)	- 1.0
	3467.4(3)	3467.1(5)	+ 0.3
A'	3198.8(2)	3198.0(5)	+ 0.8
	3284.5(3)	3285.5(3)	- 1.0
	3372.4(2)	3372.9(1)	- 0.5
	3461.0(2)	3461.0(4)	+ 0.6
I	3229.8(3)	3229.6(3)	+ 0.2
	3300.0(2)	3300.5(4)	+ 0.1
	3370.8(1)	3371.4(2)	- 0.6
	3442.8(3)	3442.3(3)	+ 0.5
II	3256.2(5)	3255.8(2)	+ 0.4
	303.1(3)	3303.4(2)	- 0.3
	3350.4(2)	3351.0(3)	- 0.6
	3399.1(5)	3398.6(3)	+ 0.5

TABLE. IV.16. (Continued)

a. Sites labelled A, A' and II are from the ^{39}K and ^{41}K atoms. Site labelled I, is from the mixed metal clusters.
b. Calculated using a least square fit.
c. Calculated using the spin Hamiltonian given by eq. (3.24). Units are given in Gauss

TABLE IV.17 Magnetic Parameters of KCa_n in an Ar Matrix.

Sites[a]	g-values	a_o(G)[b]	ρ[c]
A	1.9900(3)	90.74(3)	1.11(3)
A'	1.9950(2)	78.11(2)	0.958(2)
I	1.9937(1)	56.60(2)	0.695(2)
II	1.9943(6)	38.54(5)	0..472(5)

a. Sites labelled A, A" were assigned to the ^{39}K atom , while site labelled II to the ^{41}K isomer. The remaining quartet was due to the mixed-metal cluster.
b. The K atom atomic h.f. is a_K = 81.9 Gauss, and $a_o = g_o$ He/ H_o.
c. $\rho_K = a_o / a_K$.

Appendix I. Reprint by permission of the American Institute of Physics: J. Chem. Phys., **82**, 4739 (1985)

ESR spectra of $Ag_3(^2A_1)$ in an N_2 matrix

K. Kernisant, G. A. Thompson,[a] and D. M. Lindsay
Department of Chemistry, City University of New York, The City College, New York, New York 10031

(Received 29 January 1985; accepted 1 March 1985)

ESR spectra assigned to Ag_3 molecules have been produced by codepositing atomic silver with excess nitrogen at temperatures close to 4.2 K. The spectra are characterized by an axially symmetric spin Hamiltonian having $g_\parallel = 1.9933(3)$ and $g_\perp = 1.9558(3)$ and, for $^{107}Ag_3$, $A_\parallel = 310.8(6)$ G with $A_\perp(1) = 310.1(6)$ G and $A_\perp(2) = 76.0(2)$ G with $A_\perp(2) = 72.6(2)$ G for the apical(1) and basal(2) nuclei, respectively. The axial symmetry of the spectra is believed to imply that the trimer is rotating about one axis. There is no evidence for a pseudorotating trimer spectrum. The isotropic spin populations are $\rho_{3s}(1) = 0.51$ and $\rho_{3s}(2) = 0.12$ implying an acute angled geometry with ground state symmetry $^2A_1$. This is in sharp contrast to the obtuse angled isomer ($^2B_2$ ground state) found for Ag_3 in a C_6D_6 matrix. For Ag_3 ($^2A_1$) there is little p character on the apical atom but a 10%–15% p hybridization on each of the two basal nuclei.

I. INTRODUCTION

The equilateral triangle is an unstable geometry for both the Group IA and Group IB metal trimers.[1,2] A Jahn–Teller distortion removes the electronic degeneracy present in D_{3h} symmetry, giving rise to an isosceles geometry (point group C_{2v}) with apical angle either greater than or less than 60° (the "obtuse" and "acute" isomers, respectively). The two C_{2v} isomers are predicted to have radically different spin populations. The obtuse trimer, with a $^2B_2$ ground state, is characterized by a large spin population on the two terminal atoms and (at the simple Hückel level) a node on the central atom. For the acute isomer ($^2A_1$ ground state) the spin population on the apical atom is predicted to be large and, again at the simple Hückel level, approximately four times that on each of the two basal atoms.

For the Group IA trimers Na_3[1] and K_3[2] and for Ag_3 in a deuterobenzene matrix,[3] the ground state is found to be $^2B_2$. In the case of Li_3, the acute and obtuse geometries are equienergic and the trimer is best described as being a completely fluxional molecule with (on average) equal spin populations on all three atoms.[4,5] The silver trimer electron spin resonance (ESR) spectra reported here give isotropic spin populations of 51% on one nucleus and 12% on each of two additional nuclei. This is conclusive evidence for a $^2A_1$ ground state for Ag_3 in a nitrogen matrix.

II. EXPERIMENTAL

Silver trimers were formed by codepositing atomic silver, either naturally occurring (Alfa, 99.9%) or isotopically enriched (Oak Ridge National Laboratory, 98.2% ^{107}Ag), with excess nitrogen (Airco, 99.9995%) on a polished OFHC copper target (width 5/32 in., thickness 0.031 in.) mounted inside a TE_{102} X-band cavity. The cavity was attached to a variable temperature cryostat, whose design has been described previously.[6] The copper target was counterbored to a depth of 0.026 in. in order to accommodate a small quartz (Dynasil 4000) window of diameter 0.094 in. (Hibshman Corp., San Luis Obispo, CA). The quartz window was held in place with a minimum amount of GE 7031 adhesive. With this arrangement it is possible to obtain both ESR and optical absorption spectra of the same matrix sample. Silver was evaporated from a directly heated tantalum boat (R. D. Mathis, ME-10) supported on two water cooled electrodes and surrounded by a water cooled radiation shield. During an experimental run the metal flux was periodically monitored with a quartz microbalance. The microbalance used a commercial controller and oscillator (Veeco, QM-301) but had a carefully designed sensor head which optimized the thermal contact between the quartz crystal and its water cooled mount. Further details of the evaporation source can be found elsewhere.[6] For the $^{107}Ag_3$ spectra presented here, the N_2:Ag ratio is estimated to be 85:1. Approximately 0.35 μmol/h of Ag were incident on the copper target for a total deposition time of about 1 h. Matrices were grown at temperatures close to 4.2 K and then annealed to ~25 K. The ESR spectrum of Ag_3 was observed in freshly grown matrices, but its resolution is dramatically improved by annealing. No further irreversible changes were observed, providing the matrix temperature did not exceed 30–35 K. Matrix temperatures were measured and controlled with a Scientific Instruments model 5500 cryogenic controller and a GaAs sensor. Despite several attempts, no ESR spectra attributable to Ag_3 were observed for Ar, Kr, or Xe matrices.

All spectra were recorded on an IBM-Bruker ER 200D EPR spectrometer using 100 kHz magnetic field modulation (peak-to-peak amplitude ~3 G) and phase-sensitive detection. ESR spectra could be further processed by averaging repetitive scans on a multichannel analyzer (Tracor Northern, TN 1710). Acquisition times ranged from 5000–10 000 s. For $T \gtrsim 20$ K a microwave power of 20 mW was found to be optimum. The resonance frequency of the cavity plus copper target and matrix sample was measured periodically with a microwave frequency counter (HP 5245L plus HP 5255A plug-in). Individual spectra were calibrated with a proton magnetometer (Micronow, model 515). Relative and absolute field positions are judged accurate to ± 0.2% and ± 0.5 G, respectively.

[a] Present Address: Molecular Spectroscopy Division, National Bureau of Standards, Washington, D.C. 20234.

 0021-9606/85/114739-06$02.10

TABLE II. Rotationally averaged hf constants A_1(1 or 2) and A_2(1 or 2) for the apical(1) and basal(2) nuclei of Ag_3. For the apical nucleus $\alpha = 0$. The axes x, y, z are defined in Fig. 2.

Rotation axis	A_1	A_2	$1/3(A_1 + 2A_2)$	$A_1 - A_2$
x	$a - \beta$	$a + \frac{1}{2}\beta$	a	$-3/2\,\beta$
y	$a + \beta(3\cos^2\alpha - 1)$	$a + \frac{1}{4}\beta(3\sin^2\alpha - 2)$	a	$3/2\,\beta(3\cos^2\alpha - 1)$
z	$a + \beta(3\sin^2\alpha - 1)$	$a + \frac{1}{4}\beta(3\cos^2\alpha - 2)$	a	$3/2\,\beta(3\sin^2\alpha - 1)$

have axial symmetry. This phenomenon is not unknown, the best documented case being NO_2 in an argon matrix.[33] Unlike NO_2, however, the three principal moments of inertia for the silver trimer are comparable in magnitude, so that a unique rotational axis is not immediately apparent.[34] Table II summarizes rotationally averaged hf constants obtained by rotating the static tensors, Eqs. (4) and (5), about either the x, y, or z axes and then averaging each tensor element over all orientations. For both nuclei, the Fermi contact term $a = 1/3(A_1 + 2A_2)$, independent of rotational axis. The entries in column 5 of Table II show that the anisotropic parameter $A_1 - A_2$ may be either positive or negative. However, the experimental anisotropies, $A_1(1) - A_2(1) = 0.7$ G and $A_1(2) - A_2(2) = 3.4$ G from Table I, are both positive.[35] This would imply that the trimer rotates about the molecular C_2 axis, which is also the axis with the smallest moment of inertia.[34] While this conclusion is statistically significant,[34] the dipolar hyperfine analysis (particularly for the apical nucleus) is complicated by a relatively large pseudohyperfine interaction (see below) and a rotation about the z axis should not be ruled out.[36]

Table III gives the experimental isotropic parameters for the case of a silver trimer rotating about a principal axis. The isotropic spin populations[37] $\rho_{s_1}(1)$ on the apical atom and $\rho_{s_2}(2)$ on each of the two basal atoms are, respectively, hf constants $a(1)$ and $a(2)$ divided by the corresponding gas-phase parameter, $^{107}a_{5s} = 611.1$ G.[18] An analogous appraisal of the trimer anisotropic spin populations is less straightforward. Since for unit spin population in a ^{107}Ag $5p$ orbital $\beta_{5p} \sim 9.0$ G,[18] this suggests an apical atom p character $\rho_{5p}(1) \lesssim 2\%$–$3\%$. An analysis of the p character on the two basal atoms requires a value for the orbital orientation angle α. However, the sum of the isotropic spin populations is $\rho_{s_1}(1) + 2\rho_{s_2}(2) = 0.75$ and, since the total (isotropic + anisotropic) spin population should be close to unity, the ESR spectra imply $\rho_{5p}(2) \lesssim 15\%$ or $\beta(2) \lesssim 1\frac{1}{2}$ G. For this situation the expressions in the last column on Table II satisfy $A_2 - A_1 \approx 3.4$ G only if α is relatively close either to 0° or to 90°, corresponding to a rotational averaging about the y axis or the x axis, respectively. This suggests that the bonding between the two basal atoms should be viewed as either nearly π or nearly σ in character.

TABLE III. Isotropic hf constants and spin populations for ^{107}Ag$_3$ and ^{109}Ag$_3$ in nitrogen matrices.

Nucleus	a	ρ_{s_i}*
Apical(1)	310.3(6)	0.51
Basal(2)	73.7(2)	0.12
Atom	637.5(13)	1.04

*Isotropic spin populations $\rho_{s_1}(1)$ and $\rho_{s_2}(2)$ are ratios of corresponding a values to gas-phase constant $^{107}a = 611.1$ G (Ref. 18).

V. THE g TENSOR AND PSEUDOHYPERFINE INTERACTION

Figure 3 shows a molecular orbital (MO) scheme for the ground $\cdots 1a_2^2 2a_1$ configuration of Ag_3. This figure draws heavily from the SCF-CI calculations of Basch[29] and from the Walsh type correlation diagrams for AB_2 and B_3 molecules discussed by Gimarc.[30] Since $\Delta g_\parallel = -0.0090$ and $\Delta g_\perp = -0.0465$ are both *negative* this implies dominant contributions to the g-tensor anisotropy from spin-orbit coupling to the empty molecular orbitals of the s and p manifold.[15,31] Although molecular structure calculations disagree as to the relative order of $2a_1$ and $1b_2$ (see later

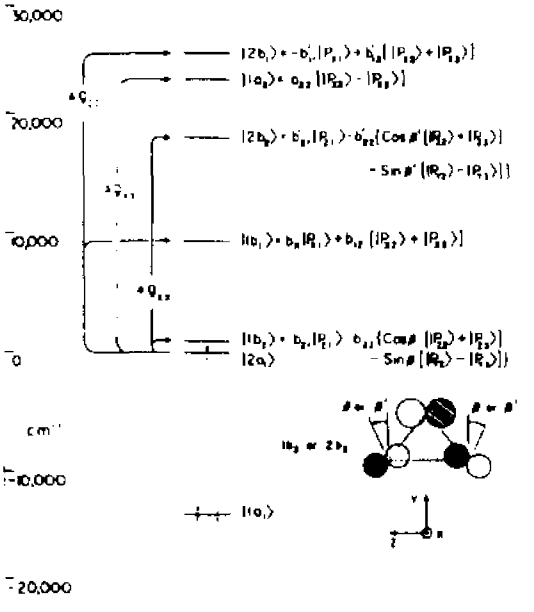

FIG. 3. Molecular orbital diagram for the s manifold and, in part, the p manifold of Ag_3 showing principal contributions to the trimer g tensor. The LCAO expressions give the p character for each orbital. The atomic axes x_1, y_1, z_1, etc. are defined in Fig. 2.

TABLE I. Parallel (∥) and perpendicular (⊥) parameters for $^{107}Ag_3$ in a nitrogen matrix and ^{107}Ag parameters. Estimated errors (see the text) are given in parentheses. Units are Gauss.[a]

	Matrix	g	A (1)	A (2)
$^{107}Ag_3$(∥)	N_2	1.9933(3)	310.8(6)	76.0(2)
$^{107}Ag_3$(⊥)	N_2	1.9958(3)	310.1(6)	72.6(2)
^{107}Ag atom	N_2	2.0010(3)	637.5(13)	
^{107}Ag atom[b]	Ar	2.0007(3)	640.8(13)	
^{107}Ag atom[c]	GP	2.0023(10)	611.09(1)	

[a] hf constants in Gauss are related to hf constants in ergs by $g_n\beta_n$ ergs G^{-1}. See also Refs. 7 and 16.
[b] The authors of Ref. 8 give $g = 1.9998(1)$ with $A = 645.7(1)$ G.
[c] Gas-phase constants from Ref. 18.

powder pattern.[17] No such effects were observed.

Table I gives the magnetic parameters $g_\parallel$, $g_\perp$ and $A_\alpha(1)$, $A_\alpha(2)$ used in the simulated spectrum, Fig. 1(b). The line shape function was a Gaussian derivative with a peak-to-peak width (ΔH_{pp}) of 5.5 G. By comparison, atomic silver in N_2 has a Lorentzian line shape with $\Delta H_{pp} = 9.0$ G. The stick spectrum assignment shown in Fig. 1 represents the transition fields of Eq. (3) using the constants of Table I. Estimated errors given in parentheses in this table correspond to the calibration uncertainties noted earlier. The average difference between the experimental and calculated (parallel and perpendicular) features is 0.4 G. Also given in Table I are the g value and (isotropic) hf constant for atomic silver in N_2 and Ar matrices and in the gas phase.[18]

For unenriched silver, a total of six distinct isomers are formed, giving rise to 48 parallel and 48 perpendicular transitions. Since the natural abundances of ^{107}Ag and ^{109}Ag are 51.8% and 48.2%, respectively,[19] the six isomers give comparably intense ESR spectra. Nevertheless, except when overlapped by atomic silver transitions, the perpendicular features are quite well resolved.[20] Within the experimental errors quoted in Table I, the measured $g_\perp$, $^{107}A_\perp(1)$, and $^{107}A_\perp(2)$ are the same as those obtained from the enriched sample. Moreover, the observed hf constant ratio, $^{109}A_\perp/^{107}A_\perp = 1.153(3)$, is in good agreement with that predicted from the ratio of nuclear moments, $\mu_{109}/\mu_{107} = 1.1544$.[21]

IV. HYPERFINE STRUCTURE

Figure 2 illustrates the 5s and 5p character expected for the partially occupied $2a_1$ orbital of Ag_3. Since $g_\parallel$ and $g_\perp$ are both less than g_e, it will be assumed that there is no significant admixture of d character from the filled 4d manifold of the trimer. Thus the anisotropy in the ESR spectrum will arise from p-orbital spin populations, $\rho_{5p}(1)$ on the apical atom (labeled 1 in Fig. 2) and $\rho_{5p}(2)$ on each of the two basal atoms (labeled 2 and 3). The corresponding isotropic spin populations are denoted $\rho_{5s}(1)$ and $\rho_{5s}(2)$. In the g-tensor principal axes (x, y, z in Fig. 1), the (axially symmetric) hf tensor for the apical nucleus is given by[15] the sum of the Fermi contact and dipole–dipole terms, $A(1) = a(1)\mathbb{1} + T(1)$,

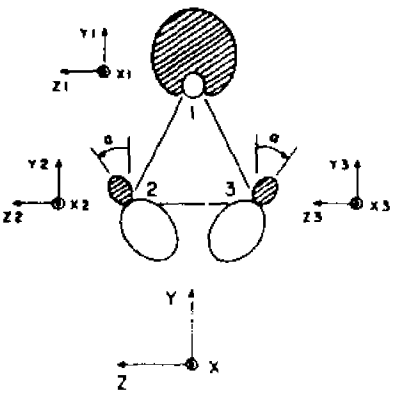

$$|2a_1\rangle = -a_{1s}|P_{y1}\rangle - a_{1p}\{\cos\alpha[|P_{y2}\rangle + |P_{y3}\rangle] + \sin\alpha[|P_{z2}\rangle - |P_{z3}\rangle]\}$$

FIG. 2. Qualitative hybridization scheme for the partially occupied $2a_1$ orbital of Ag_3. Although 75% s in character, only p-orbital coefficients are included in the LCAO expression for $|2a_1\rangle$. Also shown are atomic axes ($x1$, $y1$, $z1$), etc. and molecular g-tensor axes (x, y, z).

with

$$T(1) = \beta(1)\begin{pmatrix} -1 & 0 & 0 \\ 0 & +2 & 0 \\ 0 & 0 & -1 \end{pmatrix}, \tag{4}$$

where $a(1) = \rho_{5s}(1)a_{5s}$ and $\beta(1) = \rho_{5p}(1)\beta_{5p}$. The parameters a_{5s} and β_{5p} are hf splitting constants for unit spin populations in a ^{107}Ag 5s and 5p orbital, respectively. Since, in general, the p orbitals located on the basal nuclei are oriented at some angle $\pm\alpha$ in Fig. 2) with respect to the molecular C_3 axis, the hf tensors for these two nuclei are neither axially symmetric nor diagonal in the x, y, z frame. Thus for nucleus 2, $A(2) = a(2)\mathbb{1} + T(2)$, but now[17]

$$T(2) = \beta(2)\begin{pmatrix} -1 & 0 & 0 \\ 0 & 3\cos^2\alpha - 1 & 3\sin\alpha\cos\alpha \\ 0 & 3\sin\alpha\cos\alpha & 3\sin^2\alpha - 1 \end{pmatrix} \tag{5}$$

A similar expression pertains to nucleus 3 except that $T_{xy} = T_{xy} = -3\sin\alpha\cos\alpha$. For both nuclei, the predicted hf splittings [$K_\alpha(2)$, for H parallel to $i = x$, y or z] are[22]

$$\begin{aligned} K_{xx}(2) &= T_{xx}(2) + a(2), \\ K_{yy}(2) &= \{[T_{yy}(2) + a(2)]^2 + T_{yz}(2)^2\}^{1/2}, \\ K_{zz}(2) &= \{[T_{zz}(2) + a(2)]^2 + T_{xy}(2)^2\}^{1/2}, \end{aligned} \tag{6}$$

so that (unless $\alpha = 0$ or $\pi/2$) an orthorhombic hf splitting $K_{xx}(2) \neq K_{yy}(2) \neq K_{zz}(2)$ would be expected. Since the observed hf anisotropy is not large, small deviations from axial symmetry might not be resolved in the ESR powder spectra for Ag_3. However, the g-tensor anisotropy is large and, as discussed in more detail below, a fortuitous coincidence of two g-tensor components seems unlikely.

If the trimer is assumed to rotate about one of its principal axes, then the rotationally averaged g and hf tensors will

III. SPECTRA AND ANALYSIS

Figure 1(a) shows the axially symmetric ESR spectrum observed for $^{107}Ag_3$ in an N_2 matrix at 25 K.[7] The separation into a low field and a high field group of transitions ($m = \pm 1/2$) arises, from a nearly isotropic hyperfine (hf) interaction with a single ^{107}Ag nucleus (spin, $I = 1/2$). The triplet splitting ($M = 0, \pm 1$) within each group is assigned to a smaller and more anisotropic hf interaction with two additional but equivalent ^{107}Ag nuclei. In Fig. 1(a), $H_r = 3322.4$ G is the resonance field for a free electron ($g_r = 2.002\,32$) at a cavity frequency of 9.310 78 GHz. The sharp feature at $g = 2$ is a background resonance arising from the GE 7031 adhesive. An additional but broader background signal has been partially subtracted out. Also shown are transitions due to atomic silver[8] and methyl (Me) radicals.[9] At $T = 5.2$ K, the $M = 0$ perpendicular components of $^{107}Ag_3$ are split by 1.5 and 3.0 G for $m = +1/2$ and $-1/2$, respectively. This might imply that the trimer is trapped in several matrix sites whose magnetic parameters show a small temperature dependence as has been reported for Li_3 in argon.[10] No spectra corresponding to a pseudorotating trimer[2,4,11] were observed over the temperature range $4.2 \leq T \leq 30$ K.

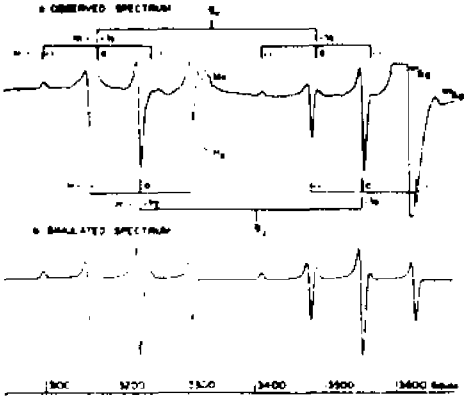

FIG. 1. Observed (a) and simulated (b) ESR spectra for $^{107}Ag_3$ in a nitrogen matrix at 25 K. The resonance field for a free electron is $H_r = 3322.4$ G. Isotopically enriched ^{107}Ag was used. For spectral assignment see the text and Ref. 7.

Figure 1(b) shows a simulated ESR spectrum computed from[12]

$$I(H) = \int \sum_{m,M,J} I(H',m,M,J)\,F(H - H')\,dH', \tag{1}$$

where

$$I(H,m,M,J) = \frac{H_\parallel(m,M,J)\,H_\perp^2(m,M,J)}{H^2\left[H_\perp^2(m,M,J) - H_\parallel^2(m,M,J)\right]^{1/2}\left[H^2(m,M,J) - H^2\right]^{1/2}} \tag{2}$$

with ($\alpha = \parallel$ or $\perp$)

$$H_\alpha(m,M,J) = \frac{g_r}{g_\alpha}\left[H_r - A_\alpha(1)m - A_\alpha(2)M\right] - \frac{g_r^2}{4g_\alpha^2 H_r}\left[A_\parallel^2(1) + 2A_\perp^2(1) - A_\alpha^2(1)\right]\left[J(J+1) - m^2\right]$$
$$- \frac{g_r^2}{4g_\alpha^2 H_r}\left[A_\parallel^2(2) + 2A_\perp^2(2) - A_\alpha^2(2)\right]\left[J(J+1) - M^2\right] \tag{3}$$

and $H_r = g_r/g_\alpha\left[H_r - A_\alpha(1)m - A_\alpha(2)M\right]$. The algorithm defined by Eqs. (1)–(3) will be referred to as I. In these expressions, $F(H - H')$ is a line shape function and $I(H,m,M,J)$ is zero for magnetic fields outside of the range $H_\parallel(m,M,J) \leq H \leq H_\perp(m,M,J)$. Equations (2) and (3) should only be used in cases where prominent features in the powder spectrum arise from molecules aligned (or closely aligned) either parallel or perpendicular to the laboratory field. In order to check its suitability here, the trimer spectrum was simulated using an entirely different algorithm which we label II.[13] The latter calculates the resonance field (to second order in A/H) for molecules oriented at all angles with the magnetic field, summing the intensity contributions from each orientation.[14] Since both simulations gave almost identical results, effects arising from "off-principal-axis transitions"[15] are assumed to be minor. The principal advantage of algorithm I is its ability to handle magnetically equivalent nuclei. Thus, in Eq. (3) the $A_\alpha(2)$ are hf constants ($\alpha = \parallel$ or $\perp$)[16] for two magnetically equivalent $I = 1/2$ nuclei whose resultant nuclear spin has magnitude $J = 0$ or 1 and projection $M = 0, \pm 1$.[17] As described in Sec. IV, the $A_\alpha(2)$ are related to, but not necessarily equal to, the principal values of the basal atom hf tensors. The principal values of the apical atom hf tensor are denoted $A_\alpha(1)$. The g_α are molecular g-tensor components for a radical with axial symmetry.

It is at first surprising that the trimer with an assumed C_{3v} geometry should have an axially symmetric ESR spectrum. As discussed in more detail in Sec. IV, this probably implies that Ag_3 is rotating about one axis. Thus the two chemically equivalent nuclei become magnetically equivalent and the principal axes of their rotationally averaged hf tensors will be parallel to the molecular g-tensor axes. Using algorithm II, several simulations were run assuming noncoincident g and A tensors. For this situation there is a magnetic equivalency only when the field is parallel or nearly parallel to a g-tensor principal axis. For all other orientations, the two $M = 0$ transitions no longer coincide (even in first order) and additional splittings might appear in the ESR

discussion), the absolute energy difference is acknowledged to be small. Since the ESR spectra show a $^2A_1$ ground state for Ag_3 in a nitrogen matrix, this places the $1b_2$ orbital a few hundred wave numbers above $2a_1$ as indicated in Fig. 3. The orbital energies for $1a_1$, $1b_1$, $2b_2$, and $1a_2$ are the adiabatic excitation energies (relative to $2a_1$ equals zero) of the corresponding $^2A_1$, $^2B_1$, $^2B_2$, and $^2A_2$ states given in Table VI of Ref. 29. A vertical excitation energy of approximately 25 000 cm^{-1} for $2b_1$ was estimated from the orbital correlation diagram, Fig. 2 of Ref. 29. Not included in Fig. 3 are the five remaining orbitals of the p manifold. These either lie higher in energy than $2b_1$ or by symmetry make no contribution to the trimer g tensor.

Also shown in Fig. 3 are orbital coefficients for those MO's pertinent to the present analysis. Atomic $5p$ orbitals are specified with respect to axes $(x1, y1, z1)$ through $(x3, y3, z3)$ centered on silver nuclei 1–3, respectively. The atomic axes and nuclear numbering are defined in Fig. 2, which also gives the orbital coefficients for $|2a_1\rangle$. Since s orbitals do not directly enter into the g-tensor calculation, these have been omitted in both figures. Using standard methods[15,31,32] the g shifts $\Delta g_\alpha = g_\alpha - g_e$ are found to be

$$-\Delta g_{\perp} = \frac{2\lambda_{5p}}{\epsilon(b_2)}\left[-a_{11}b_{21}+2a_{12}b_{22}\cos(\alpha-\beta)\right]^2 + \frac{2\lambda_{5p}}{\epsilon'(b_2)}\left[-a_{11}b_{21}+2a_{12}b_{22}\cos(\alpha-\beta')\right]^2, \tag{7}$$

$$-\Delta g_{\parallel} = \frac{8\lambda_{5p}}{\epsilon(a_2)}a_{12}^2a_{22}^2\sin^2\alpha, \tag{8}$$

$$\Delta g_{\perp} = \frac{2\lambda_{5p}}{\epsilon(b_1)}\left[a_{11}b_{11}+2a_{12}b_{12}\cos\alpha\right]^2 + \frac{2\lambda_{5p}}{\epsilon'(b_1)}\left[-a_{11}b_{11}+2a_{12}b_{12}\cos\alpha\right]^2 \tag{9}$$

In these expressions (which ignore overlap contributions), $\lambda_{5p} \sim 615\ cm^{-1}$ is the spin-orbit coupling constant for a silver $5p$ orbital[33] and ϵ, ϵ' are (positive) excited state energies for, respectively, the lowest and highest states whose symmetries are indicated in parentheses.

The g-tensor expressions contain many more parameters than are available either from the ESR hf constants or from molecule structure calculations and a definitive comparison of experimental and predicted constants is not possible. Nevertheless several general features may be noted. Unless the trimer is rotating about one axis, it is difficult to reconcile Eqs. (7)–(9) with the axially symmetric ESR spectrum observed for Ag_3.[34] The largest g shift is probably Δg_{zz} as this arises from the low lying $1b_2$ orbital.[35] Since, experimentally, $\Delta g_\parallel > \Delta g_\perp$, this implies a rotational averaging of Δg_{xx} with either Δg_{yy} or Δg_{zz}. The relative magnitudes of Δg_{yy} and Δg_{zz} are quite sensitive to the angle α. If the bonding between the basal atoms is π in character then α is small and $\Delta g_{yy} \to 0$. Since the hf analysis associates π-type bonding with a rotational averaging about the y axis, this would imply $\Delta g = \Delta g_{yy}$ and so $\Delta g_\perp = 1/2(\Delta g_{xx} + \Delta g_{zz})$. On the other hand, if the basal bond is best described as being σ in character then $\alpha \simeq \pi/2$ and, again because of the hf data, $\Delta g_\parallel = \Delta g_{zz}$ with $\Delta g = 1/2(\Delta g_{xx} + \Delta g_{yy})$. In comparison to the case of a π-type bond, Δg_{yy} is relatively large and Δg_{zz} is small.

Since spin-orbit coupling mixes a significant amount of b_1, b_2, and a_2 character into the partially occupied $2a_1$ orbital, matrix elements of the operator

$$\mathcal{H}(k) = g_e\beta_e g_N\beta_N \sum_i \frac{\mathbf{l}_{ki}\cdot\mathbf{I}_k}{r_{ki}^3} \tag{10}$$

will not be zero. The electron orbital–nuclear spin interaction gives rise to pseudohyperfine terms, $\Omega_\alpha(k)$, which add to the isotropic and dipolar tensor elements

$$A_\alpha(k) = a(k) + T_\alpha(k) + \Omega_\alpha(k). \tag{11}$$

for the apical($k = 1$) and basal($k = 2$ nuclei of the trimer.[36] In Eq. (10), g and β are the g factor and Bohr magneton for an electron or nucleus, subscript e or N, respectively. The orbital angular momentum of the ith electron is denoted $\mathbf{l}_{ki}$. $\mathbf{I}_k$ is a nuclear spin vector and r_{ki} is the distance from electron i to nucleus k. By methods similar to those used in deriving g-tensor expressions,[36] we find

$$\Omega_\alpha(k) \propto \tfrac{2}{5}\beta_{5p}\Delta g_\alpha, \tag{12}$$

where (approximately) the proportionality constants, which in some cases *may be of order unity*, are functions of the same ground and excited state orbital coefficients that appear in the g-tensor expressions, Eqs. (7)–(9). Since $\Delta g_\perp = -0.0465$ and $^{107}\beta_{5p} = 9.0\ G$,[28] then $5/2\beta_{5p}|\Delta g_\perp| \sim 1\ G$. Accordingly, the $\Omega_\alpha(k)$ may be appreciable, particularly in comparison with the small dipolar hf for the apical nucleus.

VI. DISCUSSION

For Ag_3 isolated in nitrogen matrices the ESR spectra clearly identify a $^2A_1$ ground state corresponding to a trimer having an acute angled geometry. A distinctly different result is obtained for Ag_3 in a deuterobenzene matrix,[1] for which only the obtuse angled isomer is observed. This divergence in experimental behavior is paralleled by a similar diversity in the ground state symmetries predicted by molecular structure calculations. Thus, Richtsmeier *et al.*,[37] using a diatomics-in-molecule approach, predict a $^2A_1$ ground state for Ag_3, whereas the pseudopotential + density functional results of Flad *et al.*[38] suggest the $^2B_2$ state to be more stable. Andreoni and Martins,[39] using local-spin-density (LSD) methods, find a $^2A_1$ ground state with frozen d orbitals but equal energies for the acute and obtuse geometries if d orbitals are included as part of the valence manifold. Since, in all cases, the energy difference between the two geometries is of the order of a few hundred wave numbers, it is not surprising that such disparate hosts as N_2 and C_6D_6 might stabilize one isomer in preference to another. A classic example of this effect is the ground state of atomic nickel. In the gas phase, the $^3D_3$ state lies 205 cm^{-1} above the $^3F_4$ ground state. In Ar, Kr, and Xe, however, the ground state of Ni is $^3D_3$.[40,41] In neither C_6D_6 nor N_2 is there any evidence for a pseudorotating isomer. This is probably more a function of the trimer mass than an indication of a large inversion barrier, although matrix effects might play an important role in determining phenomena as sensitive as pseudorotation.[42]

For both Ag_3 geometries, the ESR spectra show (perhaps surprisingly) large negative g shifts, phenomena associated with both low lying excited states and a ground state hybridization scheme using $5p$ as opposed to $4d$ orbitals. For Ag_3 in N_2, the measured isotropic spin populations are $\rho_{5s}(1) = 0.51$ and $\rho_{5s}(2) = 0.12$ for the apical and basal nuclei, respectively. These values are in excellent agreement with the corresponding spin populations determined by *ab initio* methods: $\rho_{5s}(1) = 0.49$ with $\rho_{5s}(2) = 0.13$[39] and $\rho_{5s}(1) = 0.53$ with $\rho_{5s}(2) = 0.12$,[43] using LSD and SCF-$X\alpha$ methods, respectively. For all three sets of data, $\rho_{5s}(1)/\rho_{5s}(2)$ is very close to the 4:1 ratio predicted by a simple Hückel model. Neither theory nor experiment give an adequate account of the anisotropic spin populations in Ag_3. However, it can be inferred from the ESR data that the wave function for the unpaired electron is dominantly $5s$ in character at the apical nucleus, but has an approximately equal admixture of $5s$ and $5p$ character at each of the two basal nuclei.

ACKNOWLEDGMENTS

We thank Dr P. H. Kasai, Dr J. L. Martins, and Dr S. M. Mattar for helpful discussions. This research was supported in part by the City University of New York PSC-BHE Faculty Research Award Program and by the National Science Foundation under grant number CHE 83-07164 and RII 83-05241.

[1] D. M. Lindsay, D. R. Herschbach, and A. L. Kwiram, Mol. Phys. 32, 1199 (1976).
[2] G. A. Thompson and D. M. Lindsay, J. Chem. Phys. 74, 959 (1981).
[3] J. A. Howard, K. F. Preston, and B. Mile, J. Am. Chem. Soc. 103, 6226 (1981).
[4] D. A. Garland and D. M. Lindsay, J. Chem. Phys. 78, 2813 (1983).
[5] The ESR spectra of Li_3 in adamantane are characteristic of a pseudorotating isomer. The magnetic parameters are surprisingly similar to those of Ref. 4. See J. A. Howard, R. Sutcliffe, and B. Mile, Chem. Phys. Lett. 132, 84 (1984).
[6] G. A. Thompson, Ph.D. thesis, City University of New York, 1985. Both ^{107}Ag and ^{109}Ag have negative nuclear moments. For simplicity, however, we consistently denote hf constants *and* related parameters as being positive if these correspond to positive spin populations.
[7] P. H. Kasai and D. McLeod, Jr., J. Chem. Phys. 55, 1566 (1971).
[8] F. J. Adrian, E. L. Cochran, and V. A. Bowers, Adv. Chem. 36, 50 (1962).
[9] D. A. Garland and D. M. Lindsay, J. Chem. Phys. 80, 4701 (1984).
[10] D. M. Lindsay and G. A. Thompson, J. Chem. Phys. 77, 1114 (1982).
[11] For a comprehensive review of ESR powder line shapes see P. C. Taylor, J. F. Baugher, and H. M. Kriz, Chem. Rev. 75, 203 (1975).
[12] This program was written by Dr. P. H. Kasai and modified to run on either an IBM CS9000 or a VAX 11/780 computer.
[13] P. H. Kasai, J. Am. Chem. Soc. 94, 5950 (1972).
[14] W. Weltner, Jr., *Magnetic Atoms and Molecules* (Van Nostrand, New York, 1983).
[15] All hf constants are expressed in Gauss using the conversion factor $g_e\beta_e$ ergs G^{-1} (β_e = electron Bohr magneton). Some authors use $g_e\beta_e$. See Ref. 15.
[16] For ^{109}Ag, the maximum inequivalency is estimated to be 3–4 G, a relatively small value compared to the ESR linewidth of 5–6 G. In addition this effect is probably largest for those orientations where there is little ESR intensity. For a discussion of the conditions under which two nuclei are completely equivalent see Ref. 11.
[17] P. Kusch and V. W. Hughes, *Handbuch der Physik*, edited by S. Flugge (Springer, Berlin, 1959).
[18] *Handbook of Physics and Chemistry*, edited by R. C. Weast (Chemical Rubber, Cleveland, 1975).
[19] The parallel features are less well resolved and in many instances overlapped by the much stronger perpendicular transitions. However, the (just) observed parallel features do occur at their predicted field positions.
[20] H. Kopfermann, *Nuclear Moments* (Academic, New York, 1958).
[21] A. Abragam and B. Bleaney, *Electron Paramagnetic Resonance of Transition Ions* (Oxford University, London, 1970).
[22] F. J. Adrian, J. Chem. Phys. 36, 1692 (1962); P. H. Kasai, W. Weltner, Jr., and E. B. Whipple, *ibid.* 42, 1120 (1965); G. H. Myers, W. C. Easley, and B. A. Zilles, *ibid.* 53, 1183 (1970).
[23] For the structural parameters of Ref. 37, the rotational constants for $^{107}Ag_3$ are $A = 0.050\ cm^{-1}$, $B = 0.033\ cm^{-1}$, and $C = 0.020\ cm^{-1}$ where A, B, and C correspond (in Fig. 2) to axes y, z, and x, respectively. For NO_2, $A = 8.0\ cm^{-1}$ with $B = 0.43\ cm^{-1}$ and $C = 0.41\ cm^{-1}$ (see Table D-4 of Ref. 15) so that a rotation about the a axis seems most likely (Ref. 23). In a matrix, the axis of rotation need not correspond exactly to a principal axis of inertia. See F. J. Adrian, J. Bohandy, and B. F. Kim, J. Chem. Phys. 81, 3805 (1984).
[24] Although both $A_z(1)$ and $A_z(1)$ have experimental uncertainties comparable to their difference, the two errors are correlated. Measurements made on several independently calibrated spectra all gave $A_z(1) > A_z(1)$.
[25] One further contribution to the dipolar tensor is the interaction of an isotropic spin population on one nucleus with the magnetic moments of adjacent nuclei. For $^{109}Ag_3$ the maximum interaction is estimated to be 0.03 G.
[26] Spin populations derived in this manner do not take into account matrix interactions or the effects of orbital contraction or expansion on molecule formation. As shown by the atom data of Table III, the former can contribute errors of several percent. For some radicals, orbital overlap effects introduce appreciable core orbital contributions to the hf constants. See J. B. Knight, Jr., A. Lagon, R. W. Woodward, D. Feller, and E. R. Davidson, J. Am. Chem. Soc. (in press).
[27] The anisotropic parameter $^{109}\beta_{5p}$ is proportional to the mean inverse cube radius $\langle r^{-3}\rangle_{5p}$ of a silver $5p$ orbital (Ref. 15). From the fine structure (J splitting) of the first excited state of atomic silver one finds $\langle r^{-3}\rangle_{5p} = 2.60$ a.u. Alternative values may be obtained by an appropriate scaling of $\langle r^{-3}\rangle_{5p}$ for ground state Ga. Using both J and hf splittings, the values obtained for silver are $\langle r^{-3}\rangle_{5p} = 2.98$ and 3.30 a.u., respectively. Accordingly, the average of these values (one standard deviation in parentheses) was adopted: $\langle r^{-3}\rangle_{5p} = 2.45(45)$ a.u., giving $^{109}\beta_{5p} = 9.0(12)$ G. A similar analysis has been made for the other Group IB elements and will be discussed in a separate article. See D. M. Lindsay and P. H. Kasai, J. Magn. Reson. (submitted).
[28] H. Basch, J. Am. Chem. Soc. 103, 4657 (1981).
[29] B. M. Gimarc, *Molecular Structure and Bonding* (Academic, New York, 1979).
[30] P. W. Atkins and M. C. R. Symons, *The Structure of Inorganic Radicals* (Elsevier, New York, 1967).
[31] H. C. Longuet-Higgins and A. J. Stone, Mol. Phys. 5, 417 (1962); A. J. Stone, Proc. Phys. Soc. London Sect. A 271, 424 (1963).
[32] C. E. Moore, *Atomic Energy Levels*, Natl. Stand. Ref. Data Ser. Natl. Bur. Stand. No. 35 (U. S. GPO, Washington, D. C., 1971).
[33] A deviation from axial symmetry comparable to the ESR linewidth (5–6 G) would be difficult to detect. This corresponds to an orthorhombic g tensor with two elements differing by no more than ~ 0.0030 or about $\frac{1}{2}$% of $\Delta g = -0.0465$.
[34] However $1b_1$ is mainly s in character and the contribution to Δg_{zz} from the $2b_1$ orbital of the p manifold may not be negligible. By contrast both $1a_2$ and $2b_1$ belong to the p manifold and it is probably the former that determines Δg_{xx}.
[35] R. Lefebvre, Mol. Phys. 12, 417 (1967).
[36] S. C. Richtsmeier, R. A. Eades, D. A. Dixon, and J. L. Gole, Am. Chem. Soc. Symp. Ser. 179, 177 (1982); S. C. Richtsmeier, D. A. Dixon, and J. L. Gole, J. Phys. Chem. 86, 3937 (1982).
[37] J. Flad, G. Igel-Mann, H. Preuss, and H. Stoll, Chem. Phys. 90, 257 (1984).
[38] W. Andreoni and J. L. Martins, Surf. Sci. (in press). The relative stabilities of the $^2A_1$ and $^2B_1$ states and the calculated spin populations were provided by Dr. J. L. Martins.
[39] C. P. Barrett, R. G. Graham, and R. Grinter, Chem. Phys. 86, 199 (1984).
[40] W. Schnittenlacher, W. Schroeder, H. H. Rotermund, and D. M. Kolb, Chem. Phys. Lett. 109, 7 (1984).
[41] For example the inversion splitting of the first excited vibrational state of NH_3 is over an order of magnitude smaller in N_2 than in either a rare gas matrix or in the gas phase. See C. Girardet, L. Abouaf-Marguin, B. Gauthier-Roy, and D. Maillard, Chem. Phys. 89, 431 (1984).
[42] S. M. Mattar and G. A. Ozin, J. Am. Chem. Soc. (in press). The calculated spin populations were provided by Dr. S. M. Mattar.

V. REFERENCES

1. J. Jortner, Phys. Chem. 88, 188 (1984).

2. J. J. Win, H.V. Nguyen, and R.C. Flanagan, Langmuir 3, 2, 266 (1987).

3. R. Uyeda and N. Wada, Japan. J. Appl. Phys., 4, 10, 707 (1965), 7,10 ,1287 (1968);
R. Uyeda and M. Kato, Japan. J. Appl. Phys., 15, 5, 757 (1976).

4. N. Wada, Japan. J. Appl. Phys., 8, 5, 551, (1969).

5. S. Iwana, E. Shichi and T. Sahashi, Japan. J. Appl. Phys., 12,10, 1531 (1973).

6. K. Kimoto, Y. Kamiya, M. Nonoiya and R. Uyeda, Japan J. App Appl. Phys., 2, 11, 702 (1963).

7. M. Moskovits and G. A. Ozin, editors, " Cryochemistry ", Wiley interscience, N.Y. 1976.

8. K. J. Klabunde, " Chemistry of Free Atoms and Particles ", Academic Press, N.Y. ,1980.

9. W. Weltner Jr. and R. J. Van Zee, Ann. Rev. Phys. Chem., 35, 291 (1974).

10. R. P. Messmer, " Cluster Model Theory ", in T. N Rhodin : The Nature of the Surface Chemical Bond, North Holland Amsterdam, 1979, p. 51.

11. L. R. Gillens, W. J. Morterer, R. Lissilow, and A. Le Beize, J. Phys. Chem. 86,13, 2509 (1986), L. R. Gillens, W.J. Morterer and J. B. Yetterhoeven, Zeolites, 7, 11 (1981), J. Michalik and L. Kevan, J. Am. Chem. Soc. 108, 15, 4247 (1986).

12. S. C. Davis and K. J. Klabunde, Chem. Rev., 82, 153 (1982).

13. L. Brewer and B. King, J. Chem. Phys., 53, 10, 3981 (1970).

14. J. A. Howard, R. Sutcliffe and B. Milles, J. Phys. Chem., 87, 13, 2268 (1983).

15. R. A. Zhitnikov, N. V. Kolesnikov and V. I. Kosyakov, Sov. Phys., JETP, 16, 4, 839 (1963); R. A. Zhitnikov and N. V. Kolesnikov, Sov.

Phys., JETP, 19,1, 65 (1964).

16. P. H. Kasai and P. M. Jones, J. Am. Chem. Soc., 106, 11, 3069 (1984), 107, 22, 6385 (1985).

17. D. M. Lindsay , D. R. Herschbach and A. L. Kwiram, Mol. Phys, 32, 1199 (1976), 39, 529 (1980), G. A. Thompson D. M. Lindsay, J. Chem. Phys., 74, 959 (1981), G. A. Thompson, F. Tischler, D. A. Garland, D. M. Lindsay, Surf. Sci., 106, 408 (1981), D. M. Lindsay and G. Thompson, J. Chem. Phys., 77, 3, 1114 (1982), D. M. Lindsay, Am. Soc. Symp. Ser., 179, Chap. 7 (1982), D. A. Garland and D. M. Lindsay, J. Chem. Phys, 78, 2813 (1983), 80, 4761 (1984).

18. P. J. Foster, R. E. Leckneby P. Willis, Adv. Phys, 16, 769 (1967).

19. P.W. Davies and G. Del Conde, Faraday Disscuss., 55, 369 (1973), Chem., Phys.,12, 45 (1967).

20. J. C. Whitehead and R. Grace, Faraday Disscuss., Chem. Soc. 55, 320 (1973).

21. A. Gelb, K. D. Jordan and R. Silbey, Chem. Phys. 9, 175 (1975).

22. R. C. Baetzold and R. E. Mack, Inorg. Chem. 14, 686 (1975).

23. B. T. Pickup and W. Byers.Brown, Mol. Phys., 23, 1189 (1972).

24. K. H. Benneman and J. Koutecky, ed. " Small Particles and Inorganic Clusters ", 3rd. Int. meeting, Berlin West, North Holland, Pub. Amsterdam, 1984.

25. Proc. 2nd. Int. meeting , Small Particles and Inorganic Clusters, Surf. Sci., 106, (1981).

26. Int. meeting, Small Particles and Inorganic Clusters, J. Phys., Paris, 38, 1977. c.2.

27. G. A. Ozin and S. Mitchell, Angew. Chem., Int. Ed. Engl., 22, 674 (1983).

28. C. & E. News, 20, 12.23.1985.

29. C. & E. News, 9, 3.2. 1987.

30. T. G Duety, M. A. Duncan, D. E. Powers, R. E. Smalley, J. Chem. Phys.,

74, 6511 (1981), J. Am. Chem. Soc., 107, 1729 (1985).

31. D. E. Powers, J. Phys. Chem., 86, 2566 (1982).

32. J. B. Hopkins, P. R. Langridge.Smith, M. D. Morse, R. E. Smalley, J. Chem. Phys., 78, 1627 (1983).

33. H. W. Krote, J. R. Heath, S. C. O'brien, R. F. Curl , R. E. Smalley, Nature, 318, 162 (1985).

34. S. C. Rithsmeir, M. C. Henderwerk, D. A. Dixon, J. L. Gole, J. Phys. Chem., 86, 20, 3932 (1982).

35. P. H. Kasai and D. Mc Leod jr., J. Phys. Chem., 79, 2334 (1975), 82, 13, 1554 (1978).

36. K. P. Flibsen and D. R. Huffman, Surf. Sci., 156, 793 (1985).

37. L. B. Knight Jr. and W. Weltner Jr., J. Chem. Phys., 54, 9, 3875 (1971), 56,3,1152 (1972), L. B. Knight Jr., W. C. Easley, W. Weltner Jr., M. Wilson, J. Chem. Phys., 54, 7, 332 (1971).

38. G. A. Ozin and H. Huber, Inorg. Chem., 17, 155 (1978).

39. W. E. Klotzbucher and G. A. Ozin, J. Am. Chem. Soc., 100, 2262 (1978), Inorg. Chem., 18, 2101 (1979).

40. G. A. Ozin and A. J. Harlan, Inorg. Chem. 18, 1781 (1979).

41. M. Moskovits and J. E. Hulse, J. Chem. Phys., 67, 4271 (1977).

42. T. G. Dietz, M. A. Duncan, D. E. Powers, R.E. Smalley, J. Chem. Phys., 74, 6511 (1981).

43. M. M. Kappes, R. W. Kuntz, and E. Schumacher, Chem. Phys. Lett., 91, 413 (1982).

44. H. Basch, J. Am. Chem. Soc., 103, 4657 (1981).

45. B. M. Gimarc, " Molecular Structure and Bonding ", Academic , New York, 1979.

46. S. C. Richtmeir, R. A. Eade, D. A. Dixon, J. L. Gole, Am. Chem. Soc. Symp. Ser. 179, 177 (1982).

47.G. A. Thompson, 1985, Ph. D. Thesis, CCNY.

48. P. H. Kasai and D. McLeod Jr., J. Chem. Phys., 55, 1566 (1971).

49. ESR Series User's Manual (1982), IBM Instrument Inc., Danbury Ct.

50. JES.ME.3X Electron Spin Resonance Instruments Instruction Manual, Japan Electron Optics Laboratory Co., Ltd., Tokyo, Japan.

51. C. P. Poole Jr. " Electron Spin Resonance ", 2nd. Ed., Wiley New York 1983.

52. D. M. Lindsay, 1974, Ph. D. Thesis, Harvard University.

53. A. N. Nesmeyanov, " Vapour Pressure of the Chemicals Elements ", Elsevier, New York 1963.

54. W. E. Forsythe, " Smithsonian Tables ", 9th. Rev. Ed., Smithsonian Institution, Washington 1956.

55. J. E. Wertz and J. R. Bolton, " Electron Spin Resonance ", McGraw.Hill, New York 1972.

56. A. Abragam and B. Bleaney, " Electron Paramagnetic Resonance of Transitions Metal Ions, Oxford , New York 1970.

57. A. Carrington and A.D. Mc Lachlan, " Introduction to Magnetic Resonance ", Harper and Row , New York 1967.

58. P. B. Ayscough, " Electron Spin Resonance Chemistry ", Metheun, London 1967.

59. N. M. Atherton, " Electron Spin Resonance ", Wiley, New York 1973.

60. W. Weltner Jr., " Magnetic Atoms and Molecules ", Scientific and Academic Editions, New York 1983.

61. C. P. Poole, Jr., and H. A. Farach, " The Theory of Magnetic Resonance ", Wiley.Interscisnce, New York 1972.

62. G. Breit and L. I. Rabi, Phys. Rev., 38, 2082 (1931).

63. P. H. Kasai and D. MCLeod, Jr., J. Chem. Phys., 55, 1566 (1971).

64. C. P. Slichter, " Principles of Magnetic Resonance ", Springer Verlag, Berlin 1980.

65. To be Published.

66. D. M. Lindsay, G. A. Thompson and Y. Wang, J. Phys. Chem., 91, 10 (1987).

67.G. A. Ozin, H. Huber and S. A. Mitchell, Inorg. Chem., 18, 10 (1979).

68. S. A. Mitchell, G. A. Kenney.Wallace, G. A. Ozin, J. Am. Chem. Soc., 103, 20 (1981).

69. G. A. Ozin, H. Huber, D. Mc Intosh, S. Mitchell, J. G. Norman, L. Noodlemam, J. Am. Chem. Soc. 101, 13, 3504 (1979).

70. M. Moskovits and J. E. Hulse, J. Chem. Soc. Faraday Trans. II., 73, 471 (1977).

71. F. J. Adrian, E. L. Cochran and V. A. Bowers, Adv. Chem., 36, 50 (1962).

72. Reprint of $^{107}Ag_3$ in Appendix I.

73. J. A. Howard, K. F. Preston and B. Mile, J. Am. Chem. Soc., 103, 6226 (1981).

74. H. Kopperman, " Nuclear Moments ", Academic Press, New York 1958.

75. C. P. Barret, R. C. Graham and R. Gruiter, Phys. 86, 199 (1984).

76. W. Schuhenlachler, W. Schroeder, H. H. Rotesmund, D. M. Kolb, Chem. Phys. Lett., 109, 7, 1 (1984).

77. J. Flad, G. Igel.Manm, H. Preuss, H. Stoll, Chem. Phys., 90, 257 (1984).

78. P Kusch and V. W. Hughes, " Handbuch der Physik ", edited by S. Flugge, Springer, Berlin 1959.

79. S. M. Mattar and G. A. Ozin, J. Am. Chem. Soc. (in Press).

80. W. Andreoni and J. L. Martins, Surf. Sci. (in Press).

81. D.M. Lindsay and P.H. Kasai., J. Mag. Reson., 64, 100 (1983).

82. F.J. Adrian, J. Bohandy and B.F. Kim., J.Chem. Phys., 81, 3805 (1984)

83. P.W. Atkins and M. C. Symmons, " The Structure of Inorganic Radicals ", Elsevier, New York 1967, D. M. Gruen, in " Cryochemistry ", eds. M. Moskovits and G. A. Ozin, Wiley, New York 1976, p. 441, D. M. Gruen and J. K. Bates, Inorg. Chem.., 16, 10, 2450 (1977).

84. H. Abe, W. Schulze and D. M. Kolb., Chem. Phys. Lett., 60,2,208 (1979).

85. L.B. Knight and M. A. Ebner, J. Mol. Spec., 61, 412 (1976).

86. Hamada, Nature, 127, 55 (1931).

87. J.R. Sonheim, P. Sthapitandra and J.L. Margrave, J. Phys. Chem., 59, 132 (1955).

88. Hamada, Philos. Mag. G. B., 12, 5067 (1931).

89. A. S. King, Publ. Astron. Soc. Pacific., 52, 325 (1940); 54, 6 (1942).

90. S. Barat, Proc. Roy. Soc. A 109, 194 (1925).

91. D. J. Benard and S.W. Slafer, Chem. Phys. Lett., 56, 3, 438 (1978).

92. D. J. Benard and S.W. Slafer, Chem. Phys. Lett., 48, 321 (1977).

93. M. M. Kappes, P. Radi, M. Schar, E. Schumacher., Chem. Phys. Lett., 113, 3, 243 (1985).

94. A. C. Chan and E. R. Davidson, J. Chem. Phys., 52, 8, 4108 (1969).

95. C. Shing-Piaw, W. Loong-Seng and L. Yoke-Seng, Nature, 209, 1300 (1966).

96. R. A. Chiles, C. E. Dysktra, and K. D. Jordan., J. Chem. Phys., 75, 2, 1044 (1981).

97. C. W. Bauschlicher, jr., P.S. Bagus, and B. N. Cox., J. Chem. Phys., 77, 8, 4032 (1982).

98. P. Y. Cheng, and M. A. Duncan., Chem. Phys. Lett., 152, 341 (1988).

99. P.S. Bechthold, U. Kettler, H. R. Schobeer, and W. Krasser., Z. Phys. D-Atoms, Molecules and Clusters., 3, 263-270 (1986).